

**CHARACTERIZATION OF CARRIER DECAY MECHANISMS
AND QUANTUM YIELD IN COLLOIDAL UPCONVERTING
NANOSTRUCTURES**

by

Kyle R. Lennon

A thesis submitted to the Faculty of the University of Delaware in partial fulfillment of the requirements for the degree of Honors Bachelor of Chemical Engineering with Distinction

Spring 2018

© 2018 Kyle R. Lennon
All Rights Reserved

CHARACTERIZATION OF CARRIER DECAY MECHANISMS
AND QUANTUM YIELD IN COLLOIDAL UPCONVERTING
NANOSTRUCTURES

by

Kyle R. Lennon

I certify that I have read this thesis and that in my opinion it meets the academic and professional standard required by the University as a thesis for the degree of Bachelor of Chemical Engineering.

Signed: _____

Matthew Doty, Ph.D.
Professor in charge of thesis

Approved: _____

Joshua Zide, Ph.D.
Committee member from the Department of Materials Science and
Engineering

Approved: _____

Matthew DeCamp, Ph.D.
Committee member from the Board of Senior Thesis Readers

Approved: _____

Paul Laux, Ph.D.
Director, University Honors Program

ACKNOWLEDGMENTS

I would like to extend my sincerest thanks to Dr. Doty for his tremendous help and guidance since I joined his group nearly two years ago. His support has given me confidence in my abilities as a researcher, and has made possible so many great opportunities within my undergraduate career and beyond. I would also like to thank Eric Chen, who taught me all of the skills needed to complete this project, and whose companionship made my time in the lab enjoyable as well as productive. I would like to thank the Doty Group, for welcoming me without hesitation. I would also like to thank Dr. Zide and Dr. DeCamp for all of their help in advising my thesis. Finally, I would like to thank my parents, my sisters, my family, and my friends, without whom I could not have made it though the last four years.

For funding, I would like to acknowledge the contribution of the W.M. Keck Foundation to the research endeavors of the Doty Group, as well as the Undergraduate Research Program at the University of Delaware for its support as a Summer Scholar and for the ability to present my work at the 2017 AIChE National Conference with the support of a Travel Award.

TABLE OF CONTENTS

LIST OF TABLES	vii
LIST OF FIGURES	viii
ABSTRACT	xii
 CHAPTERS	
1 INTRODUCTION	1
2 BACKGROUND	7
2.1 Origin of and Methods for Overcoming the Shockley-Queisser Limit	7
2.1.1 Singlet Fission	9
2.1.2 Luminescent Downconversion and Luminescent Downshifting	9
2.1.3 Intermediate-Band Solar Cells	10
2.1.4 Photon Upconversion	10
2.1.5 Multi-Junction Solar Cells	11
2.1.6 Solar Concentrators	11
2.2 Photon Upconversion	12
2.2.1 Fundamentals	12
2.2.2 Performance Metrics	15
2.2.3 Summary of Existing Materials	17
2.2.3.1 Lanthanide and Transition-Metal-Ion Upconverters	17
2.2.3.2 Sensitized Triplet-Triplet Annihilation	19

2.2.3.3	Quantum Structures	21
2.2.4	Heterostructure Engineering of Core-Rod Colloidal Semiconductors	24
2.3	Synthesis	26
2.3.1	Materials	27
2.3.2	Synthesis of CdSe(Te) Cores	27
2.3.3	Growth of CdS Rods	27
2.3.4	Growth of CdSe Quantum Dot	28
2.4	Computational Modeling	28
3	CHARACTERIZATION METHODS	33
3.1	Steady-State Photoluminescence	34
3.1.1	Motivation and Background	34
3.1.1.1	Diffraction Grating	36
3.1.1.2	CCD Silicon Spectrometer	36
3.1.2	Methods	37
3.1.3	Results	39
3.1.4	Analysis	42
3.2	Excitation Power Dependence	45
3.2.1	Motivation and Background	45
3.2.1.1	Power-Law Relations	46
3.2.1.2	Saturation	47
3.2.2	Methods	48
3.2.3	Results	49

3.2.4	Analysis	49
3.3	Time-Resolved Photoluminescence	52
3.3.1	Motivation and Background	53
3.3.1.1	Time-Correlated Single Photon Counting	54
3.3.2	Methods	56
3.3.3	Results	57
3.3.4	Analysis	60
3.4	Quantum Yield	61
3.4.1	Motivation and Background	62
3.4.1.1	Integrating Sphere	63
3.4.1.2	Quantum Yield Standard: Rhodamine 101	64
3.4.1.3	Calculating Quantum Yield	65
3.4.2	Methods	67
3.4.3	Results	69
3.4.4	Analysis	71
3.5	Summary	78
4	FUTURE WORK	81
4.1	Compositional Grading	82
4.2	Peak Deconvolution	83
	BIBLIOGRAPHY	87
	APPENDIX	
A	MATLAB PROGRAM FOR CALCULATING QY AND UCQY	90
A.1	Main Window	91
A.2	Secondary Window	93
A.3	Results Window	94

LIST OF TABLES

1	Descriptions and expressions of rates used in the kinetic model for the InAs-based system depicted in Figure 8(a) . Adapted from [5]. . . .	31
2	Key features of the PL spectrum for each upconverting sample. . .	41
3	Exponential decay lifetimes obtain from TRPL fits.	60
4	Summary of QY and UCQY measurements for the emitter peak in each structure.	71
5	Summary of QY and UCQY measurements for the emitter peak in each structure, with UCQY values obtained via deconvolution of the emitter and absorber peaks.	76

LIST OF FIGURES

1	The physical structure of a CdSe(Te)/CdS/CdSe nanorod upconverter (top) and the band structure for the upconverter (bottom). Red and orange arrows indicate the absorption of low-energy light, and green arrows indicate the emission of high-energy light.	5
2	(a) Design of an upconverter-backed solar cell. High-energy photons (green) are absorbed in the cell, while low energy photons (orange and red) pass through the cell to the upconverting layer, where they are converted to high-energy light to be absorbed in the cell. (b) Depiction of perfect upconversion. (c) Depiction of upconversion with intentional energy loss introduced to suppress radiative (orange) and nonradiative (red) loss pathways. (d) Depiction of Photon Energy Sacrifice (PES) in the upconversion process [3].	13
3	Energy levels and wavelengths of transitions of trivalent erbium. Successive excitation leading to upconversion is indicated by the curved arrows [17].	18
4	Schematic of the upconversion process within a TTA system. Solid lines represent radiative transitions, while dashed lines represent nonradiative transitions. 'S' denotes a singlet state, 'T' denotes a triplet state, and 'TTA' represents either a homo (I) or hetero (II) TTA pathway [2].	20
5	Band diagram of an epitaxial upconverting quantum structure. The upconversion process consists of exciton generation (1), hole migration (2), secondary electron excitation (3), electron migration (4), and recombination (5). [3].	23
6	Schematic of an upconverter-backed solar cell under solar radiation (left). Depiction of the physical dimensions and structure of a CdSe(Te)/CdS/CdSe core-rod upconverter (boxed in red). Diagram of the upconverter band structure (boxed in blue), showing interband absorption (orange arrow), intraband absorption (red arrows), carrier migration (black arrows), and emission (green arrow).	25

7	The major reactants and reaction steps for the synthesis of CdSe(Te)/CdS/CdSe upconverting nanorods. Transmission electron microscope (TEM) images of (a) the CdSe(Te) cores, (b) the CdSe(Te)/CdS core/rods, and (c) the CdSe(Te)/CdS/CdSe core/rod/dot structures [27].	29
8	(a) Kinetic model of upconversion in InAs-based epitaxial quantum structures. Solid arrows show the direction of the upconversion process, dashed arrows show the direction opposite from preferred [5]. (b) The framework of a kinetic model for CdSe(Te)/CdS/CdSe colloidal core-rod quantum structures, showing the high degree of similarity with the model in (a).	30
9	(a) Upconversion quantum yield of the epitaxial quantum structure as a function of PES for a GaAs host cell [5]. (b) Overall solar cell efficiency for a variable host cell band gaps backed by epitaxial upconverting structures of variable PES. The dashed line indicates a GaAs host cell [3].	32
10	The experimental setup for free-space photoluminescence measurements. The excitation beam (either red, purple, or green here) is directed through a microscope objective to the sample, and PL/UCPL (UCPL shown in orange) is collected through an objective and directed to the spectrometer and CCD for measurement by a computer.	38
11	Normalized steady-state PL spectra obtained via excitation with a 405nm CW laser at 1 W/cm ² for (a) 4% Te-doping, (b) 10% Te-doping, (c) 20% Te-doping, and (d) 40% Te-doping.	40
12	Normalized steady-state UCPL spectra (red) obtained via excitation with a 735nm CW laser at 10W/cm ² overlaid with corresponding PL spectra (dashed) for (a) 4% Te-doping, (b) 10% Te-doping, (c) 20% Te-doping, and (d) 40% Te-doping. A 650nm SP filter was used for all measurements.	42
13	Several UCPL spectra for (a) the 4% Te-doped sample, (b) the 10% Te-doped sample, (c), the 20% Te-doped sample, and (d) the 40% Te-doped sample, taken at varying 745nm CW laser powers. The incident laser power is indicated by the curves color in coordination with the x-axis of the inset. The inset shows the log-log plot of integrated peak counts vs. incident power, showing the log-log slope.	50

14	The extended log-log power dependence relation for the 4% (black), 10% (red), 20% (blue), and 40% (pink) Te-doped samples, showing saturation effects in the neighborhood of 100-200 mW excitation power.	51
15	Operating principle for TCSPC. The laser pulse signals the timing mechanism to begin, and the arrival of a photon at the detector signals timing to stop. Because the arrival times of photons is random, forming a histogram from multiple measurements will give the decay profile for a radiative transition [31].	55
16	The experimental setup for TRPL measurements. The path of the exciting laser is shown in blue, the path of PL is shown in green, and electrical wiring is shown by curved black lines. The computer demonstrates the form of a TRPL decay curve.	57
17	The 2D TRPL profile for the 4% Te-doped sample. The inset shows two TRPL measurements at constant wavelength correlating to the emitter (596nm) and absorber (770nm) peaks, with the primary extracted lifetime for each state noted.	58
18	The 2D TRPL profile for the 10% Te-doped sample. The inset shows two TRPL measurements at constant wavelength correlating to the emitter (590nm) and absorber (660nm) peaks, with the primary extracted lifetime for each state noted.	58
19	The 2D TRPL profile for the 20% Te-doped sample. The inset shows two TRPL measurements at constant wavelength correlating to the emitter (575nm) and absorber (760nm) peaks, with the primary extracted lifetime for each state noted.	59
20	The 2D TRPL profile for the 40% Te-doped sample. The inset shows two TRPL measurements at constant wavelength correlating to the emitter (575nm) and absorber (725nm) peaks, with the primary extracted lifetime for each state noted.	59
21	(a) The chemical structure of Rhodamine 101. (b) The PL spectrum of Rhodamine 101 excited with 532nm laser, showing the peak integration equating to 100% quantum yield.	65
22	The experimental setup for measuring QY and UCQY. The multiple excitation sources are shown in green, red, and purple, and the fiber bundles are shown by curves black lines.	69

23	UCPL spectra for (a) the 4% Te-doped sample, (b) the 10% Te-doped sample, (c) the 20% Te-doped sample, and (d) the 40% Te-doped sample. The areas shaded in red show the integrated area used to determine the noted UCQY values.	70
24	UCPL spectra taken in the integrating sphere with the corresponding two-Gaussian fits for (a) the 4% Te-doped sample, (b) the 10% Te-doped sample, (c) the 20% Te-doped sample, and (d) the 40% Te-doped sample. Raw data is shown in red, and fits are shown with blue dashes, with R^2 values shown.	74
25	Deconvolved UCPL spectra for (a) the 4% Te-doped sample, (b) the 10% Te-doped sample, (c) the 20% Te-doped sample, and (d) the 40% Te-doped sample, using the fits shown in Figure 24 . The UCPL is determined by integrating the emitter peak Gaussian fit (the red shaded region).	75
26	Values of the UCQY (black), QY (red) and UCQY/QY ratio (blue) for each sample, all reported in percents.	77
27	Four variations of the CdSe(Te)/CdS/CdSe upconverting nanostructure available by changes in the compositional grading of the absorber quantum dot and the CdS rod. The current version consists of a graded absorber, flat rod (top), and the proposed optimized version consists of a flat absorber and graded rod (bottom).	83
28	Three methods for deconvolving the emitter and absorber peaks. The top figures show the UCPL spectra with the complete fit, and the bottom figures show the deconvolved emitter peak with its Gaussian fit for (a) the fitting method involving a Gaussian fit plus a scaled version of the absorber-rod fit, (b) a two-Gaussian fit of the full UCPL data only, and (c) the fitting method involving a Gaussian fit plus a scaled version of the raw absorber-rod data.	86
A.1	The main window of the Quantum Yield MATLAB program.	92
A.2	The first secondary window of the Quantum Yield MATLAB program.	95
A.3	The results window of the Quantum Yield MATLAB program.	96

ABSTRACT

With the continued rise to prominence of solar energy, increasing effort is being focused on developing more efficient solar energy harvesting technologies. Of those technologies, photon upconversion materials have been demonstrated by simulation to offer large potential efficiency boosts. While the systems that can perform photon upconversion are varied, this study focuses on CdSe(Te)/CdS/CdSe nanorod upconverting heterostructures. In this study, key aspects of the upconversion mechanism within these structures are examined, and the results are compared between samples with different levels of Tellurium doping within the absorber quantum dot to determine the efficacy of Te-doping as a design parameter for heterostructure optimization. For each structure, photoluminescence and upconversion PL measurements are taken to identify the presence of upconverted light. The dependence of the intensity of upconversion on the incident photon flux is then measured to assess the nature of the upconversion phenomenon. Time-resolved PL measurements are taken to obtain the decay lifetimes associated with carriers that can radiatively recombine. Finally, the efficiency of each structure is probed through upconversion quantum yield (UCQY) measurements in a precisely calibrated integrating sphere. While successful upconversion is observed in each structure, power-dependent measurements indicate that the upconversion does not obey the desired purely two-photon mechanism. Moreover, the structures upconvert with low efficiency, producing UCQY values less than 0.001%. However, trends between the structures indicate that adjusting the Te-doping has not had its desired effect, but has instead caused unintended changes in the structures, such as a pronounced inhomogeneity within the absorber quantum dot. To isolate the effect of Te-doping and to further optimize the structures, the effect of this inhomogeneity must be thoroughly examined in future studies.

Chapter 1

INTRODUCTION

Since the beginning of the effort to reduce humanity's dependence on non-renewable energy sources, solar energy conversion has been of principle interest. The amount of energy striking the earth in the form of sunlight is by far abundant enough to sustain the world's energy consumption, and the steady advancement of solar technologies allow for a substantial portion of that light to be transformed into electricity. These technologies, however, still face a critical economic barrier to widespread implementation in many areas: the price per kilowatt-hour of solar energy is still greater than the price of energy from the current electrical grid. Until solar energy is able to reach parity with the electrical grid price from fossil fuel burning, economic incentives will prevent the widespread adaptation of solar energy as the primary energy source. To close this once large price gap, researchers worldwide have focused on making solar cells more efficient. As the gap has closed, however, new challenges for solar energy have arisen, such as the difficulty in cheap storage of solar energy for use during periods of low or no sunlight, and in scaling production to meet increased demand.

While the efforts to increase the efficiency of traditional silicon solar cells have succeeded in decreasing the cost of solar energy greatly, they may soon reach their physical limit. This limit on the efficiency of silicon solar cells, and extendable to solar cells made of other materials, is called the Shockley-Queisser Limit. By performing a detailed energy balance on a solar cell, Shockley and Queisser determined that conventional solar cells could only reach an energy conversion efficiency slightly above 30%. This limit is due in a large part to energy lost via unabsorbed low-energy photons, whose energy is lower than the solar cell's band gap, and via thermalization of high

energy carriers, which must relax to the band edge of the solar cell, generated by high energy photons.

As current solar technologies approach this limiting value, it becomes increasingly difficult to innovate without looking towards new technologies which are not bounded by this limit. Many of these new technologies, such as multi-junction and intermediate-band solar cells, require a complete redesign of the solar cell itself to increase the limit on efficiency. While these cells can theoretically operate above the Shockley-Queisser limit, which limits only single-junction cells, their economic viability is limited by large manufacturing costs. Because the manufacturing of silicon-based cells is already well-established and highly optimized, new technologies that enhance single-junction silicon cells, rather than replace them, have large economic advantages. Of these technologies, the two most widely studied are photon upconversion and photon downconversion. The former focuses on capturing the low-energy light that silicon cells cannot absorb, and the latter aims to minimize thermalization losses associated with high-energy light. In either case, the technology can be used to develop a separate layer which is electrically isolated from solar cell, and can be added either in front of or behind the cell to enhance energy conversion.

While thermalization losses are substantial in silicon solar cells, the disuse of low-energy light accounts for a greater portion of their inherent losses. Therefore, photon upconversion promises greater potential benefits than does downconversion. At its most basic level, photon upconversion is a process by which two low-energy photons are absorbed by some system and used to generate a high-energy emitted photon. Therefore, photons with energy below the band gap of a solar cell can be absorbed by an upconverting structure (also called an 'upconverter'), and a photon with energy above the solar cell band gap can be emitted by the upconverter and absorbed by the cell to generate current.

For an upconverter to have the largest impact in this manner, therefore, it should excel in a few critical performance metrics. The first is that it must have the capability to absorb a large amount of the low-energy portion of the solar spectrum;

in other words, it should have a large absorption bandwidth (AB). Because the maximum efficiency impact that an upconverter can have is limited by the amount of the unused solar light it can capture, it is obvious why a larger AB is desired. The second metric for upconverter performance quantifies the inherent energy loss associated with the upconversion process. Thermodynamically, it is expected that some of the energy of the absorbed photons must be lost, or sacrificed, to drive the upconversion process forward. However, the loss of too much energy might negate the upconversion process altogether, as well as limit the wavelengths of low-energy light which can be successfully upconverted. This inherent energy loss is called the photon energy sacrifice (PES) of the upconverter. The final performance metric for upconverters is called the upconversion quantum yield (UCQY), and is akin to the efficiency of a solar cell. This metric measures the efficiency of the upconversion process, in terms of the number of upconverted photons per absorbed photons. A perfectly efficient upconverter will emit one high-energy photon per two low-energy photons absorbed. However, internal losses and the reversibility of many steps in the upconversion process diminish this efficiency. To maximize the impact of an upconverter, the UCQY itself must be maximized.

A few technologies exist which have demonstrated successful upconversion. Rare-earth doped nanocrystals, most often doped with lanthanide elements, have demonstrated fairly high UCQY values, above 20% [1]. Sensitized triplet-triplet annihilation (TTA) particles also show high UCQY, above 30% for this class of materials [2]. However, both of these classes of upconverters are limited by relatively large PES (some up to 1.3 eV, larger than the band gap of silicon solar cells [3]), and are severely limited AB values of less than 0.1 eV [1, 4]. A third class of upconverters, consisting of quantum compound semiconductor structures, offers potential remedies to these issues. Rather than only allowing transitions between distinct atomic or molecular states, these quantum structures allow transitions between bands. Therefore, the AB of quantum structures is in general much higher than that for lanthanide and TTA upconverters. Additionally, varying the composition of the compound semiconductors allows the band structure of these particles to be finely adjusted to control the PES

and to maximize upconversion efficiency. While high UCQY has not yet been observed in quantum structures, kinetic models predict that they might obtain UCQY values substantially above 50% at moderate PES values [5]. Their promise and ability to be customized warrants extensive research into quantum structure upconverters.

Many different materials and structures can comprise a quantum structure upconverter. In this paper, CdSe(Te)/CdS/CdSe nanorod upconverters will be examined. These structures consist of a CdS 'nanorod' grown around a CdSe(Te) 'absorber' quantum dot, which resides at one end of the rod. This absorber dot can have varied composition of Tellurium, the greater of which should decrease the band gap of the absorber dot. Both the CdS rod and the absorber dot can be synthesized to either have a 'flat' band edge (i.e. compositional uniformity across the region) or a graded band edge (i.e. compositionally graded). Though predictions using the kinetic model and first principles assume that the rod is graded and the absorber is flat, the basic synthetic methods employed in this study were found to produce flat-rod, graded-absorber structures. At the other end of the rod, a CdSe 'emitter' quantum dot is grown. The structure of this upconverter is shown in [Figure 1](#). In the absorber dot of these structures, two photon are absorbed to generate a doubly-excited electron-hole pair. The first absorption event involves the interband excitation of an electron-hole pair, and the second event involved the intraband excitation of the hole. The electron and hole migrate across the rod to the emitter dot, where radiative recombination results in the emission of a high-energy photon.

As mentioned above, one possible design parameter for this upconverter is the Tellurium doping (Te-doping) ratio in the absorber quantum dot. With increased Te-doping, the band gap of the absorber should decrease. Therefore, it is expected that this increased Te-doping might increase the AB of the structure, a salient feature for photovoltaic applications. However, it is unknown what other effects this change in Te-doping might cause. To determine the effect of Te-doping on a variety of aspects of the upconverter, four batches of upconverter were synthesized with four different Te-doping

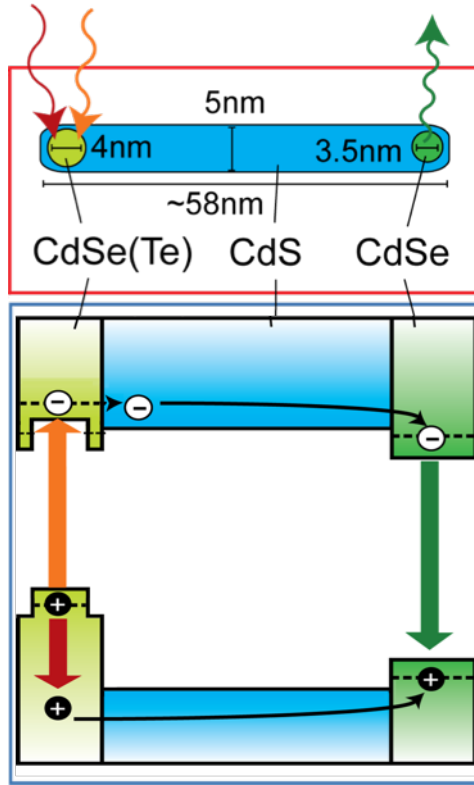


Figure 1: The physical structure of a CdSe(Te)/CdS/CdSe nanorod upconverter (top) and the band structure for the upconverter (bottom). Red and orange arrows indicate the absorption of low-energy light, and green arrows indicate the emission of high-energy light.

percentages: 4%, 10%, 20%, and 40%. The focus of this study is to carefully characterize each of these upconverting samples by a variety of methods to determine the effect of Te-doping on important photophysical and performance properties of the upconverter. These methods include steady-state photoluminescence (PL) spectroscopy, which will measure the emission spectrum of each sample, both for above and below band gap excitation. Comparison of spectra with above and below band gap excitation will determine if upconversion is occurring with emission in the emitter dot. Next, by varying the excitation power density for below band gap excitation, power-dependent upconversion measurements will be obtained. By determining the power-law relation between the upconversion intensity and the excitation power density, this method will elucidate important photophysical information about the upconversion process within

the structures, such as the order (e.g. one-photon absorption, two-photon absorption, or some mixture) of the upconversion process. By changing the excitation source from continuous-wave to pulsed, time-resolved photoluminescence (TRPL) measurements will be taken to measure the kinetics of the radiative recombination processes within the upconverters. This information, along with providing valuable insight to the nature of carrier decay in the structures, can be fed into the computational kinetic model to provide more accurate predictions of the upconverter efficiency. Finally, steady-state upconversion PL measurements will be taken inside of an integrating sphere. This sphere allows precise calibration between measurements, and therefore will be used to determine the UCQY of each structure.

Once results for all characterization methods are obtained, they can be compared between samples to determine the effect of Te-doping, and whether adjusting the doping level alone is a viable method for engineering more efficient upconverters. After a thorough exploration of the background information discussed throughout this chapter in [Chapter 2](#), the details and results of these characterization methods are presented in [Chapter 3](#).

Chapter 2

BACKGROUND

2.1 Origin of and Methods for Overcoming the Shockley-Queisser Limit

While technological improvements have advanced the efficiency of silicon solar cells for decades, modern solar cells still fail to convert the majority of energy from incident solar radiation into usable electrical current. While deficiencies in the design of solar cells are responsible for some of this loss, the majority of this inefficiency arises from fundamental limits on the performance of silicon solar cells. In 1961, William Shockley and Hans J. Queisser carried out a detailed balance on p-n junction solar cells to obtain the *detailed balance limit* of the efficiency of these solar cells, a limit which is now commonly referred to as the *Shockley-Queisser Limit* [6].

Shockley and Queisser's original balance limit is based on the assumption that radiation from a perfect blackbody sun at a temperature of 6000 K is incident over a small solid angle on a solar cell which is itself a blackbody at 300 K. Their analysis is predicated on three simple yet critical assumptions. For a solar cell of band gap E_g :

- All photons with energy greater than or equal to E_g create an electron-hole pair,
- All photons with energy greater than E_g have the same effect as a photon with energy E_g ,
- No photon with energy less than E_g produces an effect.

The detailed balance model includes five component processes:

1. generation of electron hole-pairs by absorption of solar photons,
2. radiative recombination of electron-hole pairs,
3. nonradiative processes which generate electron-hole pairs,

4. nonradiative recombination of electron-hole pairs,
5. removal of electron and holes in the form of electrical current

A slight modification of the original calculations has been performed, relaxing the assumption that incident light is from a perfect blackbody sun by computing the limit given the true solar spectrum [7]. The spectrum used in this calculation is the AM 1.5G spectrum, composed of direct sunlight combined with scattered contribution from the atmosphere, integrated over a hemisphere. Based on this analysis, the Shockley-Queisser Limit for the efficiency of a silicon solar cell, with a band gap of 1.1 eV, is just over 32%. Because only a third of the incident solar energy can possibly be converted to usable energy forms by traditional silicon solar cells, it is evident that the fundamental limitations of silicon solar cell severely inhibit the efficiency of solar energy conversion.

To understand how next-generation solar cells can overcome the limitations of these traditional, single-junction silicon solar cells, it is instructive to take a simpler approach to the detailed Shockley-Queisser balance. If only processes (1) and (5) from above occur within the solar cell, corresponding to the limiting case in which the solar cell is at absolute zero temperature, and the blackbody sun completely surrounds the solar cell, the only limitations of the solar cell are given by the latter two of the original three assumptions listed above. Specifically, any deviation from 100% efficiency is due either to the loss of energy from treating every photon with energy greater than E_g as a photon with energy equal to E_g , or is due to the disuse of photons with energy less than E_g . Shockley and Queisser themselves performed this calculation using the Planck distribution to determine the solar photon flux, and determined that in this highly idealized case, the maximum efficiency at 1.1 eV is only 44% [6]. Clearly, the majority of the inherent loss in silicon solar cells is due to these two simple limitations - the relaxation of high-energy electrons and holes generated by high-energy photons to the energy E_g , and the disuse of low-energy photons. As a result, these have been

two widely explored areas in the effort to overcome the Shockley-Queisser Limit. These efforts are explored in further detail below.

2.1.1 Singlet Fission

One proposed method for remedying the loss from high-energy photons is called *singlet fission*. In traditional cells, high-energy photons would create a single electron-hole pair, called an *exciton*, with energy well above the band edge of the cell. However, this exciton relaxes to the band edge, losing the excess energy to heat via phonon emission. In singlet fission, the same high-energy photon creates an exciton in the singlet state, which spontaneously splits into two triplet excitons with half of the energy of the singlet. Singlet fission cells could therefore potentially double the current from high-energy photons. Organic singlet fission cells have been demonstrated to produce external quantum yields in excess of 100% for high-energy light, meaning that, on average, a single incident high-energy photon produces more than one exciton, and integration into silicon solar cells could produce an overall efficiency exceeding 30% [8].

2.1.2 Luminescent Downconversion and Luminescent Downshifting

Another method for more efficiently capturing the energy of high-energy solar photons is *luminescent downconversion*. Similar to singlet-fission, the ultimate aim of downconversion is to create multiple excitons per high-energy photon. In downconversion, an external material, electrically isolated from the host solar cell, captures high-energy light to create an exciton. Due to an intermediate state within the downconverting material, this single exciton undergoes two radiative transitions, and emits two photons closer in energy to the host cell's band gap. These photons can then be absorbed within the host cell and converted to current. Models of a downconverting-enhanced solar cell under unconcentrated solar radiation have demonstrated an increase in the detailed balance limit of efficiency to 39.63% [9].

Similar to luminescent downconversion, *luminescent downshifting* (LDS) externally converts high-energy photons to low-energy photons. However, in LDS, only a

single low-energy photon is generated per high-energy photon. Because silicon solar cells more efficiently harvest light with energy closer to its band gap, this results in modest efficiency increases. Overall efficiency improvements of up to 3% have been reported for LDS-enhanced silicon solar cells [10]. Due to their electrical isolation from host solar cells, luminescent downconversion and downshifting share the advantage of being easily adaptable to the current generation of silicon solar cells.

2.1.3 Intermediate-Band Solar Cells

While the above methods seek to recapture lost energy from the high-energy portion of the solar spectrum, multiple methods exist with hopes of capturing the low-energy light unused by conventional silicon cells. *Intermediate-band (IB) solar cells* are one such method. In these cells, impurities introduce a new state, called the *intermediate band*, within the band gap of the solar cell. Photons with energy too small to excite across the entire band gap can now excite electrons from the valence band to the intermediate band, and from the intermediate band to the conduction band, where the exciton can now produce a current. Under concentrated solar radiation, for a single intermediate band, a detailed balance calculation gives a new overall efficiency limit of 63.1% [11]; and for an infinite number of intermediate bands, the efficiency limit is 77.2% [12]. The concept of *solar concentration* is explored shortly in 2.1.6.

2.1.4 Photon Upconversion

Similar to IB solar cells, *photon upconversion* aims to capture the low-energy photons in the solar energy harvesting process. Upconversion, as its name might indicate, is essentially the reverse of downconversion; two low-energy photons are combined within the upconverting material to form a single high-energy photon. Upconverting materials are electrically isolated from the host solar cells, and can therefore be easily adapted to silicon solar cells. The details of photon upconversion are explored in 2.2.

2.1.5 Multi-Junction Solar Cells

While the above section detail methods for separately considering the energy loss from photons with high and low energies, the focus of *multi-junction solar cells* is to simultaneously remedy both issues. In a multi-junction solar cell, different semiconductor materials, each with a band gap tuned to a different portion of the solar spectrum, are layered to form the multi-junction cell. By virtue of this layering, high-energy light can be captured in the material with the highest band gap, allowing for more efficient energy capture, while materials with lower band gaps allow for the capture of lower-energy light. While the high fabrication costs of these cells inhibits their commercial viability, multi-junction cells are highly efficient. Based on detailed balance limits, under unconcentrated solar radiation, a multi-junction cell with three layers demonstrates a limiting efficiency of 49%, and an infinite-layer cell is limited at 68%. Under maximally-concentrated solar radiation, these same configurations demonstrate limiting efficiencies of 63% and 86%, respectively [13].

2.1.6 Solar Concentrators

In Shockley and Queisser’s original balance limit, the intensity of solar radiation was set at the value of unconcentrated sunlight on the earth’s surface. However, increasing this intensity has been shown to improve the efficiency of solar cells; therefore, *solar concentration* has become a significant field of research for surpassing the Shockley-Queisser limit. Solar concentrators come in many forms, including systems of mirrors and lenses, microlenses, and nanowires. As was demonstrated in the above sections, the use of concentrated sunlight can significantly increase the efficiency limit of solar cells of many forms. Even for a traditional single-junction silicon solar cell, solar concentration has already been demonstrated an increase in the efficiency limit of solar cells. Single-nanowire concentrators on a silicon solar cell have already demonstrated an apparent efficiency of 40% [14]. Because of their applicability to a variety of platforms, solar concentrators continue to be widely studied in parallel with the above methods.

2.2 Photon Upconversion

While theoretical considerations of the above methods have demonstrated promise, practical considerations reveal their limitations. For multi-junction cells, the high materials and fabrication cost limit commercial applications, while for IB solar cells, loss pathways introduced by the intermediate band inhibit the intended efficiency increase [15]. An additional complication inherent to these designs is that they require a new fabrication technique for the solar cell itself, since the capture of high and low-energy photons occurs within the cell. In luminescent downconversion and upconversion, however, the active downconverting or upconverting layer can be simply added as a front or back-coat to an existing solar cell. Therefore, innovations in the cost-efficiency of silicon solar cells need not be sacrificed in the design of downconverter or upconverter-enhanced solar cells.

While both downconverting and upconverting materials retain this benefit of adaptability, theoretical considerations demonstrate that successful upconversion would produce the greatest benefit. As indicated in 2.1.2, the theoretical balance limit of a downconversion enhanced solar cell under unconcentrated solar radiation is 39.63%; however, under the same conditions, an upconversion enhanced cell demonstrates a limit of 47.6% [16]. Successful upconversion would produce twice the efficiency boost over the Shockley-Queisser limit as would downconversion, a highly compelling reason for the study of upconverting materials.

2.2.1 Fundamentals

In principle, photon upconversion can occur with any number of photons greater than one absorbed, and a single photon emitted. However, two-photon upconversion is the most common and simplest form of photon upconversion currently studied, and is the focus of this paper. Therefore, for the remainder of this paper, only two-photon upconversion will be considered, and will be simply referred to as *upconversion*.

Upconversion is fundamentally a simple process. A low-energy photon is absorbed by the upconverting material, creating an exciton in an intermediate state. A

second low-energy photon can then be absorbed, further exciting this exciton to its final, high-energy state. The exciton then can recombine to emit the high-energy photon. In principle, this can be accomplished such that there is no energy loss in the process, meaning that the energy of the emitted high-energy photon is equal to the sum of the two absorbed low-energy photons. This is referred to as 'perfect upconversion', and is depicted in Figure 2(b).

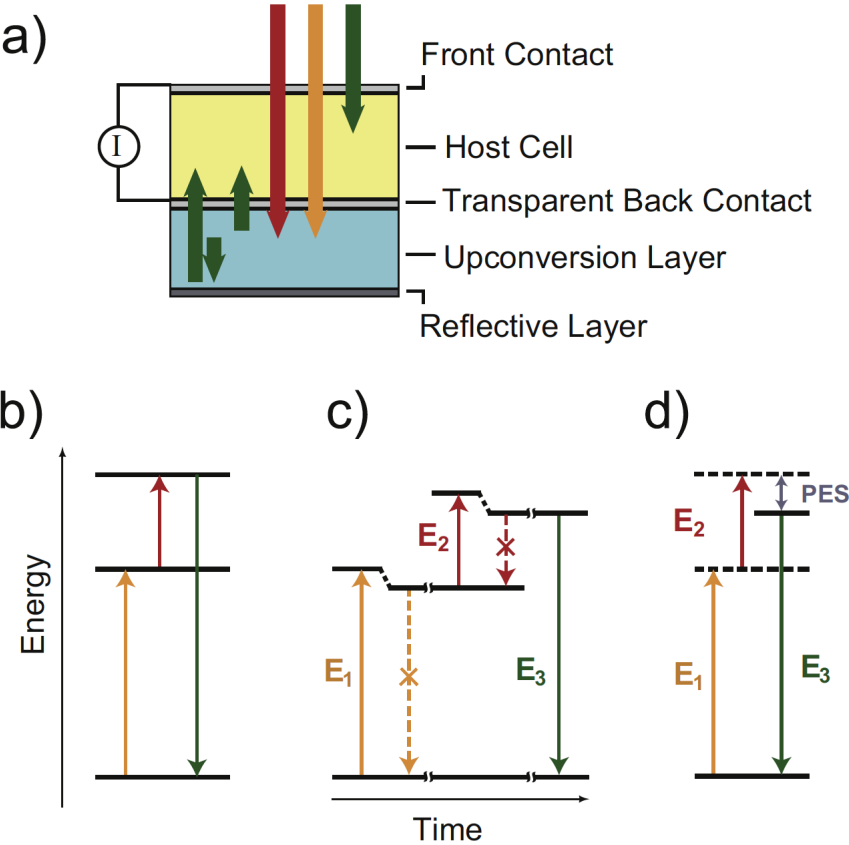


Figure 2: (a) Design of an upconverter-backed solar cell. High-energy photons (green) are absorbed in the cell, while low energy photons (orange and red) pass through the cell to the upconverting layer, where they are converted to high-energy light to be absorbed in the cell. (b) Depiction of perfect upconversion. (c) Depiction of upconversion with intentional energy loss introduced to suppress radiative (orange) and nonradiative (red) loss pathways. (d) Depiction of Photon Energy Sacrifice (PES) in the upconversion process [3].

While perfect or near-perfect upconversion is desirable for high energy conversion efficiency, it is in practice difficult to implement. In such an upconverting

structure, radiative and nonradiative pathways, essentially the reverse of the 'yellow' and 'red' absorption processes in [Figure 2\(b\)](#), compete with much higher probabilities against the preferred upconversion pathway [3] (note that colors are used in this figure only to indicate the relative energy of each involved photon, not the actual energy). Efficient upconversion therefore requires the suppression of these loss pathways. This suppression is typically introduced through the introduction of slight energy loss from each excited carrier state, as depicted in [Figure 2\(c\)](#). An exciton created from the absorption of an 'orange' photon might preferentially relax to the slightly lower energy state rather than immediately recombine. If recombination from this secondary state is forbidden, the upconversion process can now be driven forward with far less competition from recombination. After absorption of the 'red' photon, similar relaxation could occur, sending the exciton to a state in which the 'red' recombination is forbidden, but the 'green' recombination is allowed, hence completing the upconversion process.

The idea of intentionally-introduced loss in upconverting systems is critical to understanding and designing successful and efficient upconverters. The net energy loss during the upconversion is called the *photon energy sacrifice* (PES) [3]. [Figure 2\(d\)](#) depicts the concept of PES, defined as the combined energy of the absorbed photons less the energy of the emitted photon. PES is one of the critical performance metrics used to evaluate upconverters, which will be further explored in [2.2.2](#).

The design of an upconverter-enhanced solar cell is relatively straightforward. As shown in [Figure 2\(a\)](#), a conventional solar cell, consisting of the cell as well as front and back contacts, is backed by a layer of the upconverting material and a reflective layer. High-energy ('green') light is absorbed in the host cell, while the remaining low-energy, sub-band gap ('red' and 'orange') light passes through the cell and is absorbed by the upconverter. There, it is converted to 'green' light, which is then absorbed in the host cell. The reflective layer serves to reflect any unabsorbed solar radiation for a second pass through the cell and to reflect the isotropically emitted upconverted light towards the host cell.

2.2.2 Performance Metrics

Photon upconversion has been demonstrated by a variety of structures and materials systems, and theorized in even more. Because these designs often operate quite differently, it is necessary to define metrics to evaluate the performance of the upconverting structures for specific applications. For upconversion of solar radiation for photovoltaic applications, three especially important performance metrics have been defined: *upconversion quantum efficiency* (UQE), PES, and *absorption bandwidth* (AB) [3].

Upconversion quantum efficiency is perhaps the most intuitive measurement of the performance of an upconverter. UQE simply measures the ratio of emitted high-energy photons to incident or absorbed low-energy photons. UQE is often defined in two distinct ways - internal (iUQE), which measures the ratio of emitted high-energy photons to absorbed photons, and external (eUQE), which measures the ratio of emitted high-energy photons to incident photons. Because the latter generally depends on the density of upconverting structures within an upconverting layer, iUQE is the preferred method for quantifying the efficiency of an upconverting structure itself. In this paper, only iUQE is discussed, and is typically referred to as *quantum yield*. For two-photon upconversion, at least two low-energy photons are necessary to generate a single high-energy photon; therefore, the maximum ratio of upconverted to absorbed photons is 0.5, or an efficiency of 50%. While many papers report quantum yield on this scale, in this paper, the ratio of upconverted to absorbed photons is doubled when reporting quantum yield, such that a perfectly efficient upconverter would have the more natural quantum yield of 100%. All reported and referenced quantum yield values in this paper have been converted to this scale. In designing an upconverter, it is generally desirable to obtain high values of quantum yield; however, maximization of a single performance metric such as this often requires poorer performance by other metrics.

PES, or photon energy sacrifice, was discussed briefly in 2.2.1, and simply equates to the intentional energy loss introduced to drive the upconversion process

forward and suppress radiative and nonradiative loss. As demonstrated in [Figure 2\(d\)](#), PES is often composed of multiple loss components - in this figure, one after the first absorption, and one after the second. In semiconductor upconverters, for instance, the exciton consists of an electron in the conduction band and a hole in the valence band. In these structures, PES is composed of a conduction band component and a valence band component, which stabilizes the electron and hole, respectively (the details of semiconductor upconverters are further explored in the following sections). For photovoltaic applications in which the energy conversion efficiency is paramount, low PES values are desirable. However, decreasing the PES generally results in less favorable upconversion compared to the loss pathways, reducing the quantum yield.

The absorption bandwidth of an upconverting structure is another important consideration, particularly for photovoltaic applications. The AB of an upconverter is the range of low-energy wavelengths over which the upconverter can absorb and upconvert light. Since the goal of upconversion is to capture the low-energy light that is not absorbed by traditional silicon solar cells, a large AB is typically sought to maximize the impact of the upconverter. A high quantum yield, for instance, is not very meaningful if hardly any of the incident light can possibly be absorbed. However, increase the AB again requires with trade-offs in other performance metrics. Each transition, including both absorption and emission, within the upconverter is tuned to a specific photon energy. While higher-energy light can still create excitons in the absorptive transitions, the resultant upconverted photon does not have more energy than if the original, lower-energy photons were absorbed. Therefore, a larger AB will result in higher PES. Additionally, due to specific resonance wavelengths for each transition, not all wavelengths are upconverted with equal efficiency, meaning that a larger AB also will accompany a lower quantum yield.

These three performance metrics are the most critical in evaluating the performance of an upconverter. Because they are closely linked, the optimization of upconverters is very complex and requires careful consideration of trade-offs between the performance metrics. Rather than maximize or minimize any single metric, the effects

are weighed to determine the optimal design for a specific application. For photovoltaics, an overall measure of the success of an upconverter is the net increase in the overall efficiency of the enhanced solar cell. To achieve this optimization requires thorough knowledge and precise control of each aspect of upconverter performance.

2.2.3 Summary of Existing Materials

Multiple materials systems have so far been demonstrated to successfully upconvert light. The mechanisms by which upconversion is achieved varies based on the class of material. There are three such classes into which upconverting structures are generally divided: *lanthanide and transition-metal-ion*, *sensitized triplet-triplet annihilation* (TTA), and *quantum structures* [3].

2.2.3.1 Lanthanide and Transition-Metal-Ion Upconverters

Crystalline materials containing transition metal ions and doped with lanthanide ions are known for their ability to upconvert infrared radiation into visible radiation - salient characteristics for photovoltaic upconverters. A common lanthanide dopant is trivalent erbium (Er^{3+}). The energy levels associated with the ground and excited states of this ion are shown in [Figure 3](#), along with the wavelengths of transitions between these states.

The energy states of trivalent erbium reveal why this dopant is ubiquitous in lanthanide-based upconverters. It absorbs strongly in the infrared region at a wavelength of 1563 nm, below the band gap of silicon. If the ion is excited twice (corresponding to two curved arrows in [Figure 3](#)), by relaxing to its ground state it will re-emit an 800 nm photon, above the band gap of silicon. Multiple excitation of Er^{3+} occurs either by excited state absorption or by energy transfer. A common host lattice for this lanthanide dopant is NaYF_4 , chosen because it limits nonradiative loss due to low phonon energies [17]. In addition to erbium, trivalent ytterbium (Yb^{3+}) is often used as a dopant in lanthanide upconverters. The first excited state to ground state

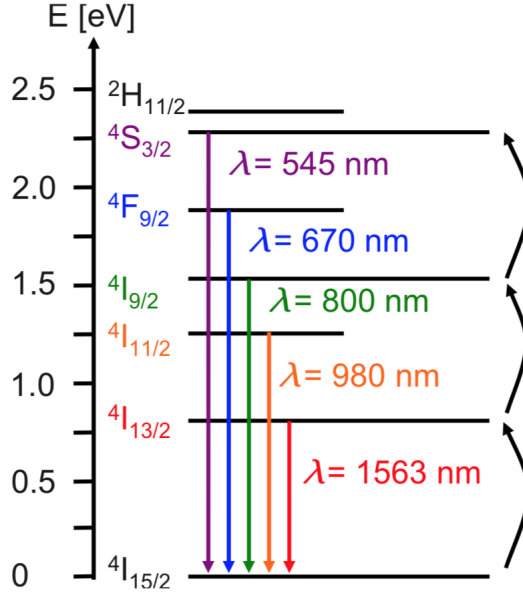


Figure 3: Energy levels and wavelengths of transitions of trivalent erbium. Successive excitation leading to upconversion is indicated by the curved arrows [17].

transition in Yb^{3+} matches in energy the 980 nm transition in Er^{3+} ; therefore, absorption of light by Yb^{3+} followed by energy transfer from the excited Yb^{3+} to the either ground state or excited Er^{3+} allows population of higher energy Er^{3+} states, causing visible emission [18].

In terms of quantum yield, lanthanide structures generally perform well. NaYF_4 : $\text{Er}^{3+}/\text{Yb}^{3+}$ structures have demonstrated quantum yield values of up to 12% [18]. However, because these upconverters tend to emit visible light substantially more energetic than the silicon band gap, they are better suited for solar cells with larger band gaps where energy conversion of visible light is more efficient, such as GaAs. Another upconverting structure, BaY_2F_8 : Er^{3+} , emits strongly near 1000 nm, a more well-suited wavelength for silicon solar cells, and has demonstrated a higher quantum yield of 20.2% for 30% Er^{3+} -doped samples [1]. Despite the higher quantum yield, however, BaY_2F_8 : Er^{3+} -enhanced silicon solar cells demonstrate lower calculated overall efficiency than do NaYF_4 : $\text{Er}^{3+}/\text{Yb}^{3+}$ -enhanced GaAs cells [3].

While lanthanide-based upconverters offer promising quantum yield, their performance is limited by the remaining performance metrics. The PES values observed in these materials are moderate; in NaYF₄: Er³⁺/Yb³⁺ structures, values in the range of 0.16-0.47 eV are observed [3], and in the BaY₂F₈:30% Er³⁺ structures, the PES is approximately 0.4 eV [1]. The more major limiting factor to their performance for photovoltaic applications, however, is their narrow absorption band. Because the transitions within the structures that lead to upconversion are atomic, they absorb over only a small range of wavelengths. NaYF₄: Er³⁺/Yb³⁺ structures have an AB of only 0.13 eV, centered at approximately 980 nm [19], while BaY₂F₈:30% Er³⁺ structures have an even more narrow AB of 0.08 eV, centered at 1493 nm [1]. Although the quantum yield of lanthanide upconverters is high, computational modeling predicts a maximum efficiency of 33.4% for a NaYF₄: Er³⁺/Yb³⁺-enhanced GaAs solar cell (band gap of 1.42 eV), only a slight improvement over the original 33% detailed balance limit for GaAs [3]. Even in this optimistic case for upconverter with promising quantum yield, the impact on solar technology is minimal, thus lanthanide upconverters possess severe fundamental limitations for photovoltaic applications.

2.2.3.2 Sensitized Triplet-Triplet Annihilation

An alternative means of upconversion to lanthanide-based atomic transitions is triplet-triplet annihilation (TTA). TTA systems consist of a sensitizer compound and one or more acceptor compounds. The sensitizer compound is typically either a Pt(II) or Pd(II) porphyrin, and the acceptor compound is often 9,10- diphenylanthracene (DPA). A diagram of the upconversion process within one such system, using Pt(II) octaethylporphyrin (PtOEP) as the sensitizer and both DPA and 1,3- diphenylisobenzofuran (DPBF) as acceptors, is shown in [Figure 4](#).

Absorption occurs in the sensitizer (PtOEP), which is excited to a singlet state (S₂) by a 2.33 eV photon. Internal conversion (IC) and intersystem crossing (ISC) transform this singlet into a triplet state, and energy transfer (ET) populates the triplet state of an acceptor (either DPA or DPBF). Triplet-triplet annihilation can

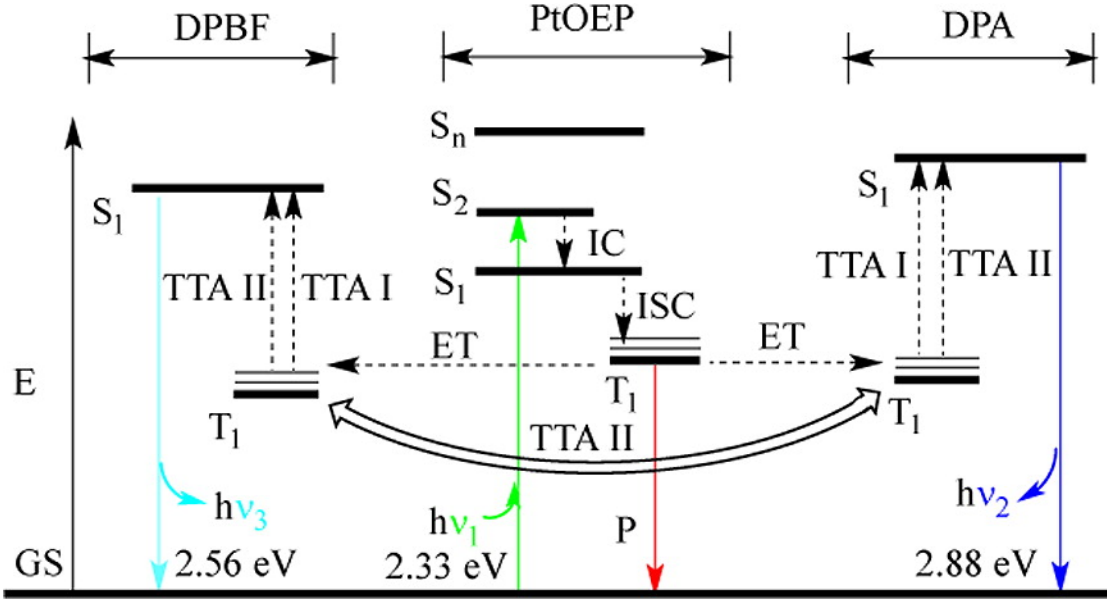


Figure 4: Schematic of the upconversion process within a TTA system. Solid lines represent radiative transitions, while dashed lines represent nonradiative transitions. 'S' denotes a singlet state, 'T' denotes a triplet state, and 'TTA' represents either a homo (I) or hetero (II) TTA pathway [2].

then occur either between two triplets of the same type (homo-TTA) or of different types (hetero-TTA) - represented by TTA I and TTA II, respectively - to populate the acceptor singlet state. Finally, upconverted emission occurs at either 2.88 eV in DPA or 2.56 eV in DPBF.

The primary advantage of TTA systems is their high values of quantum yield. The multiacceptor system shown in Figure 4 has demonstrated a quantum yield of 32% [2]. In single-acceptor PdOEP/DPA systems, a maximum measured quantum yield of 36% is reported [20]. Both of these observed quantum yield values are well in excess of the highest observed quantum yields of lanthanide upconverters.

While the upconversion quantum yield of TTA systems is excellent, these upconverters have many drawbacks that limit their applicability to photovoltaics. From Figure 4, it is immediately evident that the wavelengths pertinent to TTA are incompatible with silicon photovoltaics. Photons with energy of 2.33 eV - those absorbed by the sensitizer - are well above the silicon band gap, so upconverting them is only of

use to solar cells with large band gaps. Because cells with band gaps of this size have limiting efficiencies much lower than that of silicon solar cells, even highly effective TTA systems cannot match the efficiencies of modern single-junction silicon cells. For instance, the detailed balance limit of a solar cell with a band gap of 2.75 eV is 8.01% [3].

TTA systems are further limited by their AB and PES. As is evident from the proximity of the absorbed and emitted photon energies in Figure 4, the emitted photons do not nearly have equal energy to two absorbed photons. The minimum PES reported for TTA systems is 0.54 eV, above the maximum reported values for lanthanide upconverters, while the maximum PES of 1.34 eV is greater than the band gap energy of a silicon solar cell [3]. Such high energy losses are prohibitive in efficient energy conversion. Additionally, TTA systems share the same limitations in AB as lanthanide upconverters. The ground state to singlet transition in the sensitizer is a molecular transition resonant with a specific wavelength, and therefore has a narrow linewidth. Therefore, the resulting AB is only 0.08 eV wide, posing another severe limitation in efficient energy conversion, as much of the sub-band gap light is still not absorbed by the TTA upconverter [4]. Combined with the high PES, this narrow AB negates the potential benefit of high quantum yield. Even for a 100% quantum yield Pd(II) tetraphenylporphyrin/DPA system (with absorption at 2.37 eV), the maximum efficiency of a TTA enhanced 2.75 eV band gap solar cell would only be 10.8%, still far below the efficiency of commercially available solar cells [3].

2.2.3.3 Quantum Structures

The lanthanide and TTA classes of upconverters are fairly well defined in terms of the materials and structures that successfully upconvert. Upconversion in quantum structures, on the other hand, has been accomplished and theorized for a variety of structures and a variety of materials systems. In quantum upconverters, the mechanisms of upconversion vary more substantially than in those previously discussed upconverter classes. The commonality between these structures is that, due to their

size, often on the order of nanometers, quantum mechanical effects are essential in producing upconversion.

Perhaps one of the more simple examples of a quantum upconverting structure is the colloidal CdTe quantum dot nanoparticle. In these structures, there are four pertinent energy states: the valence band maximum (VBM), the conduction band minimum (CBM), the hole surface states (HSSs) and the electron surface states (ESSs). The states are situated such that the HSS and ESS are within the band gap defined by the VBM and CBM, with the ESSs approximately 0.8 eV below the CBM and the HSSs about the same energy above the VBM. Therefore, sub-band gap photons cannot populate the VBM or CBM directly, but some can populate the ESSs and HSSs. These electrons/holes can then be thermally excited to the CBM/VBM, and recombination will give a higher-energy photon than that absorbed. Due to the thermal excitation, this upconversion is not two-photon, and actually exhibits a *negative* PES, with net energy gains of up to 360 meV reported [21]. Additionally, because the transitions are no longer atomic or molecular, the absorption band is far wider than in lanthanide or TTA upconverters.

While CdTe quantum dot nanoparticles have demonstrated the promise of upconverting quantum structures, more complex quantum structures have been proposed to allow greater control over the properties and performance metrics of the upconverters. These structures have most commonly been either colloidal - like the CdTe quantum dots - or fabricated on semiconductor substrates by molecular beam epitaxy. Epitaxially grown quantum structures allow for much more precise control during fabrication, giving structures with complex composition profiles. An example of the band structure of an InAs-based epitaxial upconverter is shown in [Figure 5](#). In this structure, absorption of the first low energy photon (1) creates an exciton in the InAs quantum dot (QD). The valence band gradient in the InAlBiAs layer preferentially guides the hole towards the recombination zone (2), allowing for stabilization of the electron in the QD. There, this electron is excited by another photon (3), after which the conduction band gradient in the InAlBiAs layer guides the electron towards the recombination

zone (4). Finally, the exciton recombines to give upconverted emission (5) [3].

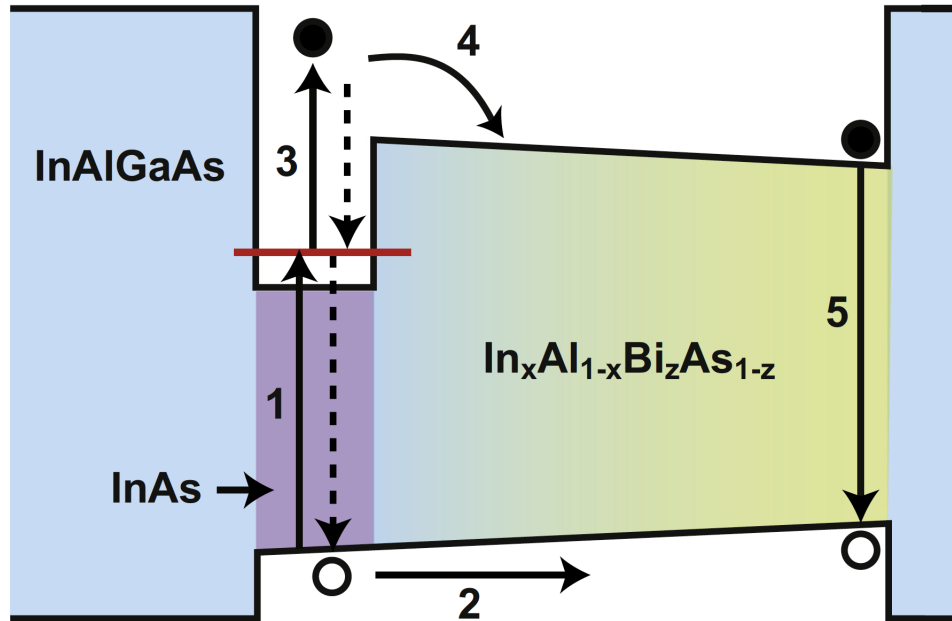


Figure 5: Band diagram of an epitaxial upconverting quantum structure. The upconversion process consists of exciton generation (1), hole migration (2), secondary electron excitation (3), electron migration (4), and recombination (5). [3].

Modeling of these upconverters reveals the advantages of upconverting quantum structures. Because the transitions involve electronic states in bands, substantial absorption can occur over a much wider range than in other classes of upconverters. The structure demonstrated in Figure 5, for instance, is predicted to have an AB of approximately 0.8 eV, nearly an order of magnitude larger than that of lanthanide or TTA upconverters. At moderate PES, models indicate that the epitaxial structure can demonstrate excellent quantum yield - 96% yield at a PES of 550 meV, and over 75% PES of below 400 meV. For a GaAs host solar cell, this performance would result in an overall efficiency in excess of 39% [3]. However, high-efficiency upconversion in this design of epitaxial structure has not yet been demonstrated experimentally. In a slightly simpler design of epitaxial upconverter, InAs/AlGaAs on a GaAs substrate, upconversion quantum yield has only been observed on the order of 0.1%, much lower

than has been theorized and than has been demonstrated in other classes of upconverters [22]. Besides the failure to demonstrate high quantum yield, epitaxial upconverters are limited by their high fabrication costs, reducing their viability in photovoltaic applications.

Colloidal quantum nanostructures provide a much more cost effective alternative to epitaxial structures. The upconversion mechanism in colloidal nanostructures tends to be quite similar to that in epitaxial structures, only lacking the ability to create precise valence and conduction band gradients to guide carrier diffusion. Colloidal structures also share the salient features of large AB and moderate-to-low PES. Two structural designs of colloidal quantum nanostructures have been explored in detail: core-shell and core-rod. The former assumes a spherical geometry, with a core surrounded by multiple outer layers, or shells; the latter takes an anisotropic rod-like shape with quantum dots on either side. Core-shell nanostructures have demonstrated successful upconversion with the PbSe/CdSe and PbSe/CdSe/CdS material systems. However, the quantum yield of these systems has been limited to 0.4% [23] and 0.8% [24], respectively. For the core-rod structure, the CdSe(Te)/CdS/CdSe material system has demonstrated an internal conversion efficiency of nearly 0.1% [25]. However, since this figure represents the probability of upconversion given that a double excitation event has occurred, the quantum yield of these structures is likely substantially lower. Additionally these upconversion measurements were taken under pulsed excitation at 0.1 mJ/cm² and above, representing conditions well above solar-relevant fluences. While quantum structures in general have yet to demonstrate high quantum yield, the potential of these structures in improving solar conversion efficiency necessitates further work to realize their limitations.

2.2.4 Heterostructure Engineering of Core-Rod Colloidal Semiconductors

While colloidal core-shell semiconductor quantum structures have demonstrated the ability to upconvert light, they have not done so efficiently. This inefficiency is in a large part due to poor spatial separation of the electron and hole after initial excitation.

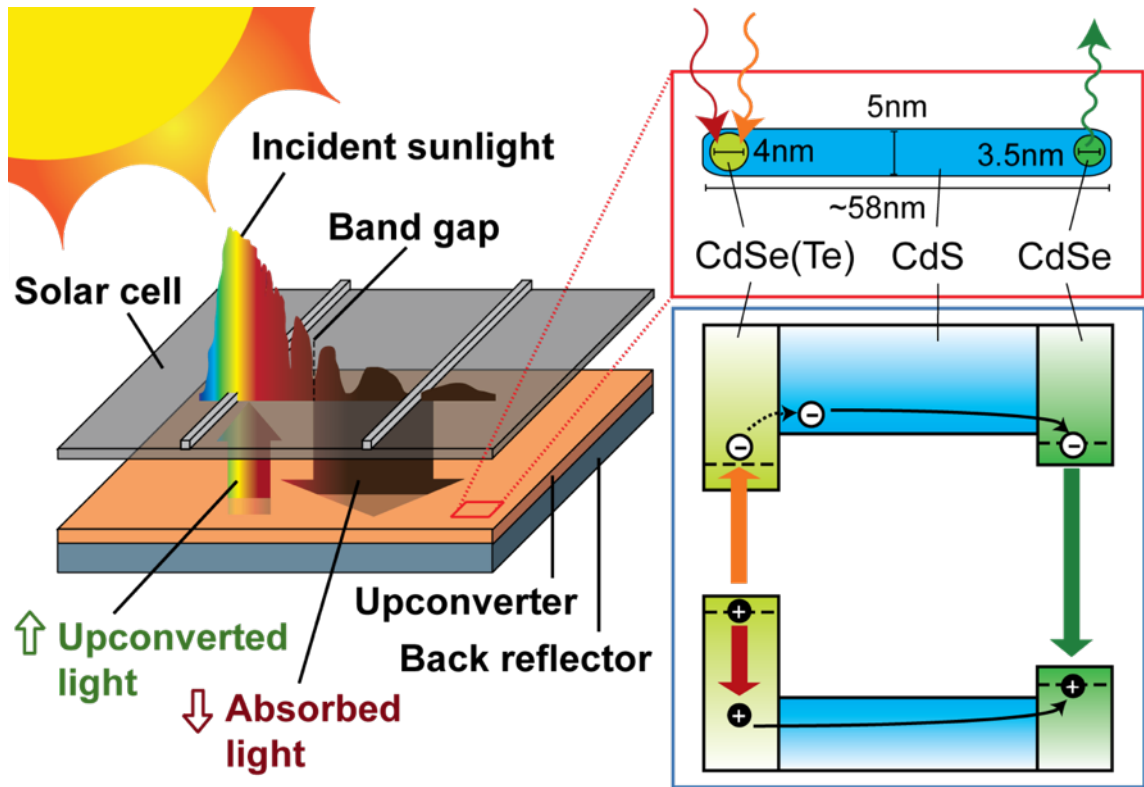


Figure 6: Schematic of an upconverter-backed solar cell under solar radiation (left). Depiction of the physical dimensions and structure of a CdSe(Te)/CdS/CdSe core-rod upconverter (boxed in red). Diagram of the upconverter band structure (boxed in blue), showing interband absorption (orange arrow), intraband absorption (red arrows), carrier migration (black arrows), and emission (green arrow).

This poor separation inhibits the stabilization of carriers within the core QD, and allows fast recombination before a second excitation event. While adding intermediate shells between the absorption and emission regions improves the separation slightly, the use of a core-rod structure separates the regions far more. Colloidal upconverters of this core-rod structure will be the focus of the remainder of this paper.

A depiction of a solar cell backed by CdSe(Te)/CdS/CdSe core-rod upconverting nanostructures is shown in Figure 6. The upconversion process here is essentially the mirror of the process in the epitaxial system, with the second excitation now occurring with a hole in the valence band. A few important features from the band diagram in Figure 6 should be noted. Firstly, the depicted diagram assumes that the band edge is

flat within each section of material. For the CdSe quantum dot, this remains the case, but it is not always true for the CdS rod and the CdSe(Te) quantum dot. Depending on the synthesis technique employed, the composition within these regions might be nonuniform, and the band edges may be graded rather than flat (roughly resembling a 'step-stool' in the core and a taper in the rod). Optimizing the design of the structure involves studying whether graded or uniform composition in the core or rod results in better performance of the upconverter. While this engineering decision is critical in the design of these core-rod upconverters, the upconverters studied in this paper are all graded-core homogeneous-rod structures.

A second important feature evident in the band diagram is that the addition of some tellurium (Te) doping in the core quantum dot raises the valence band edge and lowers the conduction band edge as compared to pure CdSe. This change alters the optimal wavelengths for the red and orange transitions shown in the diagram. Because the exact position of the band edges depends on the extent of Te-doping in the core, adjusting the Te-doping allows control of the wavelengths that can be absorbed by the upconverter. In particular, increasing the Te-doping red-shifts the orange transition, thereby widening the absorption band in the low-energy direction. This increased AB might correlate to better overall upconverter performance in photovoltaic applications. However, the effect of the Te-doping on the yield of the structures cannot be straightforwardly predicted without thorough computational modeling or experimentation. Investigating the effect of Te-doping on the performance of core-rod upconverters will be a major focus of this paper, both through gathering data needed to assemble a computational model and through direct observation of the quantum yield of core-rod upconverters with varying Te-doping.

2.3 Synthesis

The synthesis of all core-rod upconverters studied in this paper was performed by Dr. Christopher Milleville, a postdoctoral researcher in the Doty Group, using the materials and methods described below. Besides the mixing ratio of the selenium

and tellurium solutions during the synthesis of the cores, the synthesis conditions were kept constant for all samples, so that the only variations between samples was in the Te-composition of the cores.

2.3.1 Materials

Anhydrous cadmium acetate (CdAc, 99.995%), cadmium oxide (CdO, $\geq 99.99\%$), oleylamine (OA, 70%), selenium (Se), trioctylphosphine (TOP, 90%), and trioctylphosphine oxide (TOPO, 90%) were purchased from Sigma-Aldrich. Hexylphosphonic acid (HPA, $\geq 99\%$), octadecylphosphonic acid (ODPA, $\geq 99\%$), and tetradecylphosphonic acid (TDPA, $\geq 99\%$) were purchased from PCI Synthesis. Tellurium (Te) was purchased from Acros Organics. 1-octadecene (ODE, 90%) was purchased from Alfa Aesar. Toluene, acetone, and ethanol were purchased from Fischer Scientific. All reagents used in the synthesis of the core-rod upconverters were used without further purification.

2.3.2 Synthesis of CdSe(Te) Cores

The synthesis procedure for the CdSe(Te) cores was adapted from previously reported methods [25]. To begin, 0.1 M stock solutions of Se:TOP and Te:TOP were prepared by separately dissolving 2 mmol of Se and Te each in 2 mL of TOP. A separate solution of 0.15 mmol CdO, 0.3 mmol TDPA, and 8 mL of ODE was prepared and degassed, then heated to 300 °C under argon flow. At this point, a 1mL mixture of the Se:TOP and Te:TOP solutions was added in the desired Te/Se ratio. In this paper, four doping ratios are studied: 4% Te, 10% Te, 20% Te, and 40% Te. After injection, nucleation and growth of the CdSe(Te) quantum dot cores proceeded, and was stopped by removal of the heating mantle. The resulting cores were purified by solvent/antisolvent washing in toluene/ethanol and dispersed in 1 mL of TOP.

2.3.3 Growth of CdS Rods

To anisotropically grow CdS rods, the methods reported by Carbone *et al.* were followed [26]. A solution of 0.67 mmol CdO, 0.9 mmol ODPA, 0.5 mmol HPA, and 8 mmol TOPO was prepared and degassed, then heated to 350 °C under argon flow.

At 300 °C, when CdO dissolved, 2 mL of TOP was injected. The dispersion of the CdSe(Te) cores was separately mixed with 3.7 mmol of S in 2 mL of TOP, then injected into the heated CdO solution for 4 minutes before heating was removed. The resulting nanorods were twice precipitated by acetone and dissolved in toluene, before a final precipitation and dissolution in 1 mL TOP.

2.3.4 Growth of CdSe Quantum Dot

Using a procedure modified from previously reported methods [25], the CdSe quantum dot was grown on the tip of the nanorod opposite from the core by successive ionic layer adsorption and reaction (SILAR). First, Cd:TOP (0.09 mol CdAc:2.25 mL), Se:TOP (0.2 mmol:5 mL), and S:ODE (0.3 mmol:8 mL) solutions were prepared. A solution of 4.7 mmol TOPO, 2 mL OA, and 2 mL ODE was prepared, degassed, heated to 80 °C, and injected with the nanorod solution before heating to 200 °C. Then, 1 mL Se:TOP followed by 0.5 mL Cd:TOP were added dropwise by 0.1 mL every 10 minutes. Finally, 0.4 mL S:ODE followed by 0.2 mL CD:TOP were added in 0.1 mL portions over the course of 90 minutes, after which heating was removed. The resulting nanostructures were purified by the same acetone/toluene procedure as in 2.3.3, and dispersed in toluene for storage. A summary of the synthesis procedure with accompanying TEM images of aliquots following each major step is shown in Figure 7.

2.4 Computational Modeling

Computational modeling of upconverting quantum structures is a critical facet of the engineering procedure. Models serve as a proof of concept for novel structures, provide a critical tool for optimizing the upconverter design, and can provide deeper understanding to the physics and the limitations of upconverter performance. Constructing a robust computational model is also much more time and cost efficient than carrying out multiple rounds of synthesis and characterization to reach an optimal design.

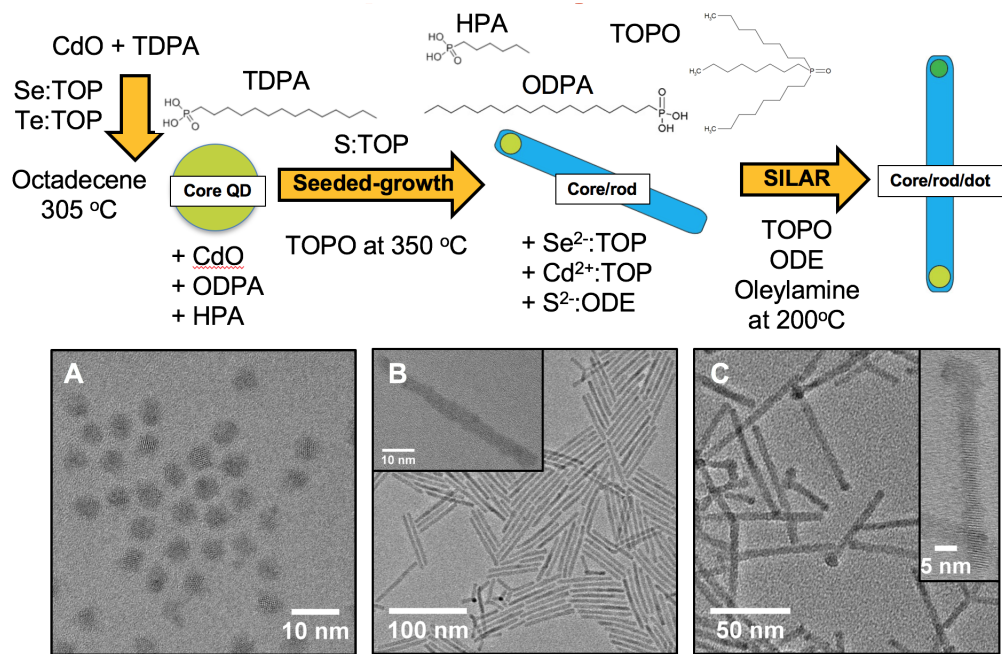


Figure 7: The major reactants and reaction steps for the synthesis of CdSe(Te)/CdS/CdSe upconverting nanorods. Transmission electron microscope (TEM) images of (a) the CdSe(Te) cores, (b) the CdSe(Te)/CdS core/rods, and (c) the CdSe(Te)/CdS/CdSe core/rod/dot structures [27].

While through modeling of the CdSe(Te)/CdS/CdSe core-rod system has not yet been completed, a computational framework has been established for the InAs-based system depicted in Figure 5. While this model is slightly different due to different material properties, the framework is largely the same, and the predictions given by the model are very instructive in examining the potential of the core-rod upconverter. Figure 8 shows the framework (including relevant rate constants) of the kinetic model for the InAs-based system, and demonstrates the similarity of this system to the core-rod system.

The subprocesses that make up the upconversion process, indicated by 10 separate rate constants, are listed in Table 1. In this table, $n_{x,y}$ represents the number of carriers in state 'x', and 'y' represents the carrier type - either electron (e) or hole (h). The maximum occupancy of the QD is represented by n_c , and E1, E2, and E3 correspond to the orange, red, and green energy gaps, respectively, in Figure 8.

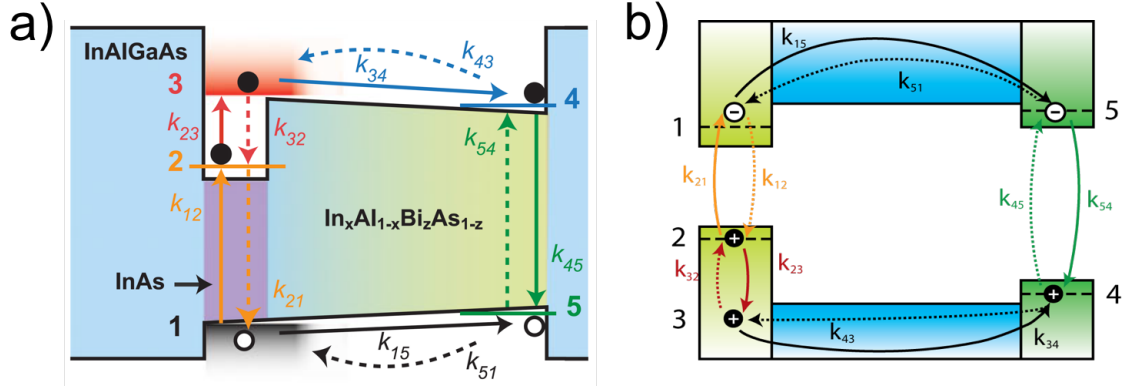


Figure 8: (a) Kinetic model of upconversion in InAs-based epitaxial quantum structures. Solid arrows show the direction of the upconversion process, dashed arrows show the direction opposite from preferred [5]. (b) The framework of a kinetic model for CdSe(Te)/CdS/CdSe colloidal core-rod quantum structures, showing the high degree of similarity with the model in (a).

For well studied systems such as the InAs-based quantum structures, the values of these rate constants can be found in or approximated from literature. For novel material systems or for accurate modeling of specific synthetic batches, many of these parameters can be obtained through optical characterization. In particular, the radiative (k_{21} and k_{45}) and nonradiative (k_{32}) relaxation rates can be extracted from Time-Resolved Photoluminescence (TRPL) and transient absorption (TA) spectroscopy, respectively. While the details of TA, a pump-probe method by which the time-correlated absorption of a sample is measured to determine the population decay lifetime of an excited state, are not explored further in this paper, the details of TRPL are explored thoroughly in 3.3.

Using literature data for rate constants, the kinetic model of the InAs-based structure demonstrates the exceptional promise of this system, and similar systems, in photovoltaic applications. Specifically, these structures can reach a maximum upconversion quantum yield of 96%, and can attain high quantum yield values at a moderate PES of 400 meV [5]. For realistic host solar cell materials, this performance would result in historic solar cell efficiencies for upconverter-enhanced systems - above 40% for CdTe (1.51 eV band gap) and CGS (1.62 eV band gap), and above 39% for GaAs (1.42

Table 1: Descriptions and expressions of rates used in the kinetic model for the InAs-based system depicted in [Figure 8\(a\)](#). Adapted from [\[5\]](#).

Rate constant	Description	Expression
k_{12}	Incoming photon absorption rate for E1	$k_{12} \cdot (1 - n_{2,e}(t)/n_c)$
k_{21}	Radiative recombination rate for electrons in state 2 with holes in state 1	$k_{21} \cdot n_{2,e}(t) \cdot n_{1,h}(t)$
k_{23}	Incoming photon absorption rate for E2	$k_{23} \cdot n_{2,e}(t)$
k_{32}	Relaxation rate of electrons in continuum band into ground or first excited state of QD, depending on filling	$k_{32} \cdot n_{3,e}(t) \cdot (1 - n_{2,e}(t)/n_c)$
k_{34}	Relaxation rate of electrons in state 3 to recombination zone, state 4	$k_{34} \cdot n_{3,e}(t)$
k_{43}	Diffusion of electrons from recombination zone to QD	$k_{43} \cdot [n_{4,e}(t) - n_{3,e}(t)] \cdot \exp(-\Delta E_{CB}/k_B T)$
k_{15}	Relaxation rate of holes in state 1 to recombination zone at state 5	$k_{15} \cdot n_{1,h}(t)$
k_{51}	Diffusion of holes from recombination zone to QD	$k_{51} \cdot [n_{5,h}(t) - n_{1,h}(t)] \cdot \exp(-\Delta E_{VB}/k_B T)$
k_{45}	Radiative recombination rate for electrons in state 4 and holes in state 5	$k_{45} \cdot n_{4,e}(t) \cdot n_{5,h}(t)$
k_{54}	Absorption rate of a photon with energy equal to or higher than E3	k_{54}

eV band gap). Plots of the PES-dependent quantum yield (for a GaAs host cell) and of the overall cell efficiency as a function of both PES and host cell band gap are shown in [Figure 9](#), demonstrating the promise and versatility of this upconverter. Although the placement of the absorption and emission bands in the colloidal core-rod system vary slightly from the epitaxial structure might cause the performance to change slightly, and the lack of a band edge gradient in the CdS layer will likely diminish performance slightly, these model predictions justify optimism about the performance of the core-rod structures. To prove these optimistic predictions for the core-rod structure requires an adjusted kinetic model as well as direct observation of their upconversion photoluminescence.

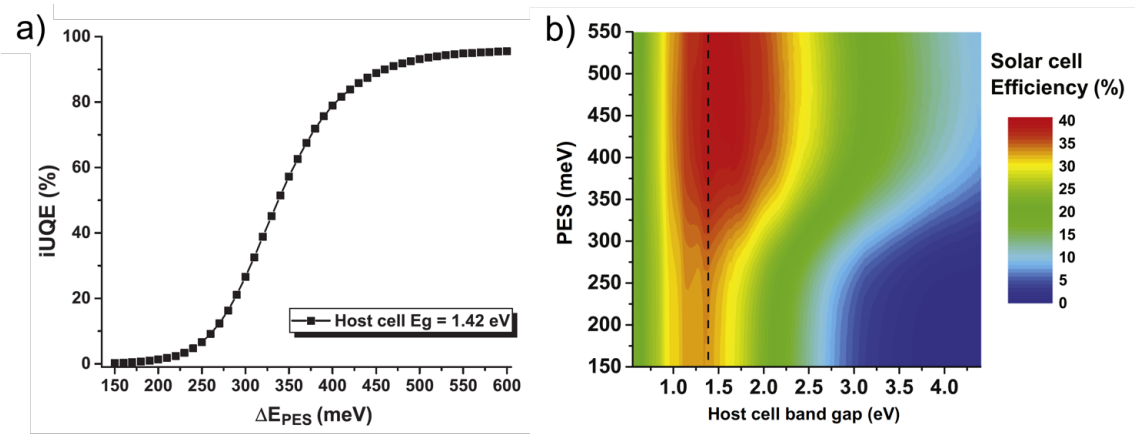


Figure 9: (a) Upconversion quantum yield of the epitaxial quantum structure as a function of PES for a GaAs host cell [5]. (b) Overall solar cell efficiency for a variable host cell band gaps backed by epitaxial upconverting structures of variable PES. The dashed line indicates a GaAs host cell [3].

Chapter 3

CHARACTERIZATION METHODS

In this chapter, the effects of heterostructure engineering of colloidal semiconductor nanostructures on upconverter performance, carrier dynamics, and photophysics are explored through four different optical characterization techniques. As was discussed in 2.2.4 the structures under study in this chapter are CdSe(Te)/CdS/CdSe double quantum dot nanorods with a compositionally graded core quantum dot (CdSe(Te)) and a compositionally homogeneous rod (CdS). In this engineering study, the varied design parameter is the Te-doping content of the core quantum dot. In particular, four samples were synthesized with different Te-doping percentages in the core - 4%, 10%, 20%, and 40% Te-doping - while attempting to hold all other device parameters, such as the rod length and size of either quantum dot, constant. Due to the smaller band gap of Te relative to Se, it is expected that an increase in Te-doping would allow utilization of lower energy light by the upconverters, providing a relative increase in the AB. The focus of this chapter is to determine the effectiveness of this heterostructure engineering by characterizing the overall performance of the synthesized upconverters.

To fully characterize the upconverting nanostructures, the characterization methods discussed in this chapter should accomplish four major goals: (1) verify that the structures upconvert light; (2) determine the mechanism(s) by which the structure upconvert light; (3) measure the lifetime(s) associated with radiative recombination within the structures; and (4) quantify the efficiency of upconversion within the structures. These goals are to be accomplished via steady-state photoluminescence, excitation power dependence, time-resolved photoluminescence, and quantum yield measurements, respectively. The results of each goal are then compared to determine the effect of Te-doping in the core on the upconverter performance.

3.1 Steady-State Photoluminescence

The measurement of photoluminescence, the emission of light by matter after the absorption of photons, is essential to the characterization of any optical material. PL measurements involve transforming emitted photons into electrical signal, but variation in the measurement scheme can yield quite different data. In this section, one such variation, called *steady-state photoluminescence* (PL) is explored.

3.1.1 Motivation and Background

Steady-state PL involves the measurement of the intensity of light emitted by a sample upon steady-state, or time-invariant, excitation. These PL measurements often involve wavelength-dependent diffraction to spatially separate different emitted wavelengths in order to obtain a portion of the emission spectrum of the sample. In the case of CdSe(Te)/CdS/CdSe upconverting quantum structures, this emission spectrum provides valuable information about the performance and underlying physics. When light with energy above the band gap of the CdSe emitter quantum dot is used to excite the sample, steady-state PL measurements are here referred to as 'down-conversion' PL, while excitation with below band gap light gives upconversion PL measurements. In this paper, 'down-conversion' PL will simply be abbreviated as PL, while upconversion PL will be abbreviated as UCPL.

PL measurements of the full upconverting structures have two peaks, one with emission at wavelengths corresponding to the band gap of the CdSe(Te) absorber quantum dot (the 'absorber peak'), and another at wavelengths corresponding to the band gap of the CdSe emitter quantum dot (the 'emitter peak'). UCPL measurement, on the other hand, focus primarily on the high-energy emitter peak. By comparison of the center wavelength and shape of this peak in the UCPL spectrum with the same features of the emitter peak in the PL spectrum, a pair of PL and UCPL measurements can indicate whether successful upconversion is occurring. Specifically, if an emitter peak is observed in the UCPL spectrum with the same features as the emitter peak in

the PL spectrum, the former must be due to upconverted emission from the emitter quantum dot.

In addition to providing this critical determination of successful upconversion, PL measurements can also provide a rough idea of the practical performance of the upconverters. Because, for semiconductors, the emission peak occurs at approximately the band gap energy, the PL absorber peak should indicate the distribution of absorber band gaps in the nanoparticle ensemble. Since this same energy is also the onset of absorption, the location of the absorber peak gives the minimum energy needed to excite the interband absorber transition, and its width indicates the relative distribution of quantum dot sizes within the colloidal ensemble. While the minimum energy necessary to excite the interband absorber transition is important to know, it does not provide information about the minimum energy necessary to excite the intraband transition within the absorber, which might be less than the minimum for the interband transition, and provides no knowledge as to the wavelengths of higher energy light that can be absorbed. To quantify the full absorption band, absorption measurements must be taken. Besides providing insight to the absorption features of the upconverter, the energetic difference between the absorber and emitter peaks in the PL spectrum also indicates the energy gain of the upconversion process, relative to the interband absorption. For solar applications, an increased energy gain generally indicates that the lower energy portions of the solar spectrum can be more efficiently upconverted to useful light. Quantification of the PES, however, is more difficult than examining this energy gain alone; it requires not only knowledge of the emission wavelength and minimum interband absorption wavelength, but knowledge of the minimum intraband absorption wavelength, which is difficult to obtain from PL and traditional absorption measurements.

While simple steady-state PL and UCPL measurements are a powerful analysis tool for upconversion, slight modifications in the experimental setup or procedure can expand the breadth of information available by PL and UCPL. In particular, measurements of UCPL spectra at different excitation powers can elucidate the nature of

the upconversion mechanism in the structure (see 3.2), and precisely calibrated UCPL spectra can be used to measure the upconversion quantum yield of the structure (see 3.4). In this section, only simple PL and UCPL measurements are explored, taken using a free-space setup with the primary goal of validating successful upconversion in the synthesized nanoparticles.

3.1.1.1 Diffraction Grating

One important feature of PL spectroscopy is the resolution of the wavelength-dependence of the intensity of emitted light. This requires splitting a beam of mixed wavelengths into component wavelengths. In common spectrometers such as that used in this paper, this is accomplished by a diffraction grating. These gratings are governed by a 'grating equation' similar to Bragg's Law ($n\lambda = 2d\sin(\theta)$), stating that the angle of maximum reflection is related to the incident wavelength and the spacing within the grating. Therefore, adjusting the spacing of the grating allows sharper spectral resolution. In this paper, a grating with 150 grooves/mm is used, which gives a spectral resolution of about 0.25 nm over a spectral range of 350 nm.

3.1.1.2 CCD Silicon Spectrometer

Another important feature of PL spectroscopy is the transformation of photons into electrical signals. While multiple devices that accomplish this exist, that employed in the PL measurements within this paper is a charge-coupled device (CCD) silicon spectrometer. In general, this device consists of a thin silicon photoactive layer grown on a substrate and biased with a positive voltage. Due to the bias voltage, a 'depletion zone' is created where all holes are deeply embedded in the substrate and no mobile electrons exist at the surface. When a photon arrives at the device, it generates an electron-hole pair, and the hole migrates towards the substrate while the electron migrates to the surface. Pair generation is allowed over a specified time window, referred to as the 'integration time'. This process occurs separately in individual 'pixels', which are ordered in a square array. Once integration is complete, the voltage within each

pixel is controlled to transfer charges downward to the bottom pixel of each column, at which point all charges are transferred to an amplifier and converted to a voltage, resulting in the final electrical signal. Due to the spectral resolution from the diffraction grating, each column of pixels corresponds to a different wavelength, generating the PL spectrum which is read by a connected computer.

3.1.2 Methods

Simple PL and UCPL measurements were taken using a free-space setup assembled on an optical table. Via a series of mirrors, the beam from an excitation laser source was directed through two alignment irises to a microscope objective. This objective focused the beam to a point at which the sample rested on an x-stage. All samples were contained in glass cuvettes as colloidal dispersions with an optical density of approximately 0.5. The resulting photoluminescence from the sample was collected within a small solid angle by another nearby microscope objective, which collimated the light into a beam. This beam was further directed by mirrors into a spectrometer, within which a diffraction grating separated the wavelengths and concave mirrors directed the light onto the silicon CCD. This experimental setup is shown in [Figure 10](#).

For PL measurements using above band gap excitation, a continuous-wave (CW) diode laser with peak emission at 412 nm was used. For UCPL measurements, a Ti:Sapph laser with tunable emission in the 700-800 nm range was used. The wavelength of this excitation beam could be adjusted to find the optimal excitation wavelength for upconversion. Alternatively, a Fianium WhiteLase pulsed laser, with tunable emission between 400-1100 nm could be use in this setup for both PL and UCPL measurements. Because the repetition rate for this laser is always above 0.1 MHz, giving a repetition period many orders of magnitude below the typical 0.25 or more second integration time of the CCD, PL measurements taken with this pulsed source could be approximated as steady-state. However, due to the short pulses from this laser, the excitation intensity during a single pulse is much higher than in CW lasers; not only

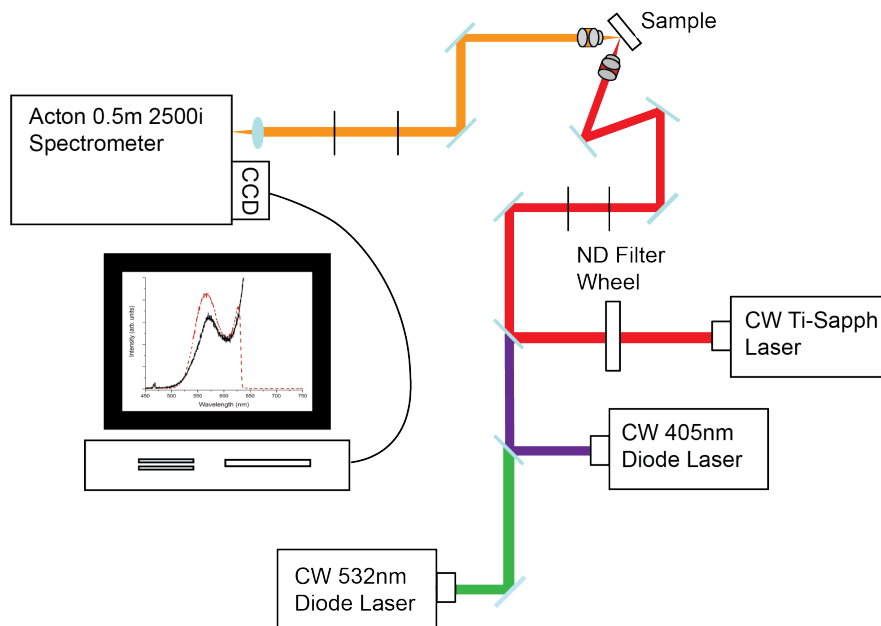


Figure 10: The experimental setup for free-space photoluminescence measurements. The excitation beam (either red, purple, or green here) is directed through a microscope objective to the sample, and PL/UCPL (UCPL shown in orange) is collected through an objective and directed to the spectrometer and CCD for measurement by a computer.

might this high intensity introduce non-linear effects, but it also represents excitation intensities orders of magnitude higher than solar intensity. Because CW excitation represents more solar-relevant conditions, it is therefore much more valuable to observe PL and particularly UCPL under CW excitation.

Once the excitation beam had been aligned through the pre-sample irises and through the focusing microscope objective, the PL from the sample was directed through the spectrometer to the CCD. The signal was read by a computer via a Lab-View program, which allowed measurements to be continually taken with a repetition rate equal to the specified integration time. The position of the sample was adjusted via an x-stage, and the path of the PL beam was aligned through a series of mirrors and lenses to maximize the PL signal read by the computer.

To isolate the PL or UCPL signal and to ensure only the proper laser wavelengths reach the sample for excitation, multiple pre- and post-excitation filters were used. For PL measurements using the 412 nm diode laser, a 405 nm long-pass (LP)

filter was placed at the entrance of the spectrometer. LP filters have a high optical density (OD), meaning very low transmission, at wavelengths below their nominal cutoff, but transmit nearly all light above that cutoff. Therefore, this LP filter greatly reduced the laser signal entering the spectrometer. Although the peaks under observation were typically more than 100 nm away from the laser wavelength, an excess of laser photons incident on the CCD could cause saturation of pixels and unwanted charge-spillover into adjacent columns, so efforts were always made to reduce the laser signal entering the spectrometer. In the case of intense PL signal above the saturation threshold for the CCD, neutral density (ND) filters, with wavelength-independent OD, were placed at the entrance to the spectrometer to reduce the photon flux to the CCD.

For UCPL measurements, more complex filtering was often required to properly observe upconversion signal. Just after the laser source, 700 nm or 750 nm LP filters (depending on the chosen excitation wavelength) were placed to ensure that only below band gap light reached the sample. If, due to poor laser performance, any high-energy photons from the laser could reach the sample, they could generate PL without upconversion, thus producing a false UCPL signal. After excitation, multiple 650 nm and 750 nm short-pass (SP, essentially the opposite of LP) were placed at the spectrometer entrance to reduce the laser signal without cutting off a substantial portion of the UCPL emitter peak (typically around 600 nm). UCPL signal was typically low, so ND filters were not required. Once the proper filtering was in place, and the alignment was optimized, a PL or UCPL spectrum was obtained and saved as a text-file for analysis.

3.1.3 Results

To begin characterizing the performance of the upconverting samples based on the goals set forth at the beginning of this chapter, PL spectra were taken for each sample to capture the emission features of both the CdSe(Te) absorber and the CdSe emitter quantum dots. These spectra were taken with CW above band gap excitation at 405nm and 10mW, which when focused to a spot size of approximately 1 mm² gives a radiant flux of 1 W/cm². Multiple spectra were concatenated to produce a

single spectrum spanning both features, which is shown for each case in [Figure 11](#). In general, each structure has an absorber peak centered near 800nm and an emitter peak centered near 600nm. This information is critical because, when the sample is excited with sub-emitter band gap light (i.e. light with energy between the absorber band gap and the emitter band gap), the resulting upconversion peak should match the emitter peak at 600nm observed here. Therefore, the 'downconversion' PL spectrum provides the basis for determining whether true upconversion is observed.

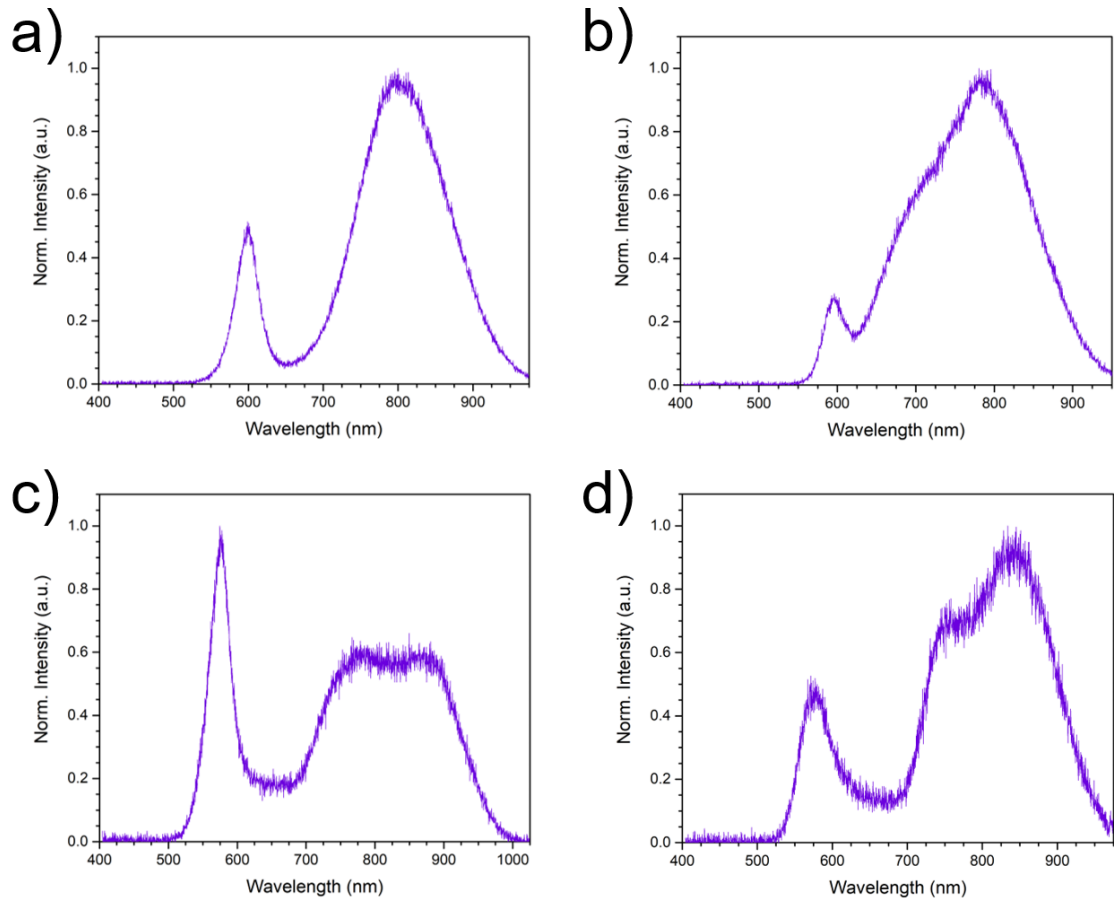


Figure 11: Normalized steady-state PL spectra obtained via excitation with a 405nm CW laser at 1 W/cm^2 for (a) 4% Te-doping, (b) 10% Te-doping, (c) 20% Te-doping, and (d) 40% Te-doping.

Along with serving as a reference for the UCPL spectra, these PL spectra contain practical information about each structure. The center wavelength of the absorber

Table 2: Key features of the PL spectrum for each upconverting sample.

Sample	Absorber Peak Center (eV)	Absorber Peak FWHM (eV)	Energy Gain (eV)
4% Te-doping	1.55	0.26	0.52
10% Te-doping	1.59	0.37	0.49
20% Te-doping	1.46	0.40	0.69
40% Te-doping	1.48	0.33	0.67

peak indicates the approximate band gap energy for the CdSe(Te) absorber in each structure, and the width of this peak indicates the homogeneity of upconverters within the colloidal ensemble. Additionally, because it is expected that increasing Te-doping in the core should create a narrower band gap in the absorber, and therefore a red-shifted absorber peak, the absorber center wavelength provides a metric for confirming that the synthesized structures match expectations. Further, the separation between the centers of the absorber and emitter peak centers indicates the approximate upconversion energy gain, a useful metric for evaluating the viability of the upconverters in solar applications. The values of each of these metrics for each sample are tabulated in [Table 2](#).

Once the PL spectrum for each sample was collected, the laser source was switched to a 735nm Ti:Sapph CW laser, operating at a power of 100mW. Using this laser, again focused onto a 1 mm² spot size to give a radiant flux of 10 W/cm², UCPL spectra for each sample were obtained. Because the UCPL intensity was in general much weaker than the PL intensity, longer integration times were required to visualize the spectra. However, as the relative intensity of upconversion is not assessed in this section, these spectra were scaled to match the corresponding normalized PL peaks. The scaled UCPL spectra overlaid with the corresponding PL spectra are shown in [Figure 12](#).

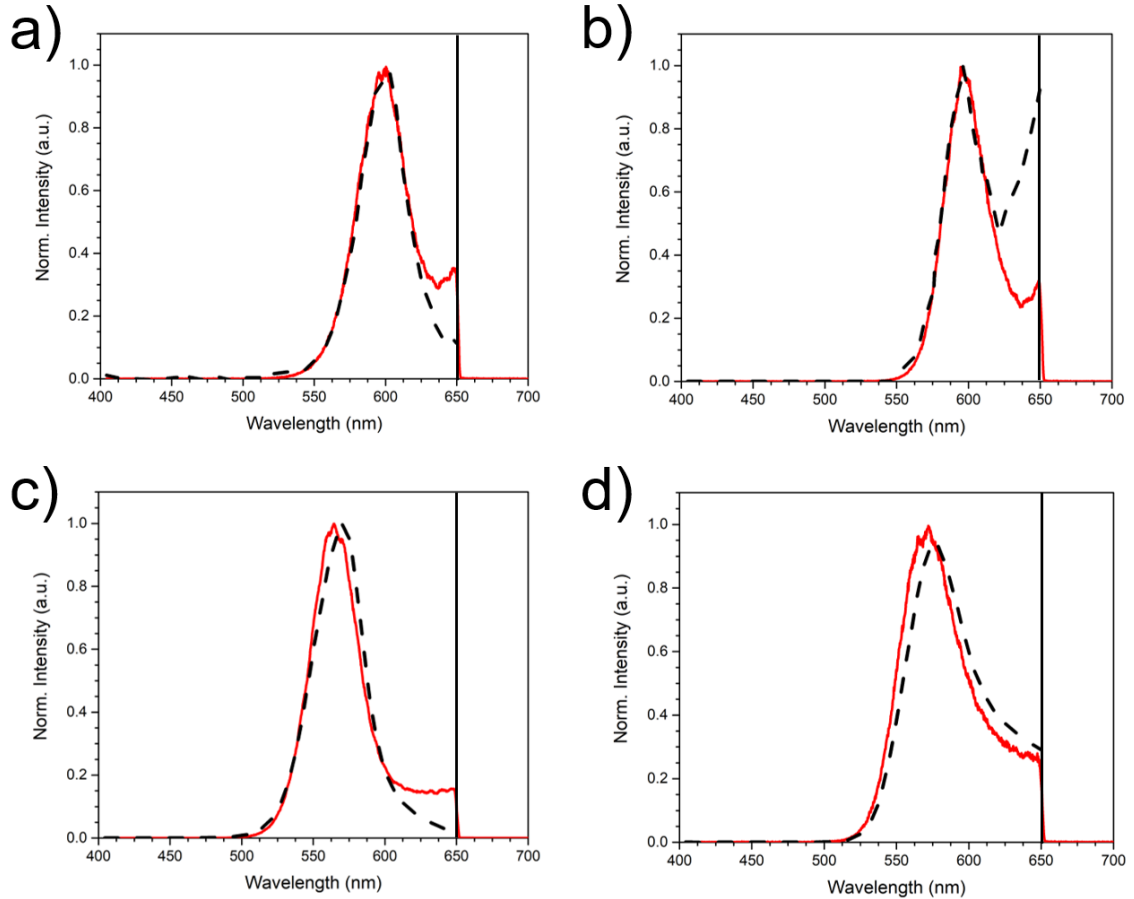


Figure 12: Normalized steady-state UCPL spectra (red) obtained via excitation with a 735nm CW laser at $10\text{W}/\text{cm}^2$ overlaid with corresponding PL spectra (dashed) for (a) 4% Te-doping, (b) 10% Te-doping, (c) 20% Te-doping, and (d) 40% Te-doping. A 650nm SP filter was used for all measurements.

3.1.4 Analysis

The most significant takeaway from the spectra presented in the preceding section is that, in [Figure 12](#), the emitter peak from the UCPL spectrum aligns very well, both in center wavelength and in peak shape, with the emitter peak from the PL spectrum for each structure. For the UCPL experiments, because the energy of the laser photons is lower than the band gap energy of the emitter quantum dot in all structures, direct exciton generation within the emitter quantum dot is impossible. However, the matching of the emitter peak in the UCPL spectrum to the PL spectrum indicates that photons are emitted from the emitter quantum dot in the UCPL

experiments; therefore, *this confirms that upconversion is occurring within the structures*. These measurements represent the first measurements of upconversion in the CdSe(Te)/CdS/CdSe material system under CW excitation, as opposed to previous measurements under pulsed excitation [25]. This is a significant advance in the field, as it demonstrates the viability of these upconverters at near solar-relevant conditions.

It is important to note that these spectra not only demonstrate upconversion, but confirm that this upconversion occurs via excitation within the absorber quantum dot and emission in the emitter quantum dot, as is the desired mechanism. This distinction is critical because, as is also evident in [Figure 12](#), there is a substantial elevated 'tail' on the low-energy side of the emitter peaks in the UCPL spectra. If the UCPL emanates solely from the emitter quantum dot, the UCPL spectra should each take a purely Gaussian shape as expected for an ensemble of quantum dots. This asymmetric tail, however, indicates the presence of upconverted emission from outside of the emitter, most likely from the absorber. While still technically upconverted emission, this feature likely derives from phonon-mediated upconversion, and indicates a potential loss pathway for the desired upconversion mechanism that can potentially damage the overall upconverter performance. It is also important to note that, while these spectra do confirm the presence of upconverted emission from the emitter, they do not confirm that this upconversion is by the expected two-photon mechanism. This photophysics is examined in [3.2](#).

In addition to successfully verifying the presence of upconverted emission from the emitter quantum dot, the PL spectra shown in [Figure 11](#) and important metrics given in [Table 2](#) provide further insight to the workings of and potential issues with the synthesized structures. By visual examination of the PL spectra alone, it is immediately apparent that the shapes of the PL spectra, specifically the shape of the absorber peak, vary significantly between samples. Because the absorber peak should result from an ensemble of quantum dot emission peaks, the overall shape should be Gaussian. For the 4% sample, that is approximately the case, but at higher Te-doping levels the absorber peak is highly non-Gaussian. In fact, at high Te-doping levels, the absorber

peak appears to be composed of two separate, but highly overlapping, Gaussian peaks. There are two possible explanations for this irregular peak shape. The first is that the shape is due to the compositional inhomogeneity of the core. As was mentioned in 2.2.4, the synthetic methods used in this paper result in absorber dots which are compositionally graded. Because this gradient results from the formation of a Te-rich center and a Se-rich outer shell within the absorber dot, increased Te-doping would exacerbate the difference between the center and outer regions of the absorber dot. This could result in the formation of two distinct states within the absorber, a low energy state and a metastable higher energy state. Emission from both states would result in the overlapped peak shape. The second explanation is that some unknown synthetic challenge results in the creation of two distinct sub-ensembles of upconverters with slightly different absorber dot features. During synthesis, this might unknowingly and randomly drive upconverters down two slightly different synthetic pathways, resulting in a bimodal distribution within the total ensemble, and giving the observed peak shape.

While it is difficult to determine which of these two challenges is the likely cause of the irregular peak shape, both represent undesired consequences of synthesis that might harm upconverter performance and inhibit the direct analysis of Te-doping on upconverter performance. For instance, the presence of the compositional gradient or bimodal distribution appears to reduce the band-gap tuning capabilities desired from changing the Te content of the core, as is evident from the lack of trend in absorber peak center demonstrated in Table 2. While the 20% and 40% samples do show a lower-energy absorber center than the 4% and 10% samples, there is no clear trend otherwise, as is the case with the absorber peak FWHM and the energy gain. Additionally, the relative peak intensity of the absorber and emitter peak varied widely between samples. Combined with the variability of the absorber peak center and shape, this indicates that synthetic challenges could be limiting the ability to keep factors besides the Te-doping level constant. It may therefore be difficult to isolate the effects of Te-doping in the forthcoming analyses.

3.2 Excitation Power Dependence

Simple steady-state PL and UCPL measurements can provide critical insight to the performance of upconverting structures, such as their AB and PES. However, by measuring and systematically varying the power of the exciting laser, further insight to the photophysics involved in the upconversion process - something not attainable through a single PL measurement - is revealed. This section focuses on these power-dependent UCPL measurements.

3.2.1 Motivation and Background

Based on the proposed model for the CdSe(Te)/CdS/CdSe upconverting structures, the upconversion process is expected to involve two photon absorption events per emitted photon. This expectation forms the basis for kinetic modeling of the upconversion structure, which strictly follows the two photon process. It is also critical in evaluating the performance of upconverters and in adjusting design parameters to improve performance. However, synthesized upconverting structures are often imperfect and might not obey the same upconversion mechanism as in computational models. Without knowledge of the true upconversion mechanism, any design using a two-photon model might be useless. Therefore, it is essential to know if the proposed mechanism of two-photon upconversion is truly occurring in any synthesized upconverters, or if another competing process is taking place that may involve more or less absorbed photons.

Along with the upconversion mechanism, it is important to know the maximum capacity of carriers an upconverting structure can accommodate at a given time. Specifically, because the absorber quantum dot contains discrete states in which it can hold holes, there are a limited amount of holes which can reside in the absorber at a given time. This leads to a phenomenon called saturation, an effect which occurs when the incoming photon flux is high enough to produce enough carriers to maintain the absorber dot at maximum carrier capacity. Beyond this saturation point, additional photon flux will not increase the rate of exciton generation, but can only affect the rate

at which excitons are excited for a second time to continue the upconversion process. Therefore, it is not desired for the saturation point to be below the operating photon flux, since the potential effects of many of these photons are limited to the second excitation event only. Knowledge of the saturation point is important in determining the range of photon fluxes over which an upconverter can most efficiently operate.

To determine the order of the upconversion mechanism and the saturation point of an upconverting structure, the dependence of UCPL intensity on excitation power density is measured. The nature of the relationship between the excitation power density and the intensity of the UCPL spectrum can reveal both the photophysics of the upconversion process and the point of saturation in the sample.

3.2.1.1 Power-Law Relations

Measuring the dependence of UCPL intensity on excitation power density is a powerful tool in determining the *order* of a photoluminescence mechanism such as upconversion. The order of a photoluminescence mechanism is comparable to that of an elementary chemical reaction in that it indicates the quantity of 'reactant' species involved in the process. In the case of photoluminescence, a single absorbed photon represents a 'reactant' species, and therefore the order of the process is simply the number of absorbed photons necessary to complete the photoluminescence mechanism (because emitted photons are like reaction 'products', and not 'reactants', they do not count towards the order of the mechanism).

In chemical kinetics, the rate of reaction is determined by the product of reactant concentrations for each reacting species. The same is true in photoluminescence mechanisms, only now the 'reactant concentration' can be thought of as the incident photon intensity, and the 'rate of reaction' as the emitted photoluminescence intensity. For n absorbed photons involved in a photoluminescence mechanism, the relationship between PL intensity and the excitation (e) intensity is given by [Equation 1](#).

$$I_{PL} = \prod_{i=1}^n I_e = I_e^n \quad (1)$$

From Equation 1, it is evident that the logarithm of the PL intensity will linearly depend on the logarithm of the excitation intensity with a slope equal to n . This relationship has been used to evaluate the nature of the upconversion mechanism in many structures [4, 21, 23, 24, 25, 28, 29, 30], and it is well established that a slope (n) of 1 corresponds to a one-photon process, while a slope of 2 corresponds to a two-photon process [28]. Higher slopes than 2 have also been attributed to physical processes; a slope of 3, for instance, is due to Auger-mediated upconversion consisting of both an electron-electron-hole and a hole-hole-electron process [30]. Because two-photon upconversion is expected to be the dominant process in CdSe(Te)/CdS/CdSe structures, the expected slope for the log-log power dependence is 2.

3.2.1.2 Saturation

In the nanorod upconverting structures, the first, interband absorption event results in the generation of a hole within the core quantum dot. Because this hole is within a quantum well, there are a limited number of states that it can occupy. Each nanostructure has a maximum capacity of holes in the core quantum dot, leading to a maximum capacity of confined holes in a colloidal suspension of nanostructures. At low excitation intensities, the rate at which this state is populated does not exceed the rate at which holes leave this state, and the maximum capacity is not reached. At some value of the incident excitation intensity, therefore, the rate of hole generation within the core will equal the rate that holes escape the core quantum dot, and the maximum capacity of holes within this dot for the suspension of structures is reached. Beyond this excitation intensity, the population of this state will not increase with increasing excitation intensity. The onset of this behavior is the *saturation point* for the nanostructures.

Returning to the discussion of power-law relations in the above section, before the saturation point, the upconversion mechanism depends on the photon absorption rate of two separate processes, the interband and intraband excitations. By Equation 1, for two 'reactant' steps, a quadratic dependence is observed, and the slope of a log-log

power dependence is 2. Beyond saturation, however, the population of the hole in the core quantum dot is constant with increasing excitation intensity, and the mechanism no longer depends on the interband absorption. The mechanism becomes effectively a linear, one-photon process after saturation, and a log-log slope of 1 is observed. The roll-off from a slope of 2 to a slope of 1 in the log-log plot indicates the point at which the interband absorption is saturated for a given upconverting nanostructure, an important value for determining the relevant photon fluxes for most efficient upconversion.

3.2.2 Methods

The procedure for taking excitation power dependent UCPL measurements was not substantially different than that of simple steady-state UCPL measurements described in 3.1.2 and shown in 10. The Ti:Sapph laser was tuned to an appropriate wavelength and directed to the sample stage via a series of mirrors and alignment irises. Before reaching the sample for excitation, the laser passed through several LP filters (700 or 750 nm, depending on the laser wavelength) to ensure that only low-energy light reached the sample. Additionally, the laser passed through an ND filter wheel. This wheel contained a rotational-gradient ND, so that by rotating the wheel, the ND of the point through which the laser passes either increased or decreased. By rotating this wheel, the excitation intensity was controlled to allow for UCPL measurements at variable excitation intensity. Immediately before each UCPL measurement was taken, the attenuated laser power was measured between the ND filter wheel and the sample to give the excitation intensity value for a given UCPL measurement.

The post-excitation setup was exactly the same as for other steady-state UCPL measurements, where the UCPL was collimated by a microscope objective and directed to the spectrometer and CCD for collection. Once an UCPL spectrum was obtained, the CCD-recorded photon counts were added across the emitter peak. While this integrated counts value did not indicate the actual emitted UCPL intensity, it provided a relative measurement for comparison between data points. The logarithm of the integrated peak counts was then plotted against the logarithm of the excitation intensity to

give the power dependence curve, from which the order of the process and, if a roll-off in slope exists, the saturation point was determined.

3.2.3 Results

To assess the dependence of the UCPL intensity on the excitation laser power, each sample was excited with 745nm CW laser with varying attenuation by the ND filter wheel, and the resulting UCPL integrated intensity was compared to the excitation power on a log-log bases. These series of UCPL spectra at varying power and determination of the log-log slope for the all samples are shown in [Figure 13](#).

To explore the behavior of the upconverters at high laser fluences, the excitation power was further increased until the data deviated from its low-power slope. This roll-off point corresponds to saturation of the absorber quantum dot. After the point of saturation, the photon absorption rate for the interband transition in the absorber dot has reached a steady-state value, and is no longer dependent on the photon flux. Therefore, after saturation, the log-log slope of the excitation power dependence should equal unity. Such behavior is shown in [Figure 14](#).

3.2.4 Analysis

What is immediately evident from this figure is that the slopes, between 1.2 and 1.4, are very far from the ideal slope of 2 for the desired two photon upconversion process. This extreme deviation is, in part, due to the convolution of two separate upconversion 'peaks', as was discussed in [3.1.4](#). The low-energy peak coordinates to upconversion emitted from the emitter dot (the 'desired upconversion'), as it matches closely with the shape of the emitter PL spectrum. The second 'peak' coordinates to the elevated higher-energy tail, just before the short-pass filter. This upconversion derives from phonon-mediated interactions which provide extra energy to charge carriers within the absorber dot, resulting in higher-energy emission. Because this mechanism involves only one photon, it has a log-log slope of 1, thus its presence decreases the overall log-log slope. However, because the nature of the desired upconversion is unknown,

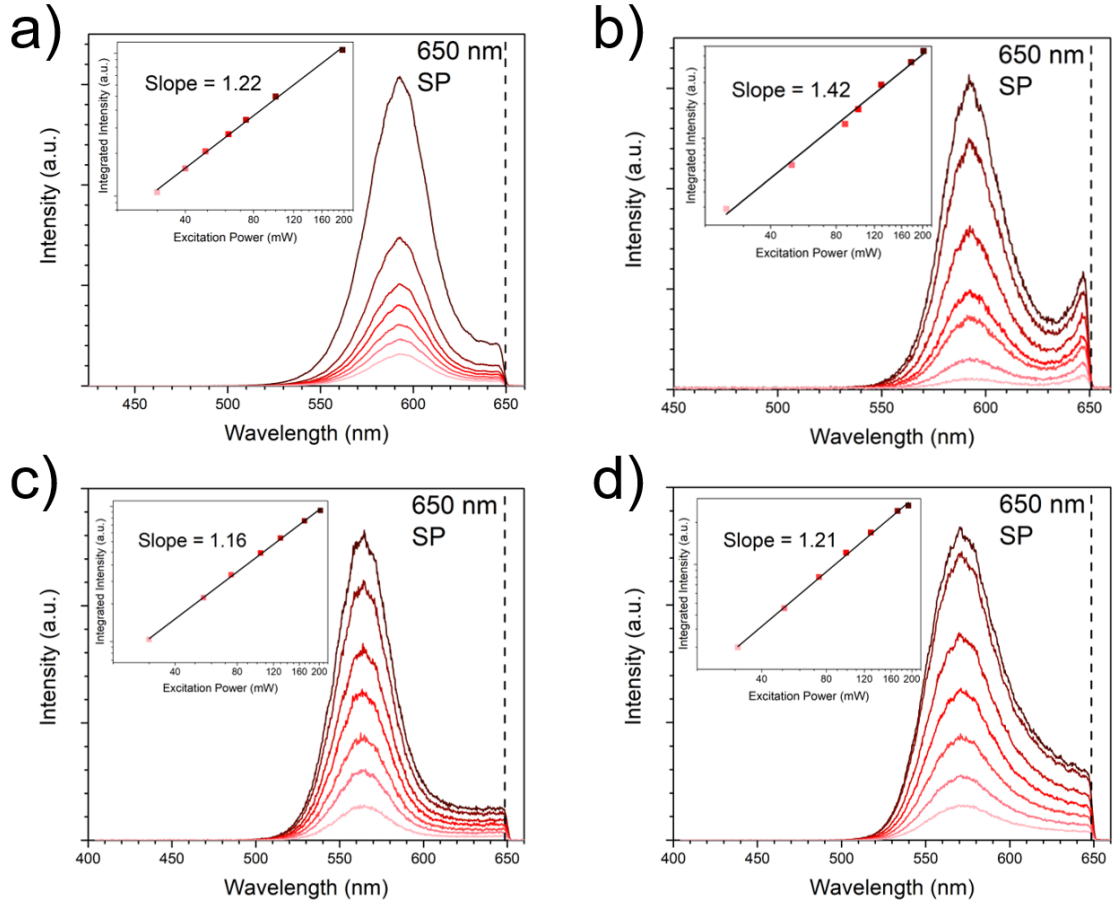


Figure 13: Several UCPL spectra for (a) the 4% Te-doped sample, (b) the 10% Te-doped sample, (c), the 20% Te-doped sample, and (d) the 40% Te-doped sample, taken at varying 745nm CW laser powers. The incident laser power is indicated by the curves color in coordination with the x-axis of the inset. The inset shows the log-log plot of integrated peak counts vs. incident power, showing the log-log slope.

it is not known whether the effect of the phonon-assisted upconversion is the only factor decreasing the log-log slope. A more accurate determination of the dependence of the desired upconversion on the excitation power requires further data processing involving the deconvolution of the emitter Gaussian peak from the low-energy absorber tail. For power dependence measurements for these samples, such data processing has not been conducted for this work. However, techniques to carry out this deconvolution are discussed in 3.4 and in Chapter 4, which can be applied to power-dependence measurements in the future.

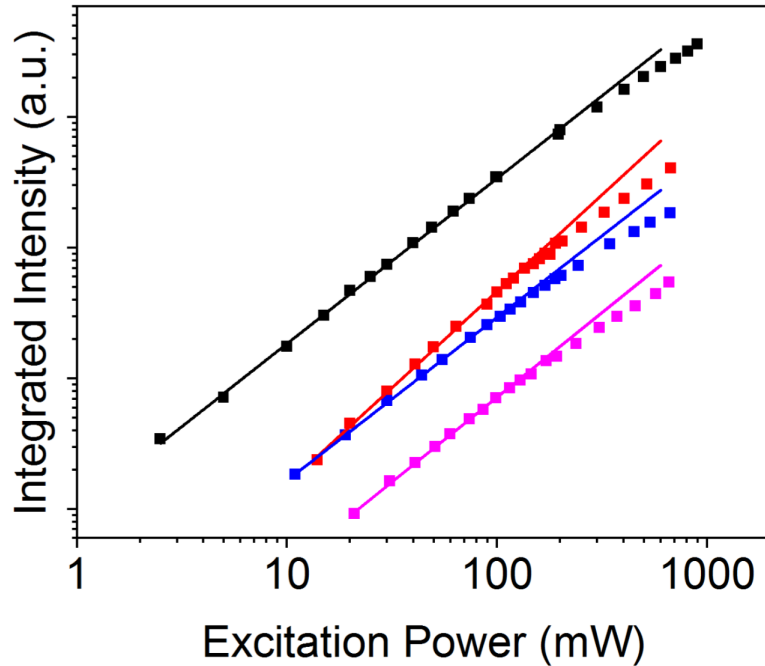


Figure 14: The extended log-log power dependence relation for the 4% (black), 10% (red), 20% (blue), and 40% (pink) Te-doped samples, showing saturation effects in the neighborhood of 100-200 mW excitation power.

While the low log-log slopes of the power dependence measurements indicate that undesired effects are occurring in the upconverting structures, rather than the desired pure two-photon upconversion, any trends in the slope with respect to varied Te-doping can indicate effects of Te-doping on the photophysics of the upconverters. However, as can be seen from [Figure 13](#), there is no trend in the slope with the Te-doping. Rather, the 10% sample exhibits a slope much higher than the other three samples, which all have very similar slopes. Therefore, it does not appear that Te-doping has any clear effects on the power dependence of upconversion in the structures, and therefore on the mechanisms of upconversion. However, these unpatterned variations indicate that some other unforeseen and undesired differences exist between the structures which has caused the variations in the log-log slope. These differences likely evolved from slight variations during synthesis, and might be problematic in future analysis of the effects of Te-doping, as any unknown or unwanted differences between the structures

will make it difficult to isolate the effects of Te-doping alone.

The final piece of important information available from power dependence measurements is the saturation point for each structure. As can be seen in [Figure 14](#), the data points begin to deviate from the low-power slope at around 100 mW. In particular, the 10%, 20% and 40% samples seem to saturate at a power between 100-200 mW, while the 4% sample saturates at a slightly higher value at or slightly above 200 mW. Because the laser spot size was approximately 1 mm^2 , these powers coordinate to photon fluxes of approximately $10\text{-}20 \text{ W/m}^2$. These saturation fluxes are about two orders of magnitude larger than the solar photon flux, indicating that, while upconversion occurs at solar relevant fluxes, saturation occurs at a flux higher than is solar relevant. While it is especially not ideal to have a saturation point below the solar photon flux, meaning that more solar photons will be wasted due to the inability of the structures to accommodate the solar flux, it is most optimal to have a saturation point near the flux at which the upconverter will operate. This ensures that the upconverter will be used near its fullest potential, as the absorber dot will have a carrier population always near its saturation population, while still not operating at a flux that gives more photons than the upconverter can absorb at steady state. The saturation point can be lowered to a more solar relevant condition by increasing the absorption within the absorber dot, such that more of the incident photons result in excitons within the dot and the dot will reach saturation at a lower incident flux.

3.3 Time-Resolved Photoluminescence

While still a photoluminescence measurement, *Time-Resolved Photoluminescence* (TRPL) is fundamentally very different from the steady-state PL measurements explored in the previous sections. It differs in the measurement procedure and equipment as well as in the information it provides about upconverting structures. While a steady-state PL measurement is independent of time, and explores the spectral properties of a structure, a TRPL measurement holds the measurement wavelength fixed and explores the dynamics - the time-dependent aspect - of photoluminescence.

3.3.1 Motivation and Background

The goal of TRPL is to provide a decay profile for a given radiative transition. This decay profile indicates how the population of an excited state decreases with time due to either radiative or nonradiative recombination or loss pathways. These decay traces can be fit to multi-exponential decay curves from which the lifetimes of various decay pathways from a state are extracted, giving critical insight to the carrier dynamics within the upconverting structure.

The first essential use of these decay lifetimes is in the computational modeling of the upconverting structures. As was discussed in 2.4, the rate constants of the interband recombination steps in both the emitter quantum dot and the absorber (core) quantum dot are required in the model, and both of these lifetimes can be extracted from TRPL experiments. However, in real synthesized structures, these radiative recombination pathways are not the only means for carrier decay from these states. In particular, nonradiative loss to trap states exists, as well as the loss of carriers through migration to other regions in the structure. Therefore, the decay profile generated from a TRPL measurement often contains more than one exponential component, and is frequently fit to a bi-exponential function, giving two decay lifetimes. It is hypothesized that each of these exponential components coordinates to a different mechanism of carrier decay. In the structures under study, the primary mechanisms by which the population of carriers in either of the quantum dots might decay are by radiative recombination, nonradiative recombination (via trap states), and carrier transfer to another location within the nanostructure. While TRPL cannot distinguish between these mechanisms, physical reasoning can help ascribe meaning to them. In CdSe(Te)/CdS/CdSe structure in particular, it is believed that nonradiative loss to trap states produces the short lifetime exponential decay, while radiative recombination leads to the longer lifetime decay.

As described above, the focus of TRPL experiments is quite different than that of steady-state PL experiments. So too is the measurement methodology. In particular, TRPL experiments require the use of pulsed lasers which deliver light in very short pulses, typically orders of magnitude smaller than the decay lifetimes of a transition,

at high repetition rates to allow for many excitation events over an integration time window. The TRPL data is collected via Time-Correlated Single Photon Counting (TCSPC), where photons are transformed to electrical signal by an Avalanche Photodiode (APD) rather than a CCD. The principles of TCSPC and APDs are explored in below.

3.3.1.1 Time-Correlated Single Photon Counting

TRPL spectroscopy requires time resolution often down to picoseconds. This time resolution is very difficult to achieve, especially if trying to differentiate between the emission time of photons from a single excitation event. Rather than try to record multiple photons from a single excitation event, TCSPC records at most a single photon from each excitation event. With this method, time resolution on the picosecond, or even femtosecond, level is possible.

The principles of operation for TCSPC greatly resemble that of a stopwatch. It begins when a pulsed laser emits a pulse of light. At the same time, the laser triggers a fast photodiode, starting the stopwatch. The pulse then excites the sample, and photons are emitted following the transient decay profile for the studied transition. The emitted PL is directed towards an especially sensitive detector, the APD. The APD is a photovoltaic device made out of a semiconductor, such as silicon. Because of a very high reverse bias voltage, a single excited electron or hole has enough kinetic energy to create more mobile carriers by collision. This results in a growing 'avalanche' of current, which, from a single photon absorption event, produces an electrical signal sufficient to be read.

At the moment the first photon arrives at the APD, this electrical signal is sent to the computer to stop the timing mechanism, and the time between the excitation pulse and the arrival of the photon at the detector is recorded. Because the pulsed laser typically has a repetition rate on the order of 1 MHz, millions of these measurements are taken in only seconds. A histogram of the ensemble of measurements gives the

decay profile for the studied transition. The operating principle behind TCSPC is concisely demonstrated in Figure 15.

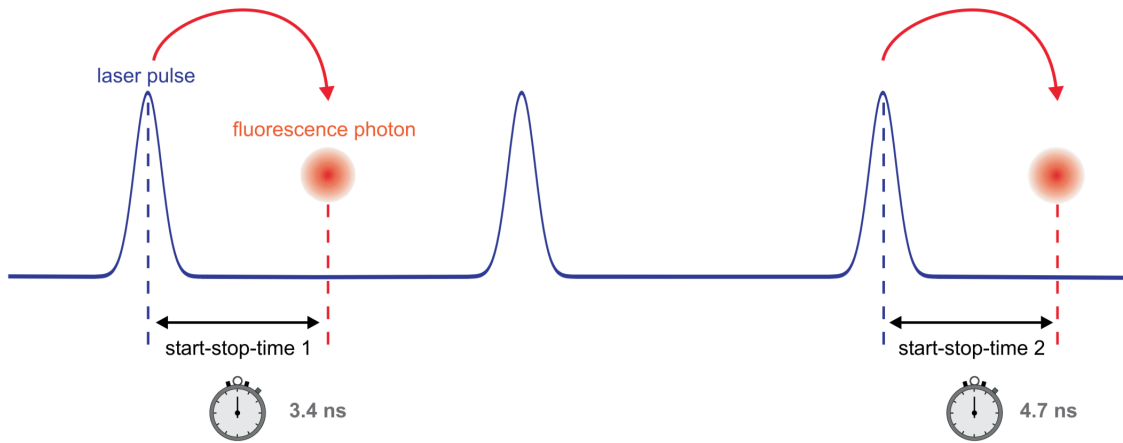


Figure 15: Operating principle for TCSPC. The laser pulse signals the timing mechanism to begin, and the arrival of a photon at the detector signals timing to stop. Because the arrival times of photons is random, forming a histogram from multiple measurements will give the decay profile for a radiative transition [31].

The randomness of the arrival times of photons is a critical assumption in TCSPC. It only holds, however, if at most one photon arrives at the detector per excitation event. If more than one photon, on average, arrives at the detector per excitation event, only the first photon would be registered, after which the detector experiences a 'dead time' during which no photon events are read. This would bias the decay profile towards the fast-arriving photons, decreasing the apparent decay lifetime. Therefore, in order for TCSPC measurements to accurately reflect the true decay dynamics, the laser signal must be attenuated such that the probability of multiple photons arriving per excitation event is low [31].

Another important aspect of TCSPC to note is that the 'stop' signal generated by the APD only depends on the arrival of a photon, without regard to the wavelength of the photon that arrives. TCSPC, therefore, is a wavelength-independent measurement scheme. However, if the APD is paired with a spectrometer that contains a diffraction grating (see 3.1.1.1) and a narrow exit slit, then only a chosen wavelength of light will reach the APD for detection. Therefore, different TRPL measurements

can be taken at different wavelengths from a samples PL spectrum. Pairing these measurements can give a 3D TRPL profile, which shows the emitted photon intensity as a function of both the time after excitation (the x-axis) and the wavelength (the y-axis). A vertical cross-section of this plot gives the PL spectrum for a sample, and a horizontal cross-section gives a single TRPL decay profile.

3.3.2 Methods

Although TRPL is quite different from steady-state PL, the experimental setup is similar. A Fianium WhiteLase laser connected to an acousto-optical tunable filter was used as the pulsed laser source. The Fianium repetition rate was set at 0.5 MHz, giving enough time between pulses for the decay profile of photoluminescence to effectively reach zero. The filter allowed the emitted wavelength of the white laser to be controlled. The pulsed laser source was directed through a series of mirrors and alignment irises to the free-space sample stage, which could similarly be adjusted in the x-direction to maximize PL collection. The PL signal was again collimated by an objective and directed to the spectrometer. The diffraction grating in the spectrometer was used to control the wavelength of PL that left the spectrometer through a narrow exit slit. After exiting the spectrometer, photons traveled to the APD for collection. Both the APD and the Fianium WhiteLase were electrically connected to a PicoHarp TCSPC module, which acted as the 'stopwatch' and transmitted the data points to a computer for readout. [Figure 16](#) provides a schematic of the experimental setup for TRPL measurements.

After the PicoHarp software had recorded a decay profile at the selected wavelength for a selected integration time, the data was transferred to FluoFit, a software which allowed for multi-exponential fits of this data. The software performed a Chi-square goodness of fit test to determine if the data was under or overfit, and it was concluded that two exponential components generally gave the optimal Chi-squared value of 1. Bi-exponential fits were generated in FluoFit for each TRPL measurement, and the lifetimes with corresponding amplitudes were recorded. To generate 3D TRPL

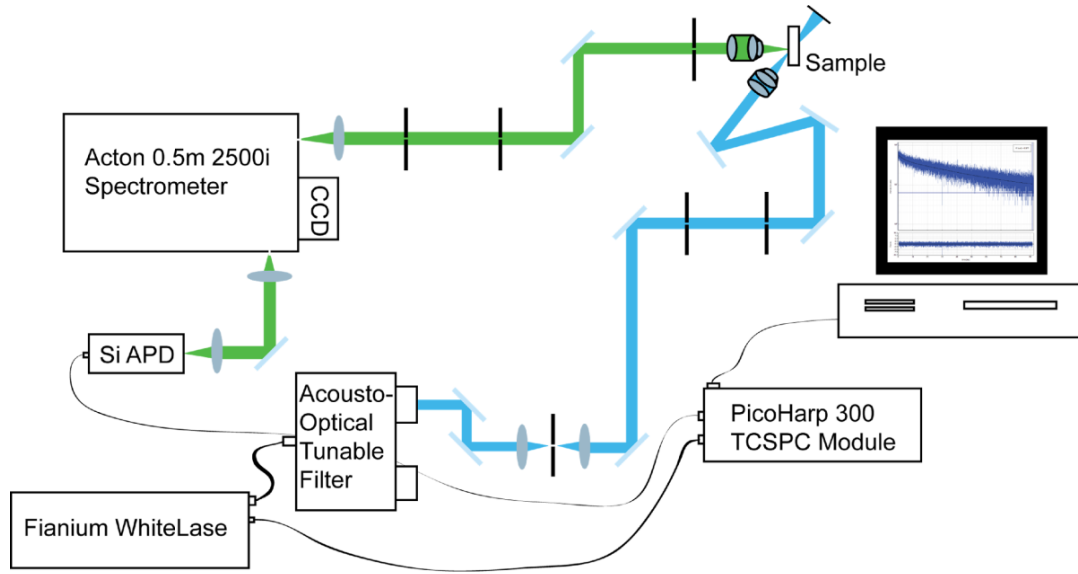


Figure 16: The experimental setup for TRPL measurements. The path of the exciting laser is shown in blue, the path of PL is shown in green, and electrical wiring is shown by curved black lines. The computer demonstrates the form of a TRPL decay curve.

profiles, the detection wavelength in the TRPL setup was adjusted via the diffraction grating, and TRPL measurements were taken at wavelengths spanning the PL spectrum for a sample. These data were then compiled in OriginLab, which generated the 3D plot.

3.3.3 Results

To provide a comprehensive analysis of the carrier dynamics for radiative transitions within the upconverting structures, TRPL measurements were taken at various wavelengths across the PL spectrum for the samples, at increments of 5-25nm depending on the proximity to a PL peak. These TRPL measurements were taken with a 475nm pulsed laser operating at a 0.5MHz repetition rate. The power of the laser was attenuated such that at most one photon reaches the APD detector per pulse, preventing any adverse dead time effects. The individual TRPL measurements were plotted together as a function of both time and wavelength to give a 2D TRPL scan. The resulting scans for each sample are shown in [Figures 17 - 20](#).

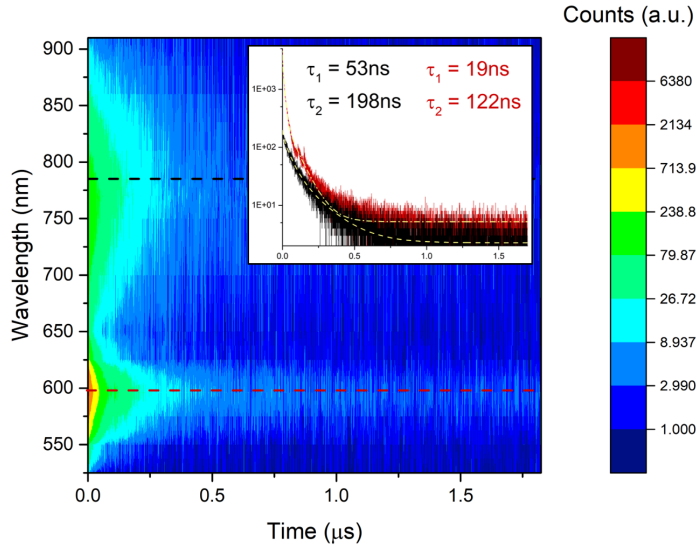


Figure 17: The 2D TRPL profile for the 4% Te-doped sample. The inset shows two TRPL measurements at constant wavelength correlating to the emitter (596nm) and absorber (770nm) peaks, with the primary extracted lifetime for each state noted.

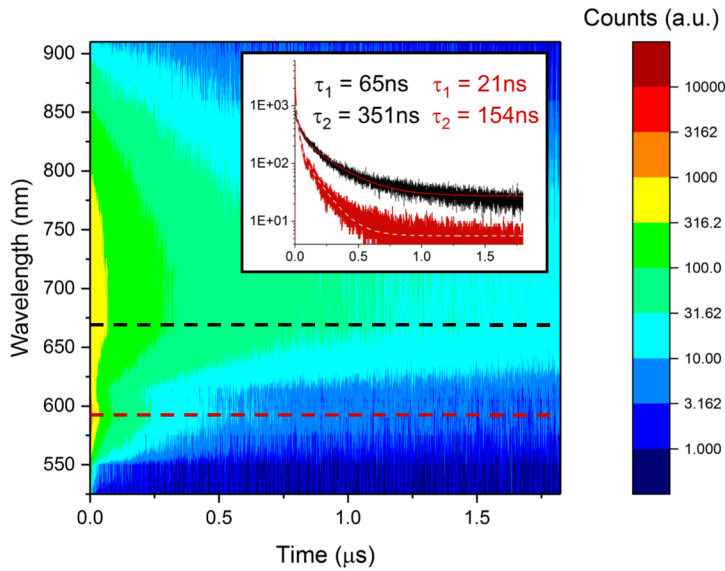


Figure 18: The 2D TRPL profile for the 10% Te-doped sample. The inset shows two TRPL measurements at constant wavelength correlating to the emitter (590nm) and absorber (660nm) peaks, with the primary extracted lifetime for each state noted.

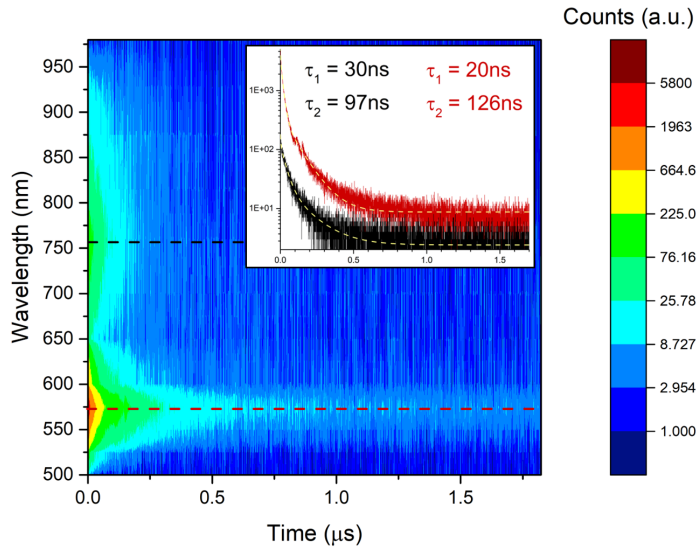


Figure 19: The 2D TRPL profile for the 20% Te-doped sample. The inset shows two TRPL measurements at constant wavelength correlating to the emitter (575nm) and absorber (760nm) peaks, with the primary extracted lifetime for each state noted.

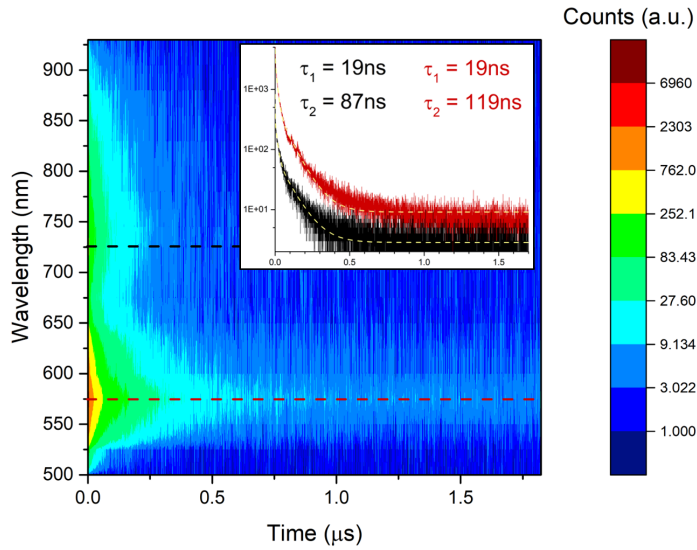


Figure 20: The 2D TRPL profile for the 40% Te-doped sample. The inset shows two TRPL measurements at constant wavelength correlating to the emitter (575nm) and absorber (725nm) peaks, with the primary extracted lifetime for each state noted.

3.3.4 Analysis

As expected from the PL spectra, each 2D TRPL spectrum contains two peaks - one for the emitter, one for the absorber - each of which decay exponentially. It is also evident from these figures that the decay rate for each peak within a single structure is not necessarily the same. To quantify the lifetimes associated with a single peak, a single decay profile at the peak maximum was fit to a bi-exponential function as described above. The resulting decay lifetimes are summarized in [Table 3](#).

As has been previously discussed, these lifetimes provide critical information that can be fed into a computational kinetic model of the upconverters. By themselves, however, the lifetime data still provide valuable insight to changes in carrier dynamics between the samples. In the emitter quantum dot, both lifetime components remain relatively constant between samples. This supports the notion that the emitter quantum dot dimensions and compositions do not vary significantly between the samples, as is desired. The lifetime components of the absorber quantum dot, however, do vary widely between samples. In particular, the long, radiative lifetime in the 20% and 40% samples is half of that of the 4% sample, while for the 10% sample is twice that of the 4%. Although it is difficult to say what trend is expected for the decay lifetimes with varying Te-doping, the lack of a clear trend and wide variations in the data again indicate the presence of unexpected effects in the structures, likely due to variations in synthetic parameters other than the Te-doping. Therefore, it is not possible to precisely isolate the true effect of Te-doping on radiative decay lifetimes.

Table 3: Exponential decay lifetimes obtain from TRPL fits.

Sample	Absorber		Emitter	
	τ_1 (ns)	τ_2 (ns)	τ_1 (ns)	τ_2 (ns)
4% Te	53	198	19	122
10% Te	65	351	21	154
20% Te	30	97	20	126
40% Te	19	87	19	119

While the data do not provide clear insight to the effect of Te-doping on carrier dynamics, they do give some early indications as to what structures might upconvert most efficiently. Recalling the sequence of steps involved in the upconversion process and the kinetic model presented in 2.4, it is clear that successful upconversion relies on singly-excited holes remaining within the absorber quantum dot for a long enough time to be excited by another absorption event. Therefore faster radiative decay, and thus shorter radiative decay lifetimes, should inhibit the upconversion process, with all else equal. By applying this reasoning to the data in Table 3, the 20% and 40% Te-doped samples are expected to have the lowest upconversion efficiency, while the 10% should have the highest efficiency, based on lifetime analysis alone. However, this reasoning ignores a number of other factors which impact the upconversion efficiency of a structure, so cannot alone definitively predict trends in upconversion quantum yield. Still, this insight is important in examining the potential limitations on efficient upconversion in these structures. The following section continues this examination of upconversion efficiency via measurements of quantum yield (QY) and upconversion quantum yield (UCQY).

3.4 Quantum Yield

Simple steady-state PL measurements as discussed in 3.1 can provide powerful insight into the performance of upconverting structures. A slightly more complex series of those measurements with varying excitation intensity, as discussed in 3.2, can reveal the nature of the upconversion mechanism within these structures. However, these methods alone give no information about the efficiency of the photoluminescence processes within these structures, most importantly the upconversion process. These *quantum yield* (QY) measurements, including *upconversion quantum yield* (UCQY), are the focus of this section.

3.4.1 Motivation and Background

For upconverting structures, two of the three performance metrics, AB and PES, can be determined or roughly estimated from PL measurements, simple absorption measurements, or knowledge of the bulk band gaps of the component materials. The third performance metric, UCQY, can be predicted using kinetic data, some of which is determined using TRPL measurements; however, precisely quantifying the true UCQY of an upconverting structure requires carefully calibrated measurements. These measurements can either generate QY or UCQY data, based on the wavelength of the excitation source. Determining the QY of upconverting structures with above band gap excitation can indicate limitations on the upconverter performance due to the efficiency of recombination alone. Measured UCQY values then indicate the efficiency of the upconversion mechanism in the structure, critical for assessing its performance for solar applications. Further, the experimentally determined UCQY value can be compared to the predicted yield given by a computational model. Combined with experimental determination of the PES and AB, this comparison can determine whether the synthesized structures are not performing as the model predicts. This can either indicate a flawed synthetic procedure that produced imperfect structures, or that assumptions within the model are flawed and predict an incorrect UCQY. If the measured UCQY does agree with the model prediction, the model can then be used to adjust the design and synthesis to produce more efficient upconverters. By taking subsequent UCQY measurements, the trends predicted by the model can be experimentally verified. Therefore, UCQY measurements are critical both for assessing the performance of an upconverting structure and for checking the validity of the computational model.

Measurement of UCQY in general requires much more than a single UCPL spectrum. Rather, absorption measurements, UCPL measurements, PL measurements of a quantum yield standard, and knowledge of the incident laser power are all needed to determine the UCQY of a structure. Because precise measurement-to-measurement standardization is necessary for comparison to a quantum yield standard, the UCPL and PL measurements are taken in an integrating sphere [32], the principles of which

are discussed below. The appropriate ratios of the PL/UCPL and absorbance at the excitation wavelength in both the sample and the standard give the ratio of their quantum yields, from which the sample UCPL can be calculated. Accurate and precise QY and UCQY measurements require the careful implementation of an integrating sphere-based setup, choice of an appropriate quantum yield standard, and detailed calculation procedure. These features of QY measurements are discussed below.

3.4.1.1 Integrating Sphere

The integrating sphere used in this experiment was purchased from Labsphere. The 6-inch diameter sphere was equipped with 3 entrance/exit ports. The first 1-inch entrance port was equatorial on the sphere, and the size of the entrance was attenuated using an attachment. The laser was directed through this port into the sphere. The second 1-inch port was situated on the north pole of the sphere. Colloidal samples of the upconverting structures were lowered into the sphere through this port via a custom 3D-printed sample holder. The final 2.5-inch exit port was situated 90 from the entrance port; the signal was directed through this port to the spectrometer via a fiber bundle held by a custom 3D-printed fiber mount.

What makes the integrating sphere a salient tool for measuring QY is that, isotropically emitted light emitted by samples within the sphere can only exit from either the small entrance port or through the fiber mounted in the exit port. Therefore, the fraction of emitted light that exits through the fiber and ultimately is recorded by the spectrometer is constant from sample to sample, allowing for calibration of the sphere with a QY standard, and providing the consistency between measurements necessary for confidence in the QY measurements.

This consistency, however, is not the only feature of the integrating sphere that allows for precise QY measurements. Because the area of the fiber bundle available for coupling to light inside the sphere is a minute fraction of the total solid angle in the sphere, direct collection of emitter light would result in minimal signal. To increase the photon flux on this fiber, therefore increasing the signal, the inside of the sphere is

coated with a diffuse reflective material, called Spectralon, that diffusely reflects light with nearly uniform efficiency above 97.5% from 350-1600nm [33]. The 3D-printed pieces that attach or enter the sphere were similarly coated with barium sulfate paint, which displays diffuse reflectance values near 99% in the same range [34]. This reflective coating allows light to remain in the sphere until it exits through either the fiber or the entrance port. Therefore, the fiber collects more indirect light that has been reflected multiple times than light that comes directly from the sample, magnifying the signal. To further improve the measurement-to-measurement consistency, a barium sulfate coated baffle is placed in the sphere 1 inch from the fiber exit port, blocking all emitted light from directly entering the fiber bundle. Thus, all light collected has been reflected by the sphere multiple times. This indirect collection allows the collection efficiency of the sphere to be completely independent from the exact placement and orientation of the sample within the sphere, so that small deviations in placement do not result in systematic error in QY measurements.

3.4.1.2 Quantum Yield Standard: Rhodamine 101

Determination of quantum yield of samples by comparison to the PL signal of another substance requires that the substance itself have a very well-defined and consistent quantum yield. For the most accurate measurements, it is also important that the quantum yield standard emit light in approximately the same region of the electromagnetic spectrum as the samples under study. This ensures that any wavelength dependencies in the collection efficiency of the measurement system do not systematically affect the quantum yield calculation.

In the core-rod upconverters studied in this paper, the emission peaks of the absorber quantum dot generally center around 800nm. The emitter peak centered near 600nm, however, is of more interest in upconversion quantum yield measurements, as it indicates the yield of the two-photon upconversion process. Rhodamine 101 was therefore chosen as the quantum yield standard for these experiments on the basis of its emission at roughly 600nm. Rhodamine 101 is a fluorescent dye that, when dissolved

in methanol and excited with a 535nm laser, luminesces with a quantum yield of 1.00 ± 0.05 [35], and has been reported to retain this value for excitation wavelengths in the 500-550nm range [36]. The structure of and PL spectrum of Rhodamine 101 are shown in Figure 21. The 100% quantum yield of Rhodamine 101 corresponds to the integrated peak counts across this spectrum.

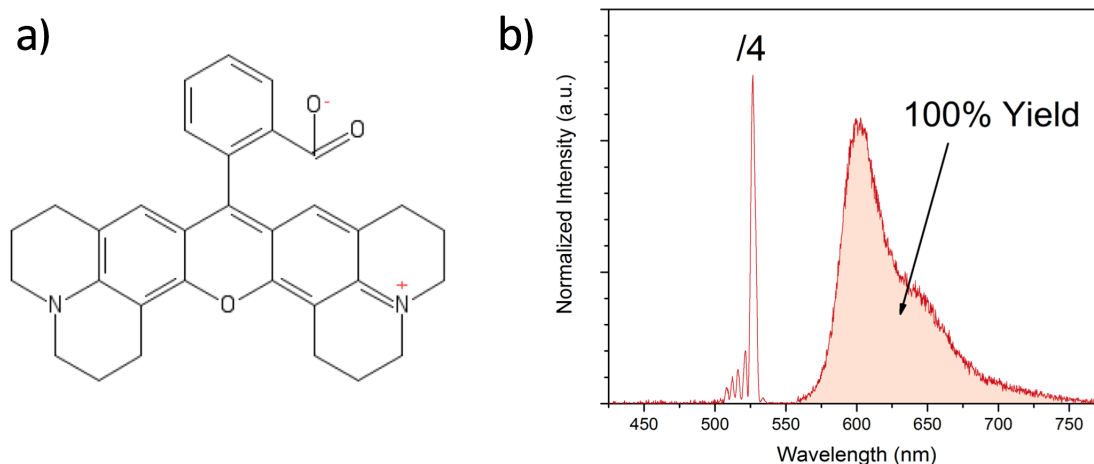


Figure 21: (a) The chemical structure of Rhodamine 101. (b) The PL spectrum of Rhodamine 101 excited with 532nm laser, showing the peak integration equating to 100% quantum yield.

3.4.1.3 Calculating Quantum Yield

The equations and procedure for calculating QY and UCQY from the appropriate measurements can be straightforwardly inferred from the definition of quantum yield, and are adapted from [36] and [37]. As was indicated in 2.2.2, the quantum yield of a substance is defined as the ratio of emitted photons to absorbed photons. Since quantum yield measurements are taken under continuous excitation, this definition can be amended to the ratio of the rate of emitted photons to the rate of absorbed photons. The rate of absorbed photons can be straightforwardly calculated by multiplying the incident photon flux, $q_{p,exc}$, by the absorption factor of the sample at the excitation wavelength, $f(\lambda_{exc})$. The incident photon flux can be calculated from the measured incident laser power (P_{exc}) as in Equation 2.

$$q_{p,exc} = \frac{P_{exc}\lambda_{exc}}{hc} \quad (2)$$

In principle, the rate of emitted photons for a system with perfect collection efficiency could be taken as the integrated peak counts of the PL or UCPL spectrum divided by the measurement integration time. However, in real systems the collection efficiency is not perfect, and the integrated peak counts are only a fraction of the emitted photon counts. Calculation of the quantum yield therefore requires knowledge of this fraction, called the collection efficiency of the setup, symbolized as η . Once the collection efficiency is known, the quantum yield of the sample, indicated by a superscript of i , can be calculated as in [Equation 3](#) (the symbol Φ_f is used to indicate fluorescence quantum yield).

$$\Phi_f^i = \frac{F^i}{\eta f(\lambda_{exc}^i) q_{p,exc}^i} \quad (3)$$

In this equation, F^i indicates the integrated PL count rate, which is described by [Equation 4](#).

$$F^i = \frac{1}{\tau^i} \int_i q_f^i(\lambda_{em}^i) d\lambda_{em}^i \quad (4)$$

Where τ^i indicates the integration time for the sample, and $q_f^i(\lambda_{em}^i)$ indicates the PL or UCPL counts as a function of emission wavelength. The integral is taken over the relevant PL or UCPL wavelength range.

If all measurements are taken in a properly implemented integrating sphere, the collection efficiency of the setup will remain constant from one sample to another as long as the measurements are taken over similar wavelength ranges. In this case, the PL counts of the quantum yield standard can be used to deduce the collection efficiency. By applying [Equation 3](#) to the standard (indicated by the superscript s) and rearranging the collection efficiency can be written as in [Equation 5](#).

$$\eta = \frac{F^s}{\Phi_f^s f(\lambda_{exc}^s) q_{p,exc}^s} \quad (5)$$

Where F^s can be calculated exactly as in Equation 4, replacing the sample integration time with the standard integration time, and integrating the standard PL over the appropriate wavelength range. Combining Equation 5 with Equation 3 thus provides the tools for calculating the standard quantum yield, given that the collection efficiency is invariant for the standard and sample measurements. While this assumption is generally fairly accurate, it does result in minor errors if the standard and sample are dissolved in different solvents with different refractive indices. To account for different solvents for the sample and standard, the collection efficiency is multiplied by the ratio of the squares of their refractive indices. Therefore, combining Equation 5 with Equation 3 and accounting for the refractive index factor gives the final equation for calculating a sample's QY, given by Equation 6.

$$\Phi_f^i = \frac{F^i f(\lambda_{exc}^s) q_{p,exc}^s n_i^2}{F^s f(\lambda_{exc}^i) q_{p,exc}^i n_s^2} \Phi_f^s \quad (6)$$

In this equation, n represents the refractive index of the solvent for either the sample or standard. For the upconversion process, however, the maximum achievable UCQY by Equation 6 is 50%, as only one photon is emitted per two absorbed. To measure UCQY on the more natural scale, where 100% represents a perfectly efficient upconverter, this equation is multiplied by 2. The equation used for calculating UCQY, represented by Φ_{UC}^i , is given by Equation 7.

$$\Phi_{UC}^i = 2 \frac{F^i f(\lambda_{exc}^s) q_{p,exc}^s n_i^2}{F^s f(\lambda_{exc}^i) q_{p,exc}^i n_s^2} \Phi_f^s \quad (7)$$

3.4.2 Methods

The quantum yield measurement setup shares many features with the standard steady-state PL setup. The same laser sources available for steady-state PL are available for quantum yield measurements. In particular, a 405nm CW laser diode, a 532 CW laser diode, and the near-IR tunable Ti:Sapph laser, often used at wavelengths near 750nm, are available for QY and UCQY measurements, which can be filtered pre-excitation by ND or LP filters. The desired excitation source is redirected towards the

integrating sphere by a flip mirror followed by a series of mirrors and alignment irises. The excitation beam is then focused to a point in the center of the integrating sphere by a plano-convex lens. Either the standard or the sample under study is contained in a 5-mL glass cuvette, which is held in the integrating sphere by a 3D printed sample holder. This holder also covers the north exit port of the sphere, and is coated with diffusely reflective barium sulfate paint. The laser excites the sample inside of the sphere, and photoluminescence reflects around the sphere until it either exits through the attenuated entrance port or via a round-to-round fiber bundle. The fiber bundle is held at the 90 exit port by a 3D printed fiber mount and baffle, which prevents emitted photons from directly entering the fiber bundle. Light is then directed through the fiber bundle to an in-line filter mount, allowing for post-excitation filtration of the PL or UCPL signal by ND or SP/LP filters to reduce the total signal or the laser signal. The filter mount then couples to a round-to-linear fiber bundle. The round end is attached to the filter mount to allow for minimal insertion loss, and the linear end directs into the spectrometer. The linear end of the fiber is held by an xyx-stage and a precision rotation mount, allowing the fiber to be precisely aligned to the narrow spectrometer entrance slit. Once light is inside the spectrometer, it is diffracted and measured just as in the standard steady-state PL measurements discussed in 3.1. A schematic of the quantum yield setup is shown in [Figure 22](#).

To take QY and UCQY measurements, the absorbance spectra of the Rhodamine 101 standard and the sample are both taken in an Ocean Optics USB Spectrometer to determine the absorption factors at the excitation wavelengths. The Rhodamine 101 cuvette is then placed in the integrating sphere and excited with 532nm laser according to its specified excitation range for 100% QY. The laser power is measured just before entrance to the integrating sphere, and the PL spectrum is recorded. The dark counts are then recorded by taking a PL measurement with the same integration time when the laser is blocked or powered off. The Rhodamine 101 cuvette is replaced with the sample cuvette, and the appropriate laser source is chosen. The laser power is again measured just before entrance to the sphere, and the PL or UCPL spectrum

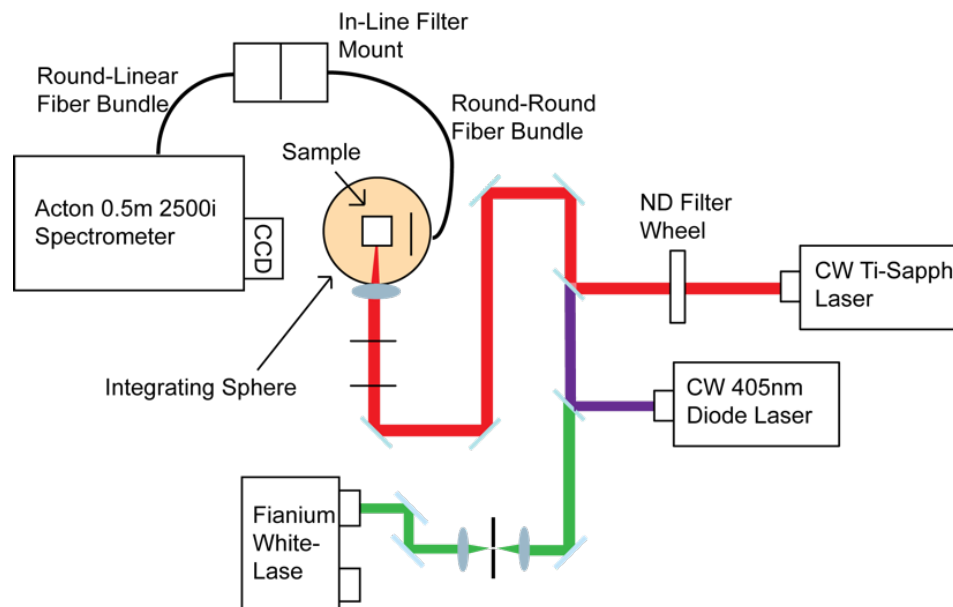


Figure 22: The experimental setup for measuring QY and UCQY. The multiple excitation sources are shown in green, red, and purple, and the fiber bundles are shown by curves black lines.

is recorded, as well as a corresponding dark counts spectrum. The Rhodamine 101 and sample spectra are then zeroed by subtracting the respective dark count spectra. Once all data is recorded, the zeroed spectra, laser powers, laser wavelengths, and absorption coefficients are fed into a MATLAB code which carries out the integration of the PL/UCPL spectra and calculates the sample QY or UCQY. In the case of UCQY measurements, depending on the nature and shape of the UCPL spectrum, the MATLAB code carries out further data processing to produce an accurate UCQY value. The details of the MATLAB code and the data processing techniques are discussed the forthcoming sections and Appendix A.

3.4.3 Results

Using the procedure described above, standardized UCPL spectra were obtain using the integrating sphere for all four samples. These spectra were zeroed using a 'dark counts' spectrum, and were integrated over appropriate bounds to obtain the UCQY of the emitter peak only. These spectra and this integration are shown in [Figure](#)

23.

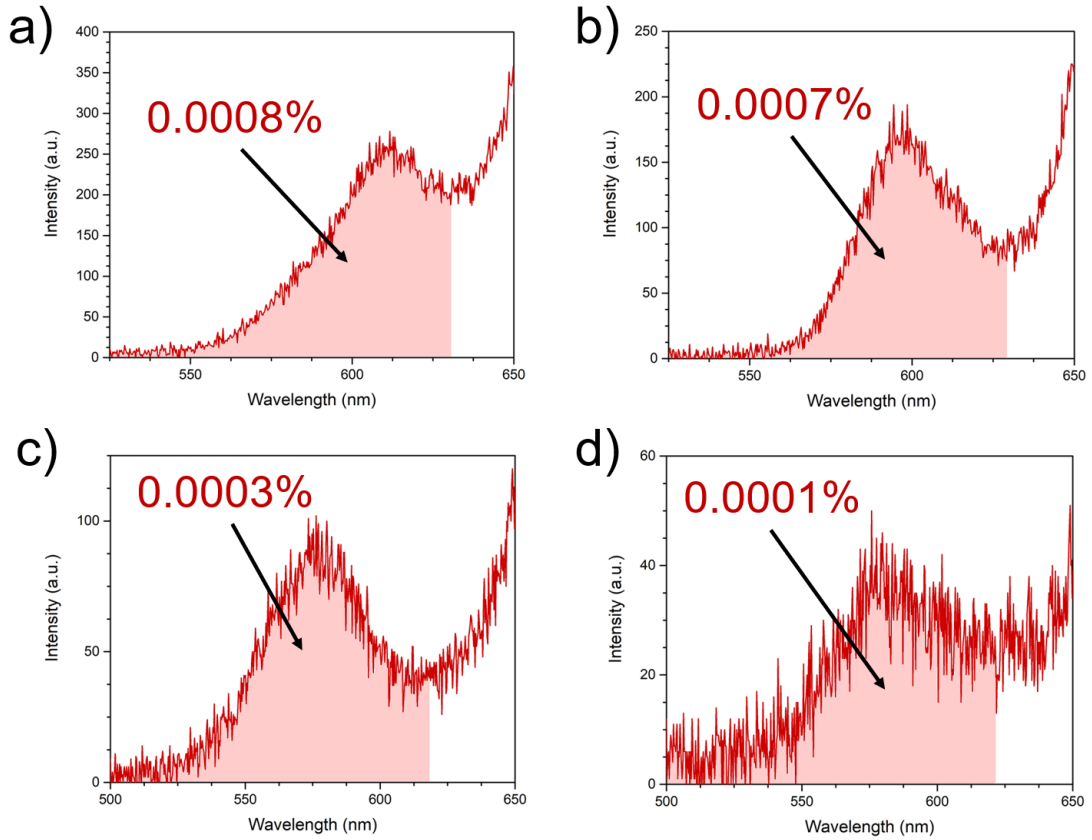


Figure 23: UCPL spectra for (a) the 4% Te-doped sample, (b) the 10% Te-doped sample, (c) the 20% Te-doped sample, and (d) the 40% Te-doped sample. The areas shaded in red show the integrated area used to determine the noted UCQY values.

The upper limit of integration for each spectrum was set at the local minimum for the spectrum between the emitter peak and the lower-energy tail. Because the UCQY value should represent the desired upconversion that emits from the emitter quantum dot, this decision aimed to maximize the inclusion of counts from the emitter peak while minimizing unwanted counts from the low-energy tail, coordinating to thermal upconversion within the absorber dots. To quantify the error in the UCQY measurements, the measurements were repeated in full on separate days. Additionally, standard QY measurements for the emitter peak were taken using above band-gap excitation (with the 412nm diode laser). The results of all UCQY and QY experiments

are summarized in [Table 4](#).

Table 4: Summary of QY and UCQY measurements for the emitter peak in each structure.

Sample	QY (%)	UCQY ($\cdot 10^4$ %)
4% Te	0.25	7 ± 2
10% Te	0.14	4 ± 4
20% Te	0.44	3 ± 1
40% Te	0.21	1.1 ± 0.5

3.4.4 Analysis

From [Table 4](#) and [Figure 23](#), it is immediately evident that the UCQY values reported here are quite low; in fact, they are substantially lower than previously reported values for other classes of upconverters and other materials system, as well as orders of magnitude lower than predicted UCQY values from the kinetic model. The values are also orders of magnitude lower than the 0.1% UCQY value reported in [\[25\]](#) for the same structure and material system. However, this 0.1% figure represents the upconversion efficiency for "hot holes", or already existing doubly-excited excitons, while the values reported here are normalized only by the absorbance of the structure, and therefore more rigorously fit the definition of UCQY. Because the yield of "hot holes" from absorption events is unknown, it is difficult to directly compare the UCQY values reported here to the 0.1% value reported in [\[25\]](#). Regardless, the UCQY values of these structures are much lower than is desired for creating a noticeable impact on solar technologies.

Because a major goal of this paper is to study the viability of heterostructure engineering via adjusting the Te content of the absorber quantum dot, it is critical to examine the difference in UCQY with varying Te-doping. From [Table 4](#), it appears that there is a general decrease in UCQY with increasing Te-doping. However, there are two major issues with extrapolating a trend from these data: a large relative error in UCQY (particularly for the 10% Te-doped sample), and the potential for systematic

error in choosing the upper bound for the UCQY integral. As for the first issue, the error bars for the 4%, 20% and 40% samples do not overlap, and therefore these samples support an inverse trend in UCQY and Te-doping. Although the mean value for the UCQY for the 10% sample falls in line with this trend, this sample displays a relative error approximately equal to the mean value. Thus its error bars encompass virtually the entire range of UCQY values seen in this study, casting doubt on any trends drawn from the remaining data.

While the high relative error most significantly affects the UCQY value of the 10% sample, the issue of systematic error from the integration bounds affects all samples. Because the shapes of the emitter peak and tail in each UCPL spectrum are different, applying a rather arbitrary integration bound could lead to a false trend in the data. Therefore, to draw any useful conclusions from the UCQY values requires remedying this systematic error. To do so, the UCPL spectra must be successfully deconvolved into two separate peaks - the full emitter peak, and the absorber peak corresponding to the low-energy tail of the each spectrum.

With the data at hand, there are two possible methods for carrying out such a deconvolution. The first would be to perform fits - assuming some functional form or forms for the peaks - on the full PL spectra for each sample over both the emitter and absorber peak, and scale the respective peak fits to properly match the UCPL data from the integrating sphere. The second method would be to perform similar fits, still assuming functional forms for each peak, but on the UCPL data from the integrating sphere directly. Either method would generate independent equations describing the emitter and absorber peak, and integration of the former would lead to the quantum yield of the emitter peak only. The benefit of the first fitting method is that a fit to the complete PL spectrum would likely generate a more accurate fit for the absorber peak, which is mostly cut off in the UCPL spectra. However, this method assumes that the shape of the emitter and absorber peaks does not change based on the excitation conditions, and therefore is the same in both the PL and integrating sphere UCPL spectra. Because the excitation wavelength in the UCPL spectra actually falls

within the absorber peak, this assumption is likely invalid. By examination of the UCPL spectra in [Figure 23](#), it is also evident that the relative intensities of the emitter peak and the absorber tail has drastically changed compared to [Figure 11](#), further disproving the validity of this assumption. Additionally, due to the asymmetric shape of the absorber peaks in the PL spectra, accurate fits would require assumption of an unconventional functional form rather than the traditional Gaussian peak shape for an ensemble of quantum dots. While a fit to the UCPL spectra only would have a smaller data set over which to fit, it would not require making such potentially invalid and unphysical assumptions. It would also guarantee that the resulting fit would be the best fit possible for the UCPL spectra. Therefore, while it is still imperfect, it is determined that this is the better method for carrying out the deconvolution with the data at hand.

To fit the UCPL spectra, each peak is assumed to have a Gaussian shape. Therefore, a two-Gaussian fit is performed on each spectra, with specific bounds on the center wavelengths of each Gaussian peak to ensure that both an emitter and absorber peak were generated. The emitter peak fit is constrained to have a center wavelength between 500 and 650nm, while the absorber peak center wavelength is constrained to have a center wavelength greater than 650nm. These constraints, while physically justifiable, are loose enough to not force the fit to pre-selected values. The fits generated for the UCPL spectra given in [Figure 23](#) are shown in [Figure 24](#).

By visual inspection only, it appears that the fitting method produces relatively accurate fits that match the data sets quite closely. Some slight systematic deviations from the data are observed, but these deviations are only slightly outside the noise of the data. As a general quantitative gauge for the goodness-of-fit, the R^2 values too show that the fits agree quite well with the data; the R^2 values are well above 0.9 for the first three fits, and suffers in the 40% sample mostly because of the low signal-to-noise ratio in that data set. Given the apparent validity of the fits, it appears that this fitting method will produce more accurate UCQY data for the emitter peak. To determine the UCQY for each spectra, the Gaussian fit of the emitter peak can now

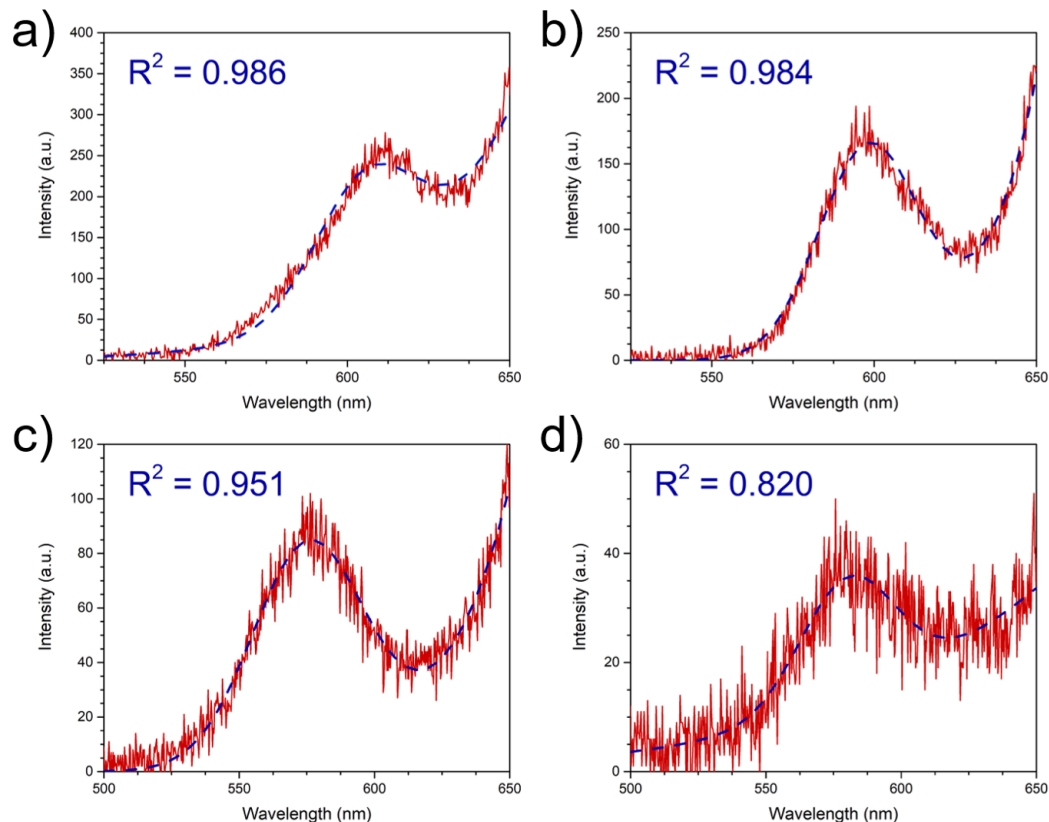


Figure 24: UCPL spectra taken in the integrating sphere with the corresponding two-Gaussian fits for (a) the 4% Te-doped sample, (b) the 10% Te-doped sample, (c) the 20% Te-doped sample, and (d) the 40% Te-doped sample. Raw data is shown in red, and fits are shown with blue dashes, with R^2 values shown.

be analytically integrated over all wavelengths. This integration is shown visually in [Figure 25](#). Using these UCQY values, the data in [Table 4](#) are updated and presented in [Table 5](#).

The UCQY data in this table are in general lower than those in [Table 4](#), without the deconvolution fits. While it was expected that deconvolving the peaks would reduce systematic error associated with manually choosing integration bounds, giving more accurate results, these fits have also reduced the relative error in most cases, increasing the precision of the UCQY measurements. This is likely due to the elimination of human error in choosing the integration bounds. However, the fits were unable to decrease the large uncertainty in the UCQY of the 10% sample, which appears to be

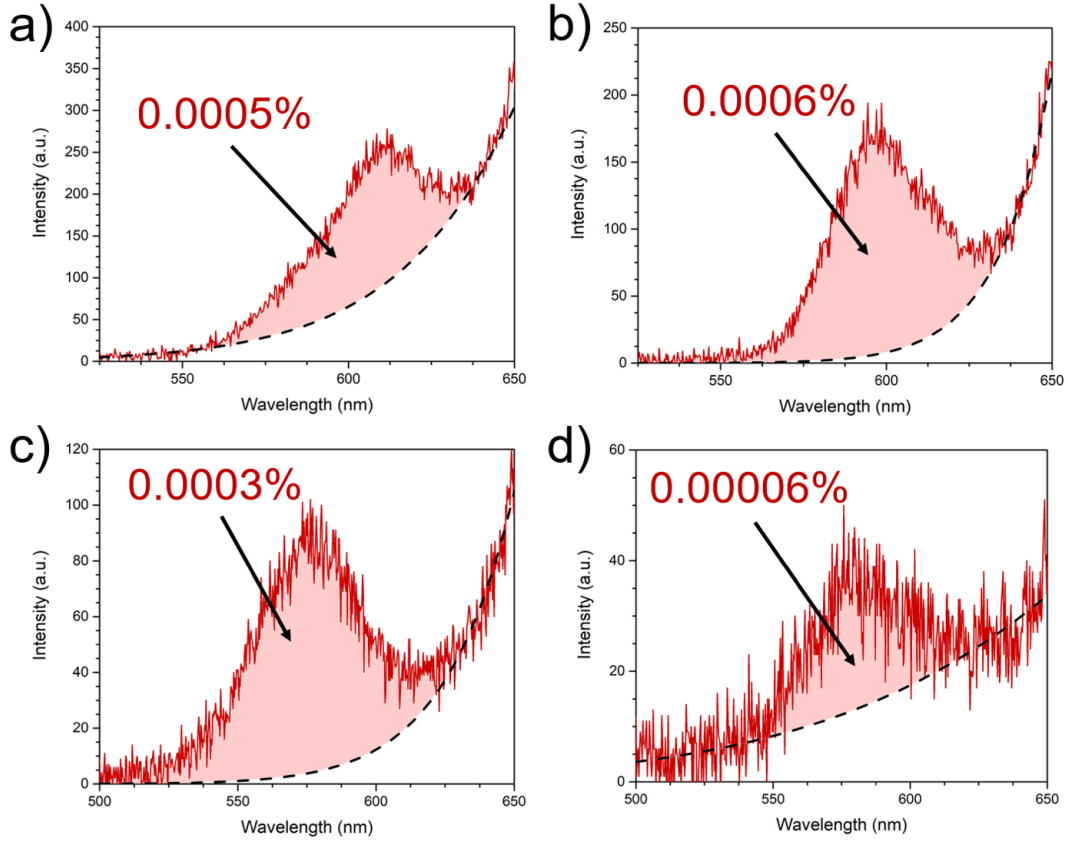


Figure 25: Deconvolved UCPL spectra for (a) the 4% Te-doped sample, (b) the 10% Te-doped sample, (c) the 20% Te-doped sample, and (d) the 40% Te-doped sample, using the fits shown in Figure 24. The UCPL is determined by integrating the emitter peak Gaussian fit (the red shaded region).

coming from a source other than the manual selection of the integration bounds. One possible source of this high uncertainty is sample degradation between measurements, giving a trend in UCQY values rather than variations around a mean. The UCQY for the 10% sample shown in Figure 25 is substantially higher than the mean value reported in Table 5. Therefore, subsequent measurements must have produced much lower values, consistent with sample degradation. However, other factors, such as variability in the measurement conditions, could have produced this high variability.

Altogether, it appears that there is still a slight downward trend in UCQY values with increasing Te-doping. Because of the large uncertainty for the 10% sample, it cannot be determined whether this sample fits the trend. For this trend to be a direct

Table 5: Summary of QY and UCQY measurements for the emitter peak in each structure, with UCQY values obtained via deconvolution of the emitter and absorber peaks.

Sample	QY (%)	UCQY ($\cdot 10^4$ %)
4% Te	0.25	5.3 ± 0.8
10% Te	0.14	4 ± 4
20% Te	0.44	2.5 ± 0.8
40% Te	0.21	0.58 ± 0.03

consequence of the Te-doping in the absorber dot, however, it is required that all other factors that affect UCQY must be equivalent in the systems. Given the irregularity and lack of trend in the shapes of the PL spectra shown in 3.1, and the varying relative peak heights of the absorber and emitter peaks in these PL spectra, it is very unlikely that all other factors have indeed been kept constant. Such undesired deviations can be clearly seen by examining the QY values for each sample. The QY values vary widely and without any pattern with respect to Te-doping. However, because Te-doping in the absorber does not effect the emitter dot, it should not effect the QY of the emitter when directly excited with high-energy light. Therefore, such variation indicates that other parameters might vary from sample-to-sample. Because the UCQY of the emitter dot is inherently limited by the QY of that dot, which approximately gives the efficiency of radiative recombination for excitons within the emitter dot, the variations in QY should also result in variations of the UCQY. Therefore, to determine the true effect of Te-doping on the UCQY, it must be isolated from the effects of changing emitter dot QY. To do this, the UCQY for each sample can be divided by the corresponding QY to normalize for unwanted effects that influence the efficiency of recombination. These UCQY/QY ratios (reported as percents) are shown in Figure 26.

The UCQY/QY ratio, as seen in this figure, is now highest on average for the 10% sample. However, due to the large error in the UCQY for this sample, the UCQY/QY ratio has a very large error, and is still impossible to place exactly within any trend. Outside of the 10% sample, the UCQY/QY ratio still appears to decrease

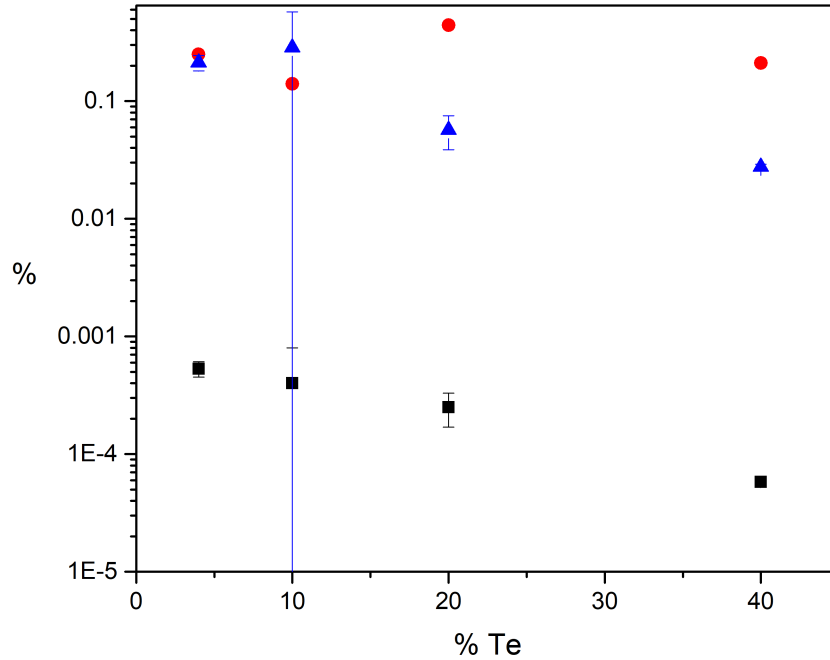


Figure 26: Values of the UCQY (black), QY (red) and UCQY/QY ratio (blue) for each sample, all reported in percents.

with increasing Te-doping. Because this ratio has now corrected for the undesired effect of varying emitter dot QY, it is believed that this trend is indicative of the effects of Te-doping. Therefore, these data indicate that increasing the Te-content of the absorber quantum dot decreases the UCQY of the upconverter.

Reexamining the PL spectra presented in 3.1 provides one possible reason why increased Te-doping might result in poorer UCQY. As was mentioned when initially examining the PL spectra, there is an increasing asymmetry in the absorber peak as the Te-content in the absorber increases. Because the synthetic methods used for these samples results in a compositional gradient within the absorber dot, such that the center of the dot is more rich in Te while the outer region is rich with Se, there are two regions of different, but close in energy, band gaps present within the absorber dot, resulting in two overlapping Gaussian peaks. This compositional inhomogeneity likely

results in the addition of trap states, both within the outer region of the absorber dot, and at the interface between the regions. Because the presence of these traps is a more severe issue as the regions become more well defined, which occurs with increasing Te-doping, the damaging effects of these traps on the UCQY should be more present in the highly doped samples. Therefore, increased Te-doping might damage UCQY by this mechanism.

3.5 Summary

At the beginning of this chapter, four goals were set forth to be accomplished by the characterization methods for each upconverting sample: (1) verify that upconversion occurs with emission from the emitter quantum dot; (2) determine if the mechanism upconversion is two-photon, one-photon, or some combination; (3) quantify the radiative decay lifetimes associated with emission from the emitter and absorber quantum dots; and (4) measure the upconversion quantum yield of each upconverting structure. By comparing the shapes of the UCPL and PL structures in 3.1, the presence of upconverted emission from the emitter dot was confirmed. In 3.2, similar UCPL measurements were taken at varying incident laser powers to measure the dependence of the upconversion intensity on the incident photon flux, in turn giving the order of the upconversion process. In all structures, this order was observed to have values between 1.1 and 1.5, indicating that the upconversion is neither a purely one or two-photon process, but rather some intermediate combination. Much of the one-photon character appears to come from a separate upconversion peak from the desired upconversion from the emitter dot - likely the result of phonon-mediated upconversion within the absorber quantum dot. The TRPL measurements in 3.3 demonstrated that the radiative decay trace for both the emitter and absorber quantum dots in all samples are best described by a bi-exponential function, indicating the presence of competing radiative and nonradiative recombination processes. These lifetimes can in turn be fed into the computational model to provide predictions of the UCQY for each structure. Finally the UCQY of each structure was measured in 3.4. The highest quantum yield

observed was still beneath one one-thousandth of a percent, indicating that more efficient structures must be synthesized if these upconverting nanoparticles are to have an effect on solar technologies.

A separate goal of this chapter was to compare the various measurements taken for samples with different Te-doping in the absorber quantum dot to determine if Te-doping is a viable method for engineering more efficient and high-performing upconverters. The primary means of making this comparison is to compare the UCQY of the different structures. In doing so, it was revealed that UCQY trends downward with increasing Te-doping. However, large uncertainty in the measurement of the 10% Te-doped sample makes it difficult to assess whether this trend is true for all levels of doping. Nonetheless, it still appears that structures with higher Te-content in the absorber dot have a lower quantum yield. This effect can be attributed to the creation of trap states due to the compositional inhomogeneity of the absorber quantum dot, which becomes more pronounced with increased Te-doping. Besides UCQY, the results of the PL/UCPL, power dependence, and TRPL measurements can also be compared between samples to assess other effects of Te-doping. The PL spectra revealed that the structures with lower Te-content produced more symmetric, nearly Gaussian absorber peaks, while higher Te-doping gave increasingly asymmetric absorber peak shapes. Again, this is likely attributable to compositional inhomogeneity in the quantum dot. The formation of a Te-rich center and an Se-rich outer 'shell' of the absorber dot might result in two distinct gaps over which carriers can recombine, producing an absorber peak that is really two overlapping Gaussian peaks.

In the power dependence and TRPL measurements, any trend with varying Te-doping is much less clear. The upconversion 'order' measured by the log-log slope of the UCPL integrated intensity vs. the excitation power was very similar for the 4%, 20%, and 40% samples, but was anomalously high for the 10% sample. Again in the TRPL measurements, the long lifetime component in the 10% sample was twice as high as that of the 4% sample, which itself was double the length of that of the 20% and 40% samples. These wide variations and lack of a clear trend indicate that other

factors besides just the Te-doping may differ between samples, and might be influencing the performance of the upconverters. Even in the PL spectra for each sample, wide variations in shape are present that cannot be explained by varying Te-doping only. Because the nature and effects of such variations in the structures are unknown, it is difficult to say whether the trend observed in UCQY truly results from Te-doping.

Considering the wide and unexplained variations in much of the data between different upconverting samples, varying the Te-doping of the absorber was not demonstrated in this paper to have successfully engineered more efficient upconverters. Because of unknown differences between the structures besides Te-doping, likely a result of synthetic variations, the true effects of Te-doping on critical performance metrics, particularly UCQY, could not be assessed with confidence. One possible reason why it was difficult to isolate the effects of the Te-content of the absorber is because of the compositional inhomogeneity of the absorber dot. In the computational model and initial analysis of this structure of upconverter, it was assumed that the absorber would be compositionally uniform, with a flat band edge. If adding additional Tellurium caused this uniformity to disappear, it would result in potentially undesired consequences, some of which were demonstrated in this paper. Therefore, this study highlights the importance of controlling the composition profile within the absorber dot in particular. If it is demonstrated, for instance, that this inhomogeneity is damaging to upconverter performance, then careful synthetic steps must be taken to ensure the absorber composition profile is uniform. Such work is the subject of the following chapter. Once these synthetic changes have been made, variations in Te-doping can again be studied to better assess the effects of this variable alone.

Chapter 4

FUTURE WORK

In the previous section, two major issues were exposed in the design and characterization methods of colloidal CdSe(Te)/CdS/CdSe upconverters. The first of these issues, the irregularity in the samples introduced by compositional inhomogeneity in the absorber dot, was observed immediately in the PL spectra and continually throughout the remainder of the section. Because this inhomogeneity potentially negated the desired effects of varying the Te-doping by creating two distinct regions within the absorber rather than a uniform region of varying band gap, it should be resolved, or at least further studied, so that the effect of other engineering changes can be isolated with more certainty. For example, although some trends, such as a general decrease in UCQY, were observed with increasing Te-doping, it is difficult to discern whether this effect is a result of the additional Tellurium causing changes in the band edge in the absorber, or due to the increasing inhomogeneity which might itself introduce carrier traps. Experiments studying the effect of compositional grading, in the absorber dot and in the CdS rod, are presented in [4.1](#).

The second issue observed in the previous chapter was the high degree of convolution of two separate features in the UCPL spectra - the desired upconversion from the emitter, and the undesired upconversion from the absorber. As was seen in the power dependence analysis, this convolution made it difficult to isolate the upconversion order of the desired process leading to emission from the emitter dot. This difficulty arose because integration over the observed upconversion peak would include counts from both the desired and undesired peaks. In the section on quantum yield measurements, the same issue was seen to an even greater extent. Because full integration over the

spectra would artificially inflate the UCQY of the desired process, and because arbitrarily choosing integration limits induced systematic error on the measurements, this issue was addressed by carrying out a two-Gaussian regression on the data. While this method did allow isolation of the emitter UC peak, it relied on assumptions which might be unjustified, and fits that might be unphysical, as well as introducing an element of fitting error that is difficult to quantify. To better understand the error in this fit, as well as limit the amount of potentially unphysical assumptions, more work on peak deconvolution is required, and will be explored in [4.2](#).

4.1 Compositional Grading

As has been thoroughly discussed thus far, the synthesized structures in this paper each possess an absorber dot which itself is compositionally inhomogeneous - that is, it consists of a Te-rich center and Se-rich outer 'shell' region. When this study was initially proposed however, it was expected that the absorber dot would be uniform in composition, as is the case for the kinetic rate model proposed for this system. The effect of compositional grading is not only interesting in the absorber dot, but in the CdS rod as well. Recalling the epitaxial quantum structures discussed in [2.2.3.3](#), there was a band gap 'funnel' formed by the compositional grading of the region separating both the absorbing and emitting sites, which aimed to increase the upconversion efficiency by promoting carrier migration to the emitting site. Through different synthetic techniques, formation of the same type of 'funnel' is possible in the CdS rod, and might impact upconverter performance. Therefore, between the rod and absorber dot, there are four variations of the structure available via compositional grading, which can be seen in [Figure 27](#).

It is expected that the structure with a graded absorber dot and flat rod will have the lowest UCQY of the four possibilities, due to the trap states introduced by the outer 'shell' of the absorber dot and the lower driving force for carrier migration to the emitter dot, while the structure with the flat dot and graded rod will have the highest UCQY by similar reasoning. If this is found to be the case, and in particular it

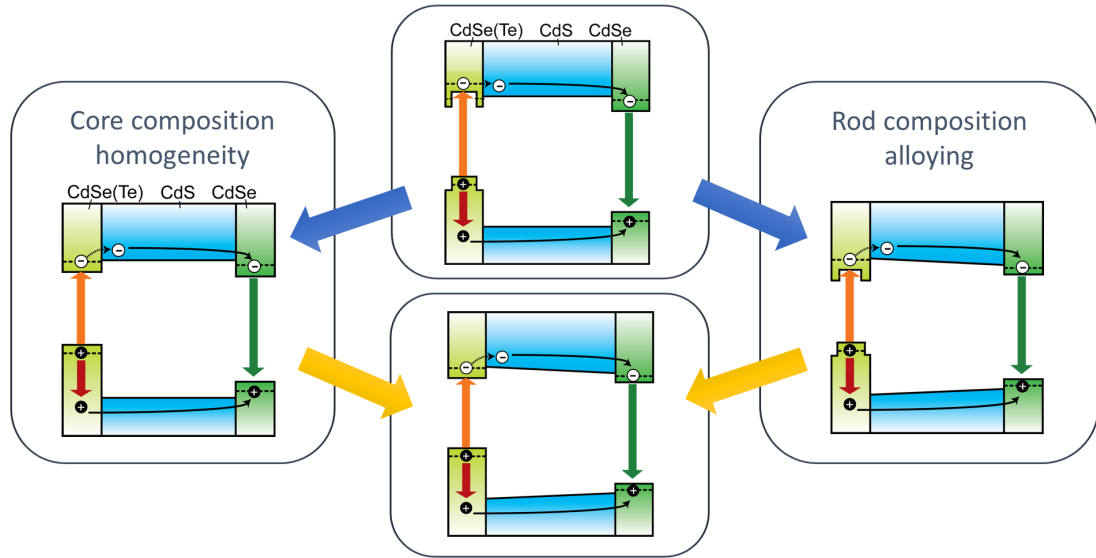


Figure 27: Four variations of the CdSe(Te)/CdS/CdSe upconverting nanostructure available by changes in the compositional grading of the absorber quantum dot and the CdS rod. The current version consists of a graded absorber, flat rod (top), and the proposed optimized version consists of a flat absorber and graded rod (bottom).

is found that a flat absorber dot improves the performance over the graded dot, then this improved structure can be studied with varying Te-doping. Because the Te-doping would then directly affect the band gap of the absorber dot, this would allow for more precise band gap engineering, with hopefully much more definitive results on the affect of the Te-content of the absorber.

4.2 Peak Deconvolution

The second major difficulty seen in this study was the difficulty in separating the behavior of the emitter quantum dot from the absorber quantum dot due to large overlap in the emitter and absorber peaks. This issue was addressed in part in 3.4, but the two-Gaussian fit used to resolve the two peaks relied on potentially incorrect assumptions, potentially unphysical fits, and introduced a new source of error that is not properly quantified. Making any physical assertions based on the quantum yield data requires a deconvolution method that holds up physical scrutiny and that has a

defined error.

Besides fitting the UCPL data from the integrating sphere directly to two Gaussian peaks, two other fitting methods are of interest for isolating the emitter peak from the absorber peak, both of which require data in addition to the UCPL spectrum. Because the deconvolution essentially requires the deconvolution of the pure absorber peak from the true UCPL spectrum, obtaining a spectrum with the absorber peak only would be very beneficial. This can be done by performing an UCPL measurement of an intermediate product of the upconverter synthesis - the CdSe(Te)/CdS structures before the CdSe emitter dot was added. Because the excitation conditions have been observed to change the shape of the absorber peak when the excitation wavelength is within the range of the peak rather than far below the peak, it is critical to take this absorber-only 'UCPL' spectrum at the same excitation conditions as the full structure UCPL spectrum.

Once the absorber-only spectrum is obtained, there are two methods for deconvolving it from the full structure UCPL spectrum. In the first method, the absorber-only UCPL is fit to a Gaussian function, then the full structure UCPL is fit to a customized function consisting of the sum of a Gaussian function and a scaling factor times the fit of the absorber-only data. The second method forgoes the fit of the absorber-only data, and instead fits the full structure UCPL to a customized function consisting of the sum of a Gaussian function and a scaling factor times the raw absorber-only data. The first method relies on the same assumptions as the fitting method previously used, namely that both peaks obey a Gaussian peak shape. As was seen in the PL and UCPL presented in this paper, this is mostly true for the emitter dot, but can be very inaccurate for the absorber dot. The new method, using the absorber-only data for a primary fit, reduces the error associated with performing a two-Gaussian fit on very noisy and highly convolved data from the integrating sphere. However, it introduces the potential for error due to variations in the absorber peak shape between the intermediate CdSe(Te)/CdS sample and the full CdSe(Te)/CdS/CdSe sample.

The latter of the newly discussed fitting methods relaxes the questionable assumption that the absorber peak is perfectly Gaussian. In doing so, it also reduced the dependence of the deconvolution on potentially unphysical fits that might arise from fitting only a small portion of the full absorber peak to a Gaussian form. However, because the absorber-only data has a fairly low signal-to-noise ratio in the region of highest overlap, and the full UCPL spectrum itself has a low signal-to-noise ratio, this may require fitting noise to noise in some regions. Additionally, this method still assumes that the absorber peak shape has not changed during the final step of synthesis. Therefore, while both of the newly discussed fitting methods improve on the original method in some respects, neither are perfect. However, if the UCQY results from each method show fair agreement, then the choice of fitting method, and therefore the choice of assumptions, has little impact on the resulting integrated counts of the emitter peak. Even if there is some spread in the results, average and range of the results from the different methods provides some quantification of the error associated with each. Therefore, in future experiments, rather than carry out just one fitting method, all three should be performed to find the average UCQY and the approximate error in the measurement. An example of these three fits performed in parallel on the same data set is shown in [Figure 28](#).

In addition to using this fitting routine to give more accurate UCQY measurements, these methods can resolve the issue with power dependence measurements, where it was difficult to isolate the dependence of the emitter peak only on the excitation power density. This method would not only allow for an isolated integrated peak counts for the emitter peak, but would give approximate error on each data point. This would lead to a more accurate log-log slope for the emitter only, as well as a better estimate of the error associated with the upconversion order. Therefore, the use of proper deconvolution methods is critical in gaining a precise understanding of the performance of future generations of upconverting structures.

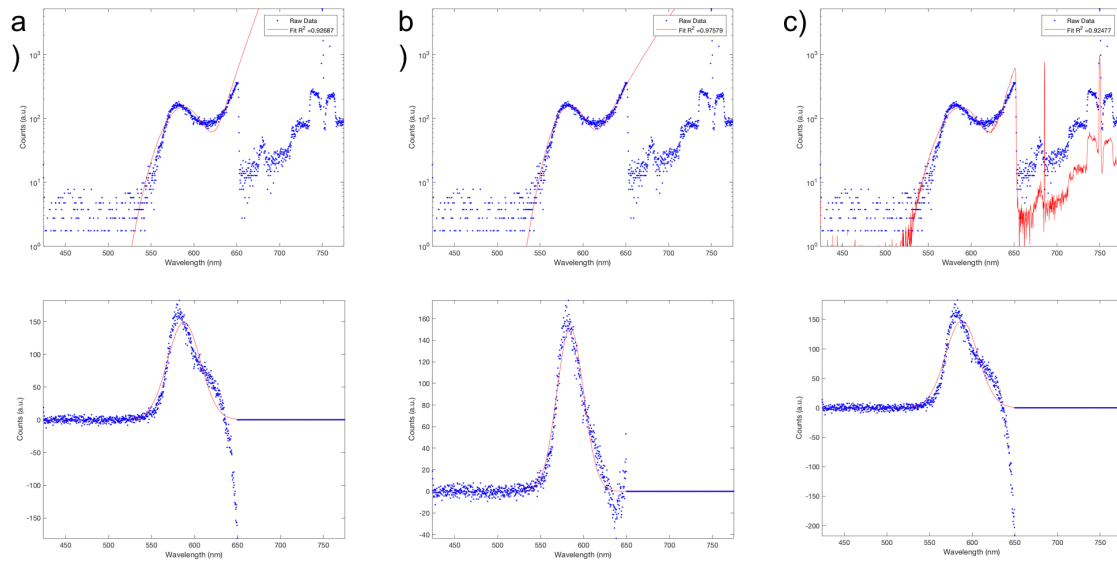


Figure 28: Three methods for deconvolving the emitter and absorber peaks. The top figures show the UCPL spectra with the complete fit, and the bottom figures show the deconvolved emitter peak with its Gaussian fit for (a) the fitting method involving a Gaussian fit plus a scaled version of the absorber-rod fit, (b) a two-Gaussian fit of the full UCPL data only, and (c) the fitting method involving a Gaussian fit plus a scaled version of the raw absorber-rod data.

BIBLIOGRAPHY

- [1] S. Fischer, E. Favilla, M. Tonelli, and J.C. Goldschmidt. Record efficient upconverter solar cell devices with optimized bifacial silicon solar cells and monocrystalline $\text{BaY}_2\text{F}_8:30\% \text{Er}^{3+}$ upconverter. *Solar Energy Materials & Solar Cells*, 2015.
- [2] X. Cao, B. Hu, and P. Zhang. High upconversion efficiency from hetero triplet-triplet annihilation in multiacceptor systems. *J. Phys. Chem. Lett.*, 2013.
- [3] D.G. Sellers, J. Zhang, E.Y. Chen, Y. Zhong, M.F. Doty, and J.M.O. Zide. Novel nanostructure for efficient photon upconversion and high-efficiency photovoltaics. *Solar Energy Materials & Solar Cells*, 2016.
- [4] R. Vadrucci, C. Weder, and Y.C. Simon. Low-power photon upconversion in organic glasses. *J. Mater. Chem. C*, 2014.
- [5] E.Y. Chen, J. Zhang, D.G. Sellers, Y. Zhong, J.M.O. Zide, and M.F. Doty. A kinetic rate model of novel upconversion nanostructures for high-efficiency photovoltaics. *IEEE Journal of Photovoltaics*, 2016.
- [6] W. Shockley and H.J. Queisser. Detailed balance limit of efficiency of p-n junction solar cells. *Journal of Applied Physics*, 1961.
- [7] S. Ruhle. Tabulated values of the Shockley-Queisser limit for single junction solar cells. *Solar Energy*, 2016.
- [8] D.N. Congreve, J. Lee, N.J Thompson, E. Hontz, S.R. Yost, P.D. Reusswig, M.E. Bahlke, S. Reineke, T.V. Voorhis, and M.A. Baldo. External quantum efficiency above 100% in a singlet-exciton-fission-based organic photovoltaic cell. *Science*, 2013.
- [9] T. Trupke, M.A. Green, and P. Würfel. Improving solar cell efficiencies by down-conversion of high-energy photons. *Journal of Applied Physics*, 2002.
- [10] E. Klampaftis, D. Ross, K.R. McIntosh, and B.S. Richards. Enhancing the performance of solar cells via luminescent down-shifting of the incident spectrum: A review. *Solar Energy Materials & Solar Cells*, 2009.
- [11] A. Luque and A. Marti. Increasing the efficiency of ideal solar cells by photon induced transitions at intermediate levels. *Physical Review Letters*, 1997.

- [12] A.S. Brown and M.A. Green. Impurity photovoltaic effect: Fundamental energy conversion efficiency limits. *Journal of Applied Physics*, 2002.
- [13] A. De Vos. Detailed balance limit of the efficiency of tandem solar cells. *J. Phys. D: Appl. Phys.*, 1980.
- [14] R. Krogstrup, H.I. Jorgensen, M. Heiss, O. Demichel, J.V. Holm, M. Aagesen, J. Nygard, and A.F. Morral. Single-nanowire solar cells beyond the Shockley-Queisser limit. *Nature Photonics*, 2013.
- [15] D.G. Sellers, S. Polly, S.M. Hubbard, and M.F. Doty. Analyzing carrier escape mechanisms in InAs/GaAs quantum dot p-i-n junction photovoltaic cells. *Appl. Phys. Lett.*, 2014.
- [16] T. Trupke, M.A. Green, and P. Würfel. Improving solar cell efficiencies by up-conversion of sub-band-gap light. *Journal of Applied Physics*, 2002.
- [17] S. Fischer, J.C. Goldschmidt, P. Loper, G.H. Bauer, R. Bruggemann, K. Kramer, D. Biner, M. Hermle, and S.W. Glunz. Enhancement of solar cell efficiency by upconversion: Optical and electrical characterization. *Journal of Applied Physics*, 2010.
- [18] A. Bril, J.L. Sommerdijk, and A.W. de Jager. On the efficiency of Yb^{3+} - Er^{3+} activated up-conversion phosphors. *J. Electrochem. Soc.*, 1975.
- [19] C. Rennero-Lecuna, R. Martin-Rodriguez, and R. Valiente. Origin of the high up-conversion green luminescence efficiency in $\beta\text{-NaYF}_4:2\%\text{Er}^{3+}, 20\%\text{Yb}^{3+}$. *Chemistry of Materials*, 2011.
- [20] R.S. Khnayzer, J. Blumhoff, J.A. Harrington, A. Haefele, F. Deng, and F.N. Castellano. Upconversion-powered photoelectrochemistry. *Chemical Communications*, 2012.
- [21] X. Wang, W.W. Yu, J. Zhang, J. Aldana, X. Peng, and M. Xiao. Photoluminescence upconversion in colloidal CdTe quantum dots. *Physical Review B*, 2003.
- [22] D.M. Tex and I. Kamiya. Upconversion of infrared photons to visible luminescence using InAs-based quantum structures. *Physical Review B*, 2011.
- [23] N.S. Makarov, Q. Lin, J.M. Pietryga, I. Robel, and V.I. Klimov. Auger up-conversion of low intensity infrared light in engineered quantum dots. *ACS Nano*, 2016.
- [24] A. Teitelboim and D. Oron. Broadband near-infrared to visible upconversion in quantum dot-quantum well heterostructures. *ACS Nano*, 2016.
- [25] Z. Deutsch, L. Neeman, and D. Oron. Luminescence upconversion in colloidal double quantum dots. *Nature Nanotechnology*, 2013.

- [26] L. Carbone et al. Synthesis and micrometer-scale assembly of colloidal CdSe/CdS nanorods prepared by a seeded growth approach. *Nano Lett.*, 2007.
- [27] E.Y. Chen, C.C. Milleville, Z. Li, K.R. Lennon, and M.F. Doty. CdSe(Te)/CdS/CdSe rods vs. CdTe/CdS/CdSe spheres: Morphology-dependent carrier dynamics for photon upconversion. 44th IEEE Photovoltaics Specialist Conference.
- [28] C. Carlone and A. Beliveau. On the anti-Stokes fluorescence in $\text{Cd}_{1-x}\text{Zn}_x\text{S}$ crystals. *Journal of Luminescence*, 1991.
- [29] Y.P. Rakovich et al. Anti-Stokes luminescence of cadmium telluride nanocrystals. *Journal of Applied Spectroscopy*, 2002.
- [30] P.P. Paskov, P.O. Holtz, B. Monemar, J.M. Garcia, W.V. Schoenfeld, and P.M. Petroff. Photoluminescence up-conversion in InAs/GaAs self-assembled quantum dots. *Applied Physics Letters*, 2000.
- [31] Time-Correlated Single Photon Counting. Wahl, m. Technical report, PicoQuant, 2014.
- [32] S. Fischer, B. Frohlich, H. Steinkemper, K.W. Kramer, and J.C. Goldschmidt. Absolute upconversion quantum yield of $\beta\text{-NaYF}_4$ doped with Er^{3+} and external quantum efficiency of upconverter solar cell devices under broad-band excitation considering spectral mismatch corrections. *Solar Energy Materials & Solar Cells*, 2014.
- [33] Labsphere, Inc. *Optical-grade Spectralon Reflectance Material*.
- [34] F. Grum and G.W. Luckey. Optical sphere paint and a working standard of reflectance. *Applied Optics*, 1968.
- [35] L. Porres, A. Holland, L.O. Palsson, A.P. Monkman, C. Kemp, and A. Beeby. Absolute measurements of photoluminescence quantum yield of solutions using an integrating sphere. *Journal of Fluorescence*, 2006.
- [36] A.M. Brouwer. Standards for photoluminescence quantum yield measurements in solution (IUPAC Technical Report). *Pure Appl. Chem.*, 2011.
- [37] C. Wurth, M.G. Gonzalez, R. Niessner, U. Panne, C. Haisch, and U.R. Genger. Determination of the absolute fluorescence quantum yield of rhodamine 6g with optical and photoacoustic methods providing the basis for fluorescence quantum yield standards. *Talanta*, 2012.

Appendix A

MATLAB PROGRAM FOR CALCULATING QY AND UCQY

To expedite the process for calculating the QY and UCQY after all the necessary data is taken, a GUI-based MATLAB program was developed which allowed users to view in real time the PL and UCPL spectra used to calculate the QY or UCQY. In addition, this program contained features to amend the UCQY calculations in the case that the UCPL spectrum contained overlap between a desired peak and an undesired peak. In this case, the program allows users to enter new data to deconvolute the peak, or deconvolve it using a two-Gaussian fitting method with no additional data. The user can vary fitting parameters and constraints, and observe immediate feedback on the fitting results with goodness-of-fit statistics, as well as observe the UCQY values calculated by various fitting methods. The program also allowed users to save the results of the fitting methods as figures and summary data files for future reference.

For the analysis conducted in the body of this paper, the only deconvolution fitting method employed was the two-Gaussian fit on the full-structure UCPL only, because data on the core-rod UCPL was unavailable. However, in subsequent work that is outside the scope of this paper, two additional fitting methods, which involve the use of core-rod UCPL data, were used to provide estimates on the uncertainty resulting from choosing a particular fitting method. The two-Gaussian fit carried out using the full-structure data only is referred to as 'Method B' in the following explanations and figures. 'Method A' refers to the method by which the core-rod UCPL is fit to a single Gaussian peak, and the full-structure UCPL is fit to a custom function consisting of a single Gaussian plus a scaling factor times the core-rod fit. 'Method C' refers to the method by which the full-structure UCPL is fit to a custom function consisting of a single Gaussian plus a scaling factor times the raw core-rod data.

The full MATLAB program employs three different GUI windows, two of which are secondary and are toggled after the use of the main GUI. The main window that is displayed when the program is opened is shown in [Figure A.1](#). The secondary window, toggled when the 'deconvolution' feature is activated on the main GUI, is shown in [Figure A.2](#). The results window, which is toggled to display the results of the fitting methods, is shown in [Figure A.3](#).

A.1 Main Window

The main window contains fields in which all of the information necessary to complete the calculation of QY or UCQY can be entered by the user. It displays in real time the reference and sample spectra that are selected by the user as '.txt' files from their computer. The main window is shown in [Figure A.1](#), and each important element is labeled with a number. Any elements not labeled are not used for the calculations discussed in this paper, some of which are vestiges of previous computation methods.

1. **Reference Browse Files Button:** this button opens up a file browser that allows the user to choose the '.txt' file that corresponds to the rhodamine 101 reference spectrum, then a browser which that the user to choose the corresponding dark counts spectrum
2. **Reference Axes:** the rhodamine 101 reference spectrum selected by the user will be displayed here
3. **Reference Left Integration Limit:** this slider allows the user to choose the lower limit of integration on the reference spectrum
4. **Reference Right Integration Limit:** this slider allows the user to choose the upper limit of integration on the reference spectrum
5. **Reference Laser Power:** the user can enter the measured laser power used to obtain the reference spectrum (in mW)
6. **Reference Laser Wavelength:** the user can enter the laser wavelength used to obtain the reference spectrum (412nm by default)
7. **Reference Quantum Yield:** the user can enter the known quantum yield for the reference (1.00 by default)
8. **Reference Integration Time:** the user can enter the integration time used for the reference spectrum (0.25s by default)

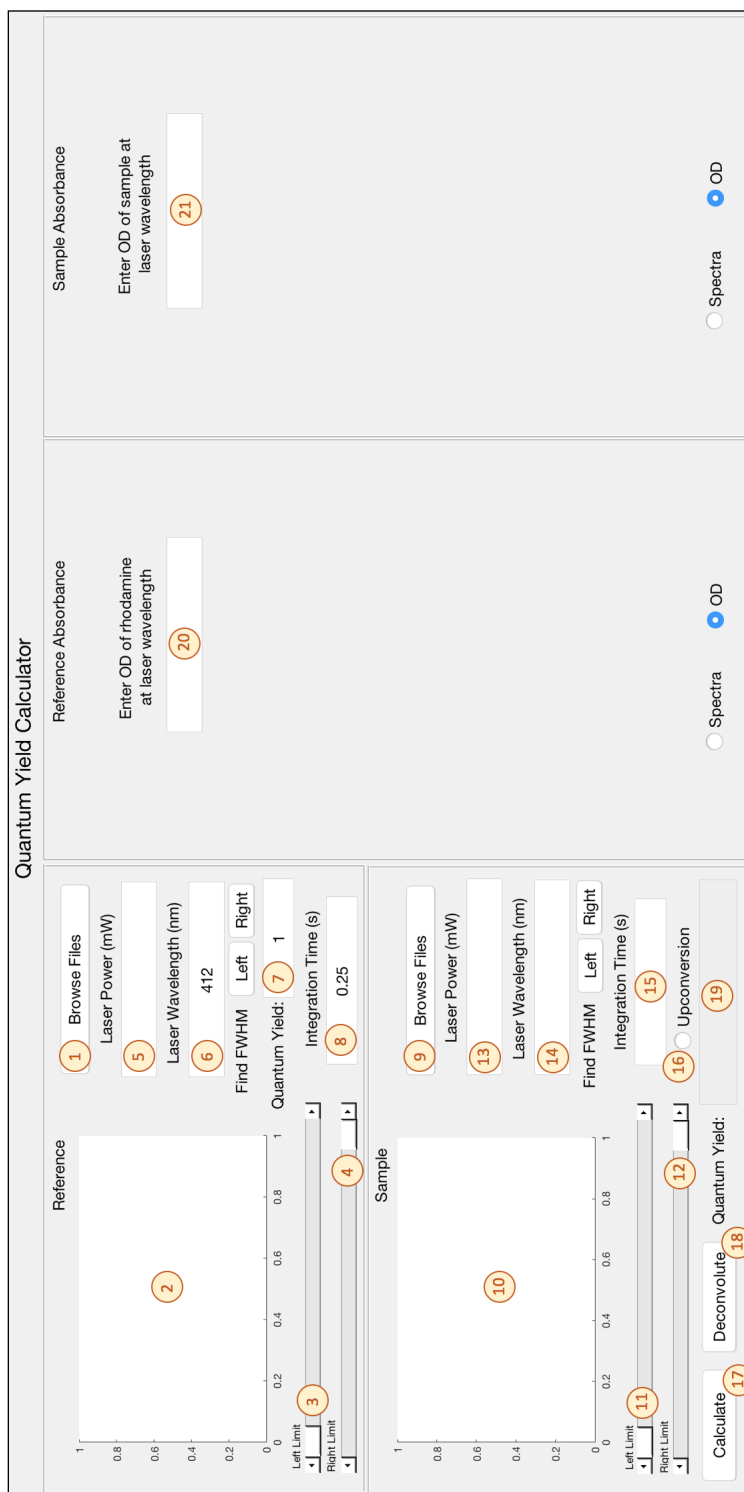


Figure A.1: The main window of the Quantum Yield MATLAB program.

9. **Sample Browse Files Button:** this button opens up a file browser that allows the user to choose the '.txt' file that corresponds to the sample spectrum, then a browser which that the user to choose the corresponding dark counts spectrum
10. **Sample Axes:** the sample spectrum selected by the user will be displayed here
11. **Sample Left Integration Limit:** this slider allows the user to choose the lower limit of integration on the sample spectrum
12. **Sample Right Integration Limit:** this slider allows the user to choose the upper limit of integration on the sample spectrum
13. **Sample Laser Power:** the user can enter the measured laser power used to obtain the sample spectrum (in mW)
14. **Sample Laser Wavelength:** the user can enter the laser wavelength used to obtain the sample spectrum
15. **Sample Integration Time:** the user can enter the integration time used for the sample spectrum
16. **Upconversion Switch:** for upconversion measurements, the user can toggle this feature to multiply the QY calculation by 2 to obtain the UCQY
17. **Calculate Button:** if no deconvolution of the PL/UCPL spectrum is necessary, the user can click this button to calculate the QY/UCQY, which is displayed in the 'Sample Quantum Yield' field
18. **Deconvolute Button:** if deconvolution of the UCPL spectrum is necessary, the user can click this button to toggle the secondary window which allows for calculation of UCQY by peak deconvolution fits
19. **Sample Quantum Yield:** if the 'Calculate Button' is clicked, the resulting QY/UCQY calculated from the spectra and data is displayed here (on a scale of 0 to 1)
20. **Reference Absorbance:** here, the user will input the reference absorbance as an optical density (OD) value
21. **Sample Absorbance:** here, the user will input the sample absorbance as an OD value

A.2 Secondary Window

This window is toggled when the 'Deconvolute Button' on the main window is clicked. It imports all of the data inputted by the user in the main window for refined

UCQY calculations using deconvolution fits. The first secondary window is shown in [Figure A.2](#), and each important element is labeled with a number. Any elements not labeled are not used for the calculations discussed in this paper, some of which are vestiges of previous computation methods.

1. **Browse Files Button:** this button opens up a file browser that allows the user to select the '.txt' file corresponding to the core-rod UCPL spectrum, and the file for the corresponding dark counts spectrum
2. **Deconvolute Button:** this button, when clicked, opens the results window to display the results of all deconvolution methods. If no core-rod spectrum is entered, this button still functions, and will execute only the 'Method B' deconvolution
3. **Short Pass:** the user can enter here the 'short pass' value. This value defines the upper limit of the core-rod Gaussian fit, as well as all of the deconvolution fitting methods on the full-structure spectrum (set at 650nm by default)
4. **Plot Type Menu:** this menu allows the user to switch between a logarithmic and linear y-scale on the 'Core-Rod Axes'
5. **Core-Rod Axes:** the core-rod spectrum and corresponding fit will be displayed on these axes, with the desired y-scale

A.3 Results Window

This window is toggles when the 'Deconvolute Button' is clicked on the secondary window. It imports all data from the main window and the secondary window, and displays the results for all fitting methods. It also allows parameters of the fit, such as the bounds and initial guesses for fitting parameters, to be adjusted by the user using the various 'Options' buttons. As mentioned, 'Method A' refers to the method involving a Gaussian fit of the core-rod data, and a Gaussian plus scaling factor fit of the full-structure data. 'Method B' refers to the purely two-Gaussian fit of the full-structure data only. 'Method C' refers to the method involving a Gaussian plus scaling factor fit of the full-structure data using the raw core-rod data only. The results window is shown in [Figure A.3](#).

1. **Method A Options:** this button displays the fit options (i.e. parameter bounds and initialization) for Method A, which can be adjusted by the user

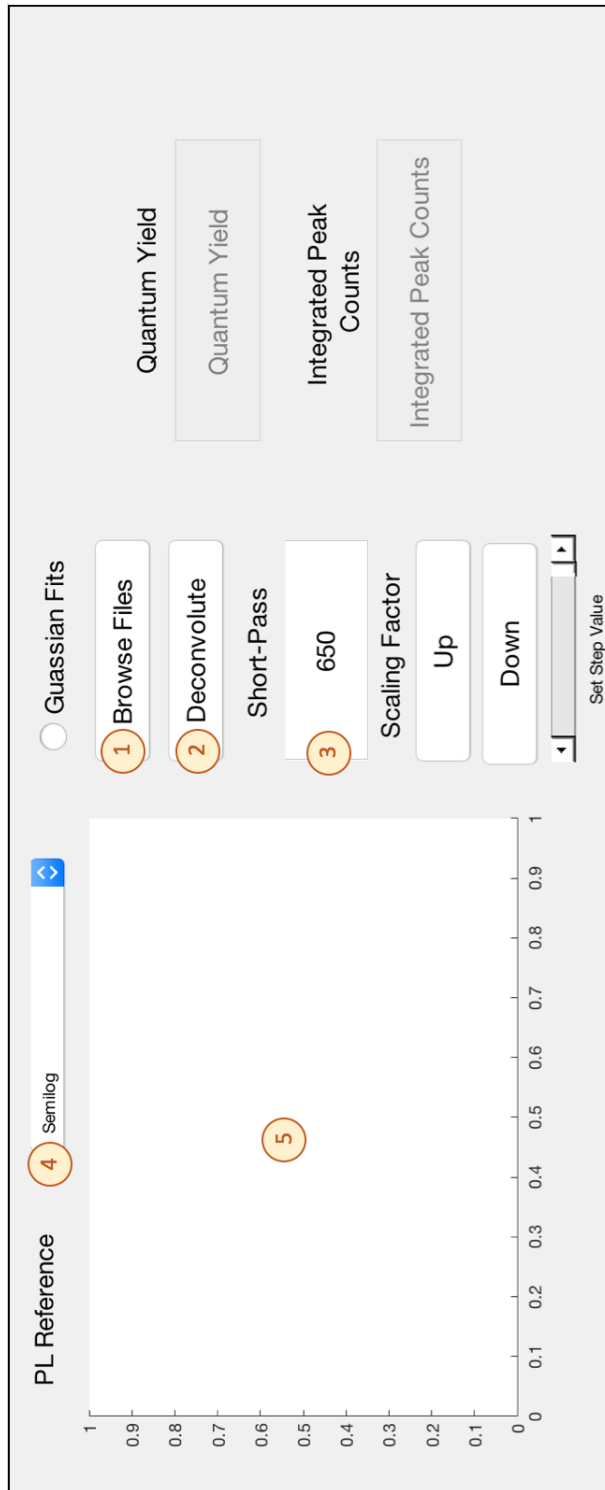


Figure A.2: The first secondary window of the Quantum Yield MATLAB program.

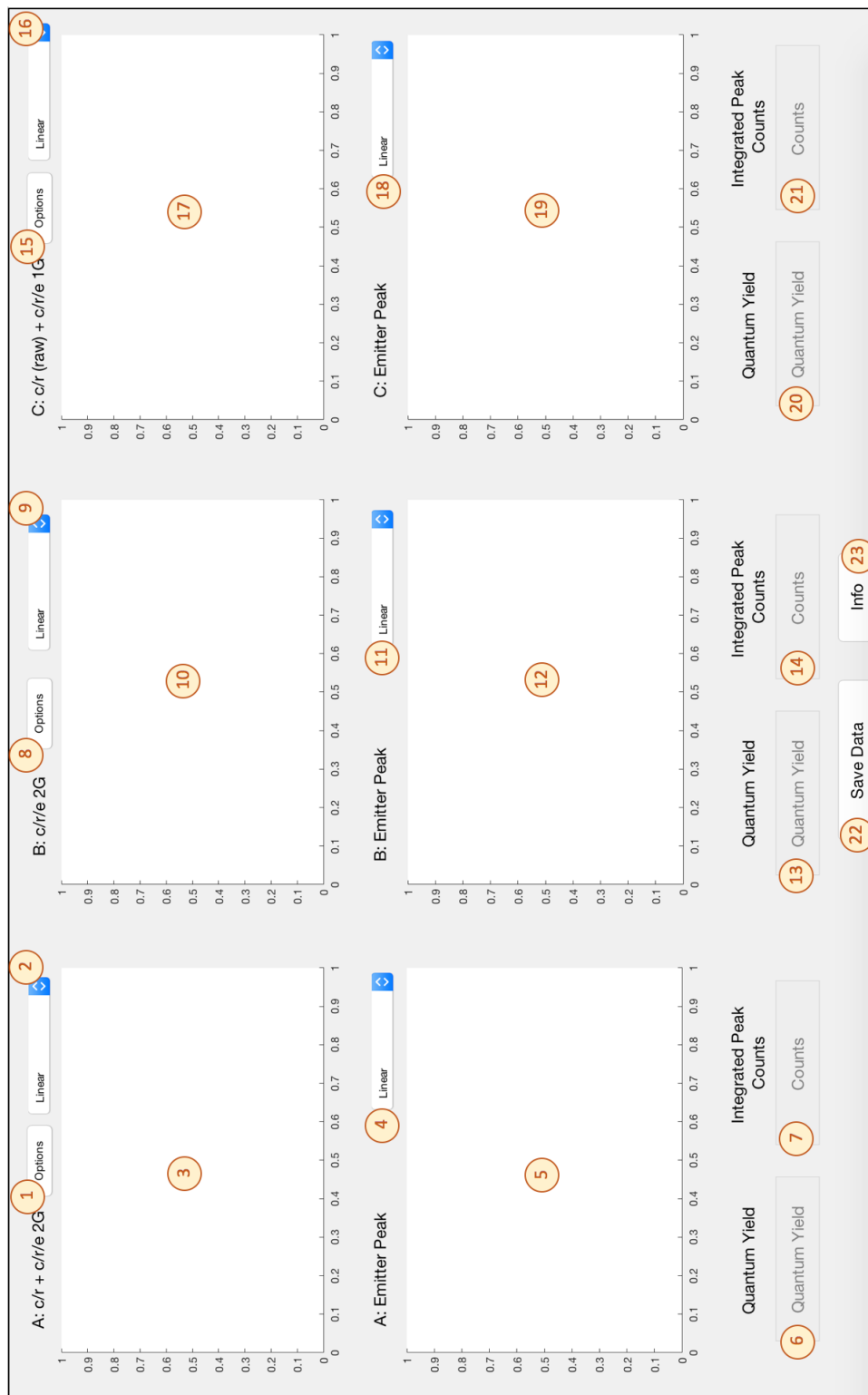


Figure A.3: The results window of the Quantum Yield MATLAB program.

2. **Method A Full-Structure Plot Type:** this menu allows the user to change the y-axis of the 'Method A Full-Structure Axes' between logarithmic and linear
3. **Method A Full-Structure Axes:** the full-structure spectrum overlaid with the Method A fit will be displayed on these axes
4. **Method A Emitter Spectrum Plot Type:** this menu allows the user to change the y-axis of the 'Method A Emitter Spectrum Axes' between logarithmic and linear
5. **Method A Emitter Spectrum Axes:** the deconvolved emitter spectrum data using Method A, and the corresponding emitter Gaussian function, will be shown on these axes
6. **Method A Quantum Yield:** the UCQY for the emitter peak obtained using Method A will be displayed here
7. **Method A Peak Counts:** the raw integrated peak counts for the emitter peak using Method A will be displayed here
8. **Method B Options:** this button displays the fit options (i.e. parameter bounds and initialization) for Method B, which can be adjusted by the user
9. **Method B Full-Structure Plot Type:** this menu allows the user to change the y-axis of the 'Method B Full-Structure Axes' between logarithmic and linear
10. **Method B Full-Structure Axes:** the full-structure spectrum overlaid with the Method B fit will be displayed on these axes
11. **Method B Emitter Spectrum Plot Type:** this menu allows the user to change the y-axis of the 'Method B Emitter Spectrum Axes' between logarithmic and linear
12. **Method B Emitter Spectrum Axes:** the deconvolved emitter spectrum data using Method B, and the corresponding emitter Gaussian function, will be shown on these axes
13. **Method B Quantum Yield:** the UCQY for the emitter peak obtained using Method B will be displayed here
14. **Method B Peak Counts:** the raw integrated peak counts for the emitter peak using Method B will be displayed here
15. **Method C Options:** this button displays the fit options (i.e. parameter bounds and initialization) for Method C, which can be adjusted by the user
16. **Method C Full-Structure Plot Type:** this menu allows the user to change the y-axis of the 'Method C Full-Structure Axes' between logarithmic and linear

17. **Method C Full-Structure Axes:** the full-structure spectrum overlaid with the Method C fit will be displayed on these axes
18. **Method C Emitter Spectrum Plot Type:** this menu allows the user to change the y-axis of the 'Method C Emitter Spectrum Axes' between logarithmic and linear
19. **Method C Emitter Spectrum Axes:** the deconvolved emitter spectrum data using Method C, and the corresponding emitter Gaussian function, will be shown on these axes
20. **Method C Quantum Yield:** the UCQY for the emitter peak obtained using Method C will be displayed here
21. **Method C Peak Counts:** the raw integrated peak counts for the emitter peak using Method C will be displayed here
22. **Save Data Button:** when clicked, this button will prompt the user to enter a folder name and location in which the data will be saved. The saved folder will include all figures in this results window, as well as a summary of all fitting parameters, UCQY values, and peak count values
23. **Info Button:** when clicked, this button will open a PDF file containing information about this results window